

NORTHWESTERN UNIVERSITY

Thermal and Electrical Transport in Thin-Film Materials for Energy
Management

A DISSERTATION

SUBMITTED

IN PARTIAL FULFILLMENT OF THE REQUIREMENTS

for the degree

DOCTOR OF PHILOSOPHY

Field of Applied Physics

By

Boya Cui

EVANSTON, ILLINOIS

September 2017

© Copyright by Boya Cui 2017

All Rights Reserved

ABSTRACT

Thermal and Electrical Transport in Thin-Film Materials for Energy Management

Boya Cui

With the rapidly growing global demand in energy nowadays, innovation and technology become critical for a transition to renewable energy, high energy efficiency or low-carbon emission. Thin-film materials are especially favorable in energy management due to the easy integration into devices. The transport properties for heat and electrical conduction are critical not only to achieve a better fundamental understanding of underlying physics, but also to develop proper and efficient operation of devices. In order to apply the Materials Genome paradigm to calculate the properties of possible new energy materials, the performance of existing materials must be properly characterized, first. This thesis studies three materials corresponding to three aspects of energy management: storage, efficiency, and conversion.

For energy storage, metal organic frameworks (MOF) are a category of highly porous materials with large surface area for natural gas adsorption and storage. Thermal conductivity is a crucial parameter for managing the exothermal process of gas adsorption as well as the endothermal process of gas desorption in MOFs, but experimental studies up

to now have been limited. As a case study of MOFs, the cross-plane thermal conductivity of a zeolitic imidazolate framework (ZIF)-8 was experimentally determined on thin films using the 3ω technique at different partial pressures in perfluorohexane, nitrogen, air, or vacuum ambients at room temperature. The observed thermal conductivity was observed to be approximately independent of ambient gas species and pressure ranging from atmospheric pressure down to vacuum. This approach of probing MOF thermal conductivity with gas adsorption establishes a method for studying MOFs with different gas ambients for effective thermal management for adsorbed natural gas applications.

In terms of energy efficiency, transparent conducting oxide InGaZnO (IGZO) is a commercialized high-performance active channel material in transparent thin-film transistors. IGZO consumes less power due to its high carrier mobility, low leakage current and good transparency. For effective thermal management of IGZO-based devices, a comprehensive study measured the thermal conductivity of various different phases of amorphous (a-IGZO), semicrystalline (semi-c-IGZO), and c-axis-aligned single-crystal-like IGZO (c-IGZO) grown by various physical deposition and chemical synthesis approaches. The atomic structures of the amorphous and crystalline films were simulated with ab initio molecular dynamics, and the film morphology was assessed by multiple X-ray techniques. The temperature-dependent thermal conductivity showed pronounced dependence on porosity, crystallinity, and shelf time. All samples are consistent with the porosity-adapted CahillPohl (p-CP) model of minimum thermal conductivity.

Lastly for energy conversion, $p \times n$ -type transverse thermoelectric (TTE) is a new paradigm where the material shows n -type and p -type behavior in two orthogonal crystal axes, respectively, leading to effective heat flow perpendicular to the current flow. Both

thin-film and bulk materials will be relevant for energy harvesting and energy management applications. To facilitate the rapid discovery of new $p \times n$ -type TTE by employing Material Genome, we introduce the criteria to identify bulk $p \times n$ TTE's from the calculated three-dimensional Seebeck tensor. A thorough search is conducted in the past literature for ambipolar compounds as $p \times n$ -type transverse thermoelectric candidates, for which the figure of merit and critical angles are calculated to evaluate their potential performance. To better understand the underlying mechanism of anisotropy, band structure and thermopower calculation are also conducted on two representative compounds.

Besides the bulk ambipolar compounds, the type-II superlattice of InAs/GaSb is another $p \times n$ -type TTE which can be prepared in thin-film form. For these novel materials, the emphasis is currently on testing and developing the appropriate characterization methods of their thermal and electrical conduction so that these advanced materials can be researched and improved. Both the in-plane and cross-plane thermal conductivities are characterized by 2-wire 3ω method. A measurement example of T2SL is also shown from room temperature down to 15 K. To deconvolve the electrical characteristics of each carrier species in this multi-carrier system, Fourier-domain mobility spectrum analysis (FMSA) is developed in Matlab with an intuitively simple algorithm, fast convergence, low computational cost, simplicity of implementation, and good fitting accuracy. The temperature-dependent measurement examples of T2SL are shown for both thermal conductivity and FMSA.

Acknowledgements

I would like to express my gratitude to my advisor Prof. Grayson for his support and guidance throughout my PhD study. He not only gives tremendous help tackle existing problems, but also keeps stimulating new thoughts for one step further. He sets an example of a passionate scientist and a dedicated educator, whose persistent and rigorous spirits will benefit me for my life and future career.

In the interdisciplinary projects, I am grateful for working with collaborators from different groups and institutions who provided insightful input from the perspective of their fields and teach me something different in every discussion. Special thanks go to the Chang Group, the Marks Group, and the Hupp Group at Northwestern, as well as Prof. Medvedeva at Missouri University of Science and Technology and Prof. Jiong Yang at Shanghai University.

Many thanks to my groupmates for their help, especially Chuanle Zhou and Yang Tang who mentored me from my 1st year. I am also lucky to meet all my friends at Northwestern who are always by my side supporting and accompanying me here.

Finally, I could not thank my parents and family enough for their unconditional love. Thanks to them for giving me courage when I am down, for always caring about me from the other side of the globe, and for supporting me to pursuing my dream no matter what. Thanks to my boyfriend for sharing happiness and sorrow with me along the way. I am so blessed.

Table of Contents

ABSTRACT	3
Acknowledgements	6
List of Tables	9
List of Figures	10
Chapter 1. Introduction: Thin-Film Materials for Energy Management	14
1.1. Metal Organic Framework ZIF-8 for Fuel Gas Storage	14
1.2. Indium Gallium Zinc Oxide for High Energy-Efficiency Thin-film Transistors	16
1.3. $p \times n$ -Type Transverse Thermoelectrics for Energy Conversion	18
Chapter 2. Metal Organic Framework ZIF-8 Thermal Conductivity under Gas Adsorption	21
2.1. Prior Research	21
2.2. Film Growth and Morphology	22
2.3. Thermal Characterization: 3ω Method	24
2.4. Gas Adsorption in ZIF-8	28
2.5. Thermal Conductivity Under Ambient Gas Pressure	30
2.6. Future Work	34

Chapter 3. Indium Gallium Zinc Oxide Thermal Conductivity and Morphology	
Comparison	36
3.1. Prior Research	36
3.2. Film Preparation	38
3.3. Simulation and Modeling	41
3.4. Results of Morphology and Thermal Conductivity	44
3.5. Discussion	49
3.6. Future Work	61
Chapter 4. Candidate $p \times n$ -Type Transverse Thermoelectrics	64
4.1. Criteria for identifying $p \times n$ -Type Candidates from Calculated Seebeck Tensors	64
4.2. Candidate Materials in Ambipolar Bulk Compounds	69
4.3. Band Structure Calculation	78
4.4. Future Work	86
Chapter 5. Towards Thermal and Electrical Characterization of Thin-Film $p \times n$ -type Transverse Thermoelectrics	87
5.1. Thermal Characterization: 2-wire 3ω Method	88
5.2. Electrical Characterization: Fourier-domain Mobility Spectrum Analysis	92
5.3. Future Work	117
References	118
Appendix .	141
1. Wheatstone Configuration for 3ω Measurement	141

List of Tables

3.1	X-ray reflectivity results on the density and porosity of films fabricated by physical deposition and chemical synthesis.	47
-----	---	----

List of Figures

1.1	ZIF-8 atomic structure	15
1.2	An example structure of a-IGZO based TFT (left), and a picture of TFT sheet with good transparency and flexibility (right).	17
1.3	Microscopic electron-hole picture of a $p \times n$ -type transverse thermoelectric material	19
2.1	Morphology of ZIF-8 film: SEM and XRD results	23
2.2	Pictures of processed sample, measurement device and setup.	27
2.3	Isotherm results of ZIF-8 in N_2 environment and C_6F_{14} environment	29
2.4	Time-dependent adsorption measurement of C_6F_{14} in ZIF-8.	30
2.5	The 3ω data of ZIF-8 thin film in air at room temperature.	31
2.6	ZIF-8 thermal conductivity as a function of pressure or adsorption, with comparison with simulation studies.	32
3.1	The atomic structure of a-, semi-c-, and c-IGZO.	42
3.2	X-ray characterization results (XRD and two-dimensional GIWAXS) of a-, semi-c-, and c-IGZO thin films.	45
3.3	3ω raw data of the sputtered a-IGZO film at $T = 300$ K and 94 K, with the measurement device picture as inset.	49

3.4	Temperature dependence of the thermal conductivity of all IGZO films under study.	50
3.5	The effect of crystallinity and porosity on IGZO thin-film thermal conductivity.	51
3.6	Room-temperature thermal conductivity as a function of over one and a half years of storage time.	58
3.7	XRD pattern of semi-c IGZO film shows slightly peak shifts after 19-month storage.	59
3.8	Hall mobility of transparent conducting oxides InO and ZITO, both of which demonstrate a maximum mobility at the transition from amorphous to crystalline phase.	62
3.9	Latest results on high-porosity IGZO thin films (red) grown by one-cycle spin-combustion process, compared with original results.	62
4.1	Crystal structure of (a) CsBi_4Te_6 , (b) $\text{ReSi}_{1.75}$, (c) PdCoO_2 and (d) $\text{LiMo}_6\text{O}_{17}$.	70
4.2	Thermoelectric characteristics of CsBi_4Te_6 , $\text{ReSi}_{1.75}$, PdCoO_2 , Na_xCoO_2 and $\text{Li}_{0.9}\text{Mo}_6\text{O}_{17}$	71
4.3	Transverse figure of merit $z_{\perp}T$, critical angles θ_{zT} and θ_{JQ} , and θ_{\perp} for candidate compounds.	75
4.4	The band diagram of $\text{ReSi}_{1.75}$ without and with spin-orbit coupling in (a) and (b), respectively.	79

4.5	Calculation results of $\text{ReSi}_{1.75}$ band structure, Brillouin zone, and Fermi surfaces.	81
4.6	Rotation angle for Seebeck tensor diagonalization and the final diagonalized Seebeck coefficients	82
4.7	Calculation results of PdCoO_2 band structure, Seebeck tensor, and Fermi surfaces.	85
5.1	Schematic diagram and mask design for 2-wire 3ω method.	89
5.2	Temperature-dependent in-plane and cross-plane thermal conductivity of InAs/AlSb T2SL.	91
5.3	Flow chart of full FMSA, mobility-domain and Fourier-domain up/down.	96
5.4	The conductivity and spectral fit of mobility-domain up/down alone, where the synthetic system has two species (one electron and one hole).	100
5.5	The spectral transition corresponding to the same synthetic dataset as Figure 5.4 examined throughout the full FMSA process.	101
5.6	Convergence comparison of the squared-error χ^2 for the full FMSA and only the mobility-domain up/down technique.	102
5.7	Application of FMSA on a system with one narrow and one wide carrier distribution (one electron and one hole species).	103
5.8	Application of FMSA on a system with four carrier species (two electron and two hole species).	103

5.9	Longitudinal and transverse conductivity curves for different mobilities $\mu_{th}/10$, μ_{th} , and $10\mu_{th}$ before and after background subtraction.	105
5.10	Comparison of FMSA total error χ^2 with and without BGS as a function of central peak mobility.	108
5.11	Comparison of FMSA fitting spectra without and with BGS when the central mobility of a single electron peak moves below μ_{th} .	109
5.12	The fit of resistivity ρ_{xx} and ρ_{xy} shows a larger deviation for FMSA without BGS than that with BGS, even though the two fit spectra look equally accurate.	110
5.13	Comparison of FMSA fitting spectra for an extremely low central carrier mobility.	111
5.14	Comparison of FMSA fitting spectra without and with BGS when an high-mobility electron species coexist with a hole species below μ_{th} .	113
5.15	InAs/GaSb T2SL structure in (a) and TEM image in (b). The magnetotransport transport data at $T= 300$ K is shown in solid black lines in resistance (c) and conductivity (d), where the dashed grey lines are the FMSA fits.	115
5.16	Mobility spectral results at $T = 303$ K, 201 K, and 105 K, where the red curve corresponds to electrons and green curve corresponds to holes.	116
.1	Circuit connection of 4-point (left) and 2-point (left) measurement.	141
.2	Comparison of 3ω raw datasets from a 150-nm thick SiN_x thin film on a silica substrate.	142

CHAPTER 1

Introduction: Thin-Film Materials for Energy Management

Increasing energy demands require fast development of technology in sustainable energy. According to U.S. Energy Information Administration, total world energy consumption projects a 48% increase from 2012 to 2040.[1] With this energy crisis, access to modern low-carbon energy services, energy efficiency, and renewable energy are considered the three pillars of the required energy transition.[2] Novel materials have been found to harvest the waste energy with thermoelectrics, utilize it effectively with high energy-efficiency materials, and store renewable or low-carbon energy with highly porous materials.

In these novel materials for energy management, heat and charge transport studies are essential not only to achieve a better fundamental understanding of material properties, but also to develop proper and efficient operation of thermal management devices to meet future energy demands. This thesis illustrates thermal and electrical transport studies on the following three material systems in different aspect of energy management: energy storage, efficiency, and conversion.

1.1. Metal Organic Framework ZIF-8 for Fuel Gas Storage

Given the growing demand for greener sources energy as well as the concurrent abundance of natural gas, vehicles fueled by natural gas (NG) in place of petroleum products are an attractive intermediate step toward the realization of a ground transportation

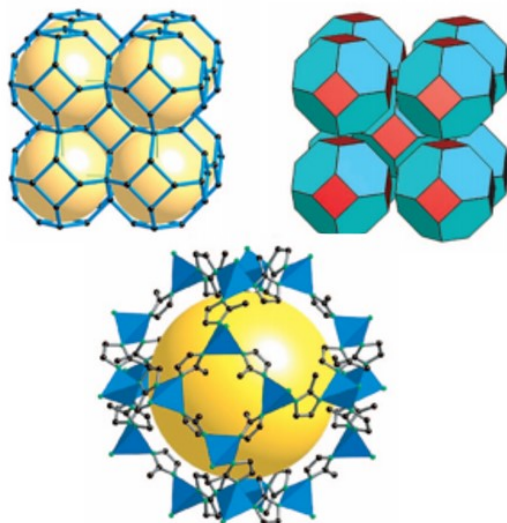


Figure 1.1. The single crystal structure [3] of ZIF-8 in stick diagram (top left) and tiling diagram (top right). Bottom diagram shows the largest cage in yellow in ZIF-8 with ZnN_4 tetrahedra in blue and H atoms omitted for clarity.

fleet that is powered by renewable sources. Vehicles of this kind, however, require large, heavy, and expensive high-pressure fuel tanks in addition to a refill-station infrastructure equipped with high-pressure equipment. To overcome these challenges, the use of fuel tanks loaded with adsorbed natural gas (ANG), as opposed to liquefied or compressed natural gas, has been proposed, as a strategy for storing large amounts of natural gas in smaller tanks at lower pressure and ambient temperature.[4] However, during the exothermic process of NG adsorption, fuel tanks and their contents undergo a significant temperature rise; depending on the rate of filling and the details tank design, as well as sorbent packing and composition temperatures can rise to over 60° [5], a change that could significantly lower a sorbents gas storage capacity.[6] Similar challenges arise with

cryosorption-based storage of molecular hydrogen, the energy source for fuel-cell powered vehicles. Thermal management in these adsorbents is critical for rapid and efficient storage and release of NG or H₂. [7]

Metalorganic frameworks (MOFs), a class of highly tailorable crystalline materials comprised of metal nodes and organic linkers. [8, 9] The high porosity and large surface area of MOF make it a promising candidate for gas adsorbents. There have been commercialized MOF-based products for gas adsorption applications in recent years. [10] Thin-film coating of MOFs provides the maximum surface area for rapid adsorption and desorption for each energy-storage cycle. It also allows for rapid heat transfer to and from the film to an underlying heat-sink for each energy-storage cycle. Among various MOFs, zeolitic imidazolate frameworks (ZIF)-8 (Figure 1.1) stands out due to its good thermal stability, chemical tailorbility and permanently large porosity [3]. ZIF-8 is an effective storage medium for fuel gases such as H₂ [11], CH₄, alkanes [12]. It is critical to study the thermal property of ZIF-8 or other MOFs during the exothermic gas adsorption for efficient operation of fuel storage device. Chapter 2 shows our most recent research on ZIF-8 thin-film thermal conductivity as a case study of MOFs with gas molecule adsorbed, which to our knowledge is the first experimental measure of MOF thermal conductivity in-situ measurement under gas adsorption.

1.2. Indium Gallium Zinc Oxide for High Energy-Efficiency Thin-film Transistors

Indium gallium zinc oxide (IGZO) thin film is a transparent conducting oxide with high carrier mobility, low intrinsic carrier concentration, good optical transparency, and consistent uniformity over large areas.[13, 14, 15, 16, 17] Both the crystalline and amorphous IGZO have been proposed to be superior electronic materials: Single-crystalline IGZO was first proposed to possess electron mobilities as high as $\mu \approx 80 \text{ cm}^2/(\text{V}\cdot\text{s})$ [13]; Amorphous phase a-IGZO became well-known later for electron mobilities $\mu > 10 \text{ cm}^2/(\text{V}\cdot\text{s})$ far exceeding that of amorphous silicon[14] (a-Si:H) as well as the ability to process at room-temperature[18], making a-IGZO a promising candidate for flexible electronics.

Among all the device applications[19, 20], IGZO is especially favorable as an active channel material in transparent thin-film transistors (TFTs), as shown in Figure 1.2. IGZO-based TFTs are more energy efficient compared with a-Si because of the superior carrier density and low leakage current[21, 22]. The good transparency of IGZO also reduced the power consumption in backlighting illumination[23].

A study of IGZO thermal conductivity is useful for effective thermal management in IGZO-based devices. Knowledge of the thermal conductivity helps to model heat generation within that active layer and the thermal distribution throughout the device[24]. Additionally, IGZO has been proposed as a thermoelectric candidate, in a similar fashion to other transparent oxides such as[25] InZnO. IGZO may have a competitive thermoelectric figure of merit [26] compared with other oxide materials, suggesting the intriguing possibility of “invisible thermoelectric device” made with transparent oxides [27, 28]. Furthermore, the large-area capabilities might allow for integration into solar panels for

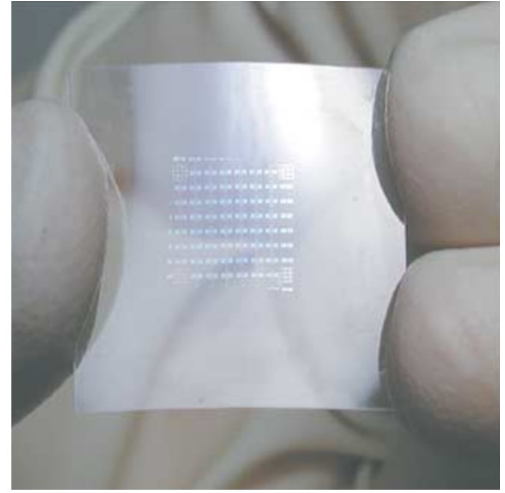
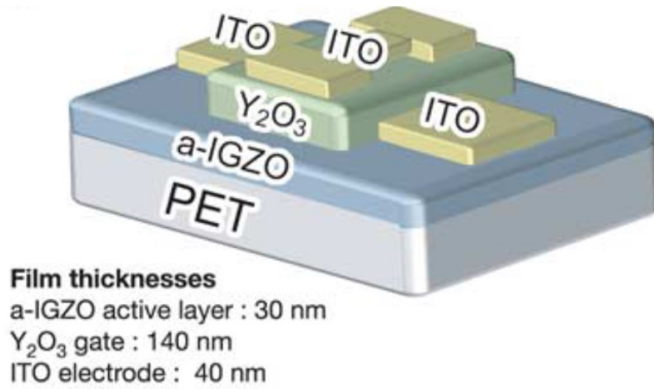


Figure 1.2. An example structure of a-IGZO based TFT (left), and a picture of TFT sheet with good transparency and flexibility (right).[15]

photovoltaic/thermal hybrid systems[29] to generate power from unavoidable waste heat. Moreover, an understanding of thermal transport in a-IGZO may yield clues to differentiate various fabrication methods, linking the thermal properties to the film structure and fabrication technique and eventually identifying strategies for improving electron mobility. Chapter 3 discussed about a comprehensive study on the transparent conducting oxide IGZO, where the thin-film morphology and temperature-dependent thermal conductivity are measured and discussed for films fabricated by diverse growth methods.

1.3. $p \times n$ -Type Transverse Thermoelectrics for Energy Conversion

Thermoelectrics, which convert thermal energy into electrical energy and vice versa, can harvest waste heat and convert it to useful work. Specifically the Seebeck effect, in which a temperature difference can create a voltage difference, form the basis of power generators for energy harvesting. Efficient collection of waste heat is essential to reduce

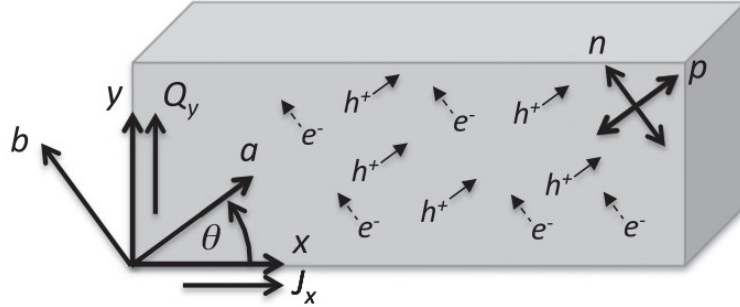


Figure 1.3. Microscopic electron-hole picture of a $p \times n$ -type transverse thermoelectric material[30], where a net p -Seebeck coefficient along a axis and a net n -Seebeck along b axis. A net charge current J_x to the right yields a net particle or heat current Q_y up.

greenhouse gas emissions and promote energy sustainability. Among thermoelectric materials, thin-film candidates not only provide flexibility and easy integration to micro-scale as the ongoing miniaturization of electronics, but also show superior thermoelectric properties due to the thickness confinement.

A “ $p \times n$ -type” transverse thermoelectric ($p \times n$ TTE) [30, 31, 32, 33, 34, 35, 36] was proposed to induce heat flow perpendicular to the current direction, where materials show n -type and p -type behavior in two orthogonal directions (Figure1.3). Unlike conventional thermoelectrics where the current and heat flow are parallel or anti-parallel with each other, TTE separates the two directions, enabling geometric engineering as another degree of freedom for enhancing figure of merit. Its intrinsic ambipolar conduction may enable cooling at cryogenic temperatures, whereas the extrinsically doped conventional thermoelectrics fail due to carrier-freezeout. A $p \times n$ TTE requires no external magnetic field to cause transverse heat flow, as do thermomagnetic materials using Nernst-Ettingshausen effect[37]. Its thin-film form can be integrated into micro-scale single-leg devices bringing simplicity of device implementation compared with double-leg longitudinal devices.

Chapter 4 introduced the criteria for identifying a $p \times n$ TTE, followed by identifying and evaluating promising ambipolar compound candidates.

Characterizing the thermal and electrical conductivity of $p \times n$ -type TTE is critical to evaluate and further enhance their figure of merit. It requires the thermal conductivity study in both cross-plane and in-plane directions, which sometimes becomes more difficult for thin film candidates. Also, the conductivity results need deconvolution since electrons and holes contribute to the conduction simultaneously. Chapter 5 showed the 2-wire 3ω method and Fourier-domain mobility spectrum analysis for thermal and electrical characterization of a thin-film $p \times n$ TTE candidate type-II superlattice (T2SL), respectively.

CHAPTER 2

Metal Organic Framework ZIF-8 Thermal Conductivity under Gas Adsorption

This chapter examines the thermal conductivity of ZIF-8 thin films with gas adsorption. Previous studies on MOF thermal conductivity are first reviewed in Section 2.1. Then Section 2.2 describes the film growth and morphology study. The 3ω method is introduced in Section 2.3 for ZIF-8 thin film thermal conductivity measurement. Section 2.4 shows the gas adsorption study of ZIF-8 in nitrogen N_2 and perfluorohexane C_6F_{14} . Thermal conductivity results measured in these two gas environments are compared and discussed in Section 2.5.

2.1. Prior Research

To date there have been few studies on the thermal conductivity of MOFs. The thermal conductivity for the prototypical MOF-5 has been obtained from simulations,[38] and confirmed experimentally only on large MOF-5 single cubic crystals.[39] Making large single crystals of MOFs can be synthetically challenging, and pelletization of MOF powders for measurements can be fraught with errors due to the presence of large interparticle spaces.[40] A zeolitic imidazolate MOF proposed for hydrogen storage,[11] ZIF-8 was predicted to have a low thermal conductivity by molecular dynamics simulation.[41] These prior studies were only for empty lattices without adsorbed gases, which obstructs our understanding on how or whether the adsorbed gas affects heat transport within the lattice

of the MOFs. Recently, two computational studies predicted opposite trends of the effect of gas adsorption on the MOF thermal conductivity.[42, 43] The discrepancies in these studies necessitate reliable experimental studies of thermal conductivity in the presence of gas adsorbents at various pressures.

Herein, we demonstrate a thin-film based approach for measuring the thermal conductivities of MOFs prepared as thin films, which could avoid the growth challenge of large crystals and compressed pellets of MOF. As a case study, ZIF-8 was selected due to its known chemical and thermal stability.[3] Thermal conductivity measurements were conducted on solvothermally prepared ZIF-8 thin films at room temperature in air or nitrogen, or in perfluorohexane (C_6F_{14}) vapor at variable pressures. Considering the potential hazard of using flammable gases in the electrical circuit setup and in the air, the inert vapor perfluorohexane was used as a substitute for fuel gases such as methane, ethane and propane. The results offer experimental insights towards the possible effects of adsorbed gas molecules on the thermal conductivity of the ZIF-8 host.

2.2. Film Growth and Morphology

ZIF-8 films were grown with good thickness control on oxide-terminated silicon with an alumina adhesion layer (2 nm $AlO_x/300$ nm SiO_x/Si) by first quickly immersing the substrate in a beaker containing a freshly prepared methanolic solution of 2-methylimidazole (2-MeIm) and $Zn(NO_3)_2 \cdot 6H_2O$ at room temperature, as has been described elsewhere.[44] By replacing the fresh methanolic solution five times every 30 minutes, a final film of ZIF-8 was obtained with a thickness of $t = 300$ nm. The ZIF-8 film is a smooth and

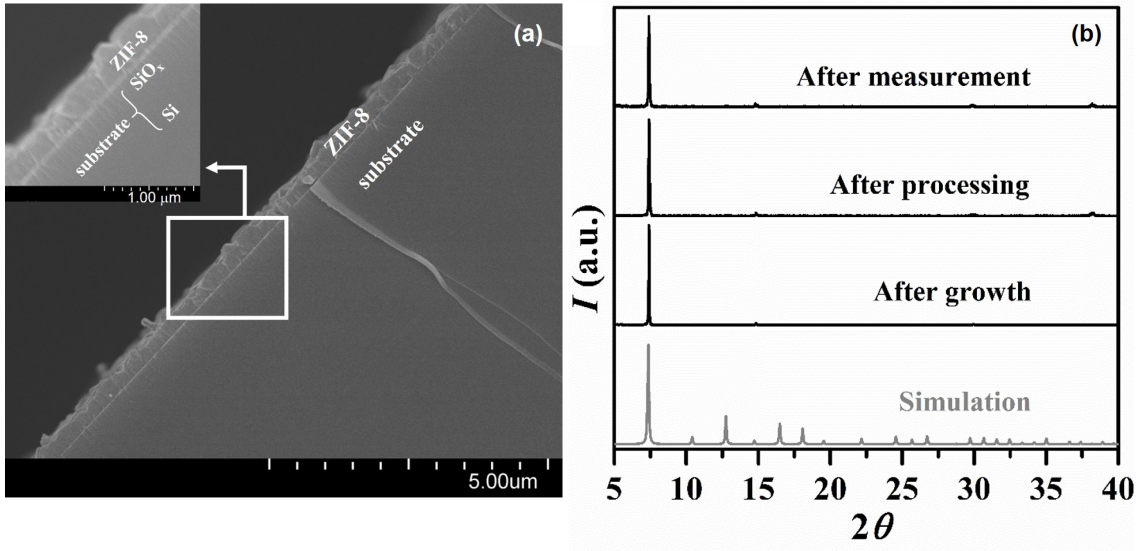


Figure 2.1. Morphology of ZIF-8 film. (a) Cross-sectional SEM images of as-grown ZIF-8 thin film. (b) X-ray diffraction patterns of ZIF-8 thin films during the study cycle (black) compared with simulation result (grey).

uniform layer on a SiO_x/Si substrate, as illustrated in the cross-sectional scanning electron microscope images Figure 2.1(a). Prior to imaging, activated MOF samples were coated with either a film of Au/Pd or Os with a 10~20 nm thickness). X-ray diffraction (XRD, $\text{Cu K}\alpha$ $\lambda = 1.54 \text{ \AA}$) patterns on the thin films confirm the crystallinity of ZIF-8 thin films throughout the measurement cycle. The results are shown in Figure 2.1(b). Except for the peak of Au contacts ($2\theta = 38.2^\circ$, from Au [111] contacts) all the peaks are consistent with the simulation, and the highest-intensity peak occurs at $2\theta = 7.4^\circ$ indicating the dominant crystal orientation of ZIF-8 [110]. Given the possibility of slow hydrothermal degradation[45, 46] of ZIF-8, XRD measurements were conducted multiple times throughout this study over the course of several days (*i.e.*, after synthesis, between processing steps, and after measurements), and it was ascertained that the crystallinity was maintained during the thermal conductivity study.

2.3. Thermal Characterization: 3ω Method

Thermal conductivity describes the capability of materials to conduct heat, which is defined by the Fourier's law:

$$(2.1) \quad \mathbf{Q} = -\kappa \cdot \nabla T.$$

It states that the heat flux density \mathbf{Q} is proportional to the negative temperature gradient $-\nabla T$ with the ratio κ as thermal conductivity.

The 3ω method is one of the most widely used methods for thermal conductivity measurement[47]. Compared with other thermal conductivity measurements[48, 49, 50], it greatly reduces the heat radiation loss, requires no sophisticated equipment setup (such as lasers), and is relatively easy to be implemented under various environments (such as changing temperature, pressure, and gas environments, etc.) for dependence study. A gold filament is deposited onto the film of interest, with comparison to another identical filament on bare substrate. An ac current in the form

$$I_\omega = I_0 \cdot e^{i\omega t}$$

with the frequency of ω is applied through the filaments, generating a Joule heating

$$Q_{2\omega} = Q_0 \cdot e^{2i\omega t}$$

in the frequency of 2ω , and consequently a temperature oscillation $T_{2\omega}$ also in 2ω . Given that the metal filament resistance is linear with temperature at most temperature range,

there would be filament resistance oscillations

$$\Delta R_{2\omega} = \frac{dR}{R dT} T_{2\omega} R$$

also in the frequency of 2ω . The term $\alpha = \frac{dR}{R dT}$ is a constant considered as the temperature coefficient of the metal, and can be determined during a slow temperature change. As a result, there will be a third harmonic term in the voltage across the filament

$$V_{3\omega} = I_{\omega} \cdot \Delta R_{2\omega} \sim e^{3i\omega t}.$$

The gold filaments act as both heater for ac current heating, and thermometer for ac temperature oscillation measurement. Standard lock-in techniques were employed to extract the third harmonic term of the voltage across the filament relative to a dummy resistor with identical nominal resistance as the filament. Depending on the width of the filament relative to the film thickness, using 3ω method is able to determine both cross-plane and in-plane thermal conductivity. Given the isotropic structure and estimated short mean-free-path of phonons in ZIF-8, cross-plane thermal conductivity is measured in the project.

Cross-plane thermal conductivity is derived when the heat flow is predominantly in the vertical cross-plane direction. This condition can be met when the heating filament width is much larger than the thickness of the film. By using the differential 3ω method[47, 51], the temperature oscillation across the film is compared between samples with and without the film of interest.

Given the measurement 3ω voltage $V_{3\omega}$ across the filament due to heating and the originally applied 1ω voltage $V_{1\omega}$, the temperature oscillation $T_{2\omega}$ at a frequency of 2ω

can be deduced as:

$$(2.2) \quad T_{2\omega} = 2 \frac{dT}{dR} \frac{R}{V_{1\omega}} V_{3\omega}$$

The temperature difference between the filaments with and without the underlying film $\Delta T_{2\omega,f}$ is the 2ω temperature difference across the IGZO film of interest, giving the film thermal conductivity as follows[51]:

$$(2.3) \quad \kappa_f = \frac{Pt}{2bl\Delta T_{2\omega,f}}$$

where P is the ac heating power, t is the thickness of the film, l and b are the length and half-width of the filament, respectively. 3ω voltage signal in our measurement is at least four orders of magnitude lower than the heating voltage in 1ω . Although lock-in amplifier is capable of extracting the minuscule $V_{3\omega}$ from $V_{3\omega}$, the experimental noise sometimes still a considerable factor in uncertainty. So optionally another circuit connection using Wheatstone bridge is able to minimize the noise and help improve the error bar, which is described in Appendix 1.

Gold filaments were processed onto ZIF-8 thin film was processed to facilitate the 3ω measurement. After spinning photoresist and subsequent photolithography patterning, a 10-nm thick chromium adhesion layer was deposited by thermal evaporation, followed by a 100-nm thick gold layer. Twin filaments were patterned both on the ZIF-8 film and atop a blank substrate. After photoresist lift-off, the ZIF-8 sample was then baked in vacuum at 100° for 2 hours to evacuate the ZIF-8 pores of any solvent molecules introduced during processing. Finally, gold wires were attached with indium onto the contact pads for measurement [Figure 2.2(a)]. Multiple filaments were usually made on

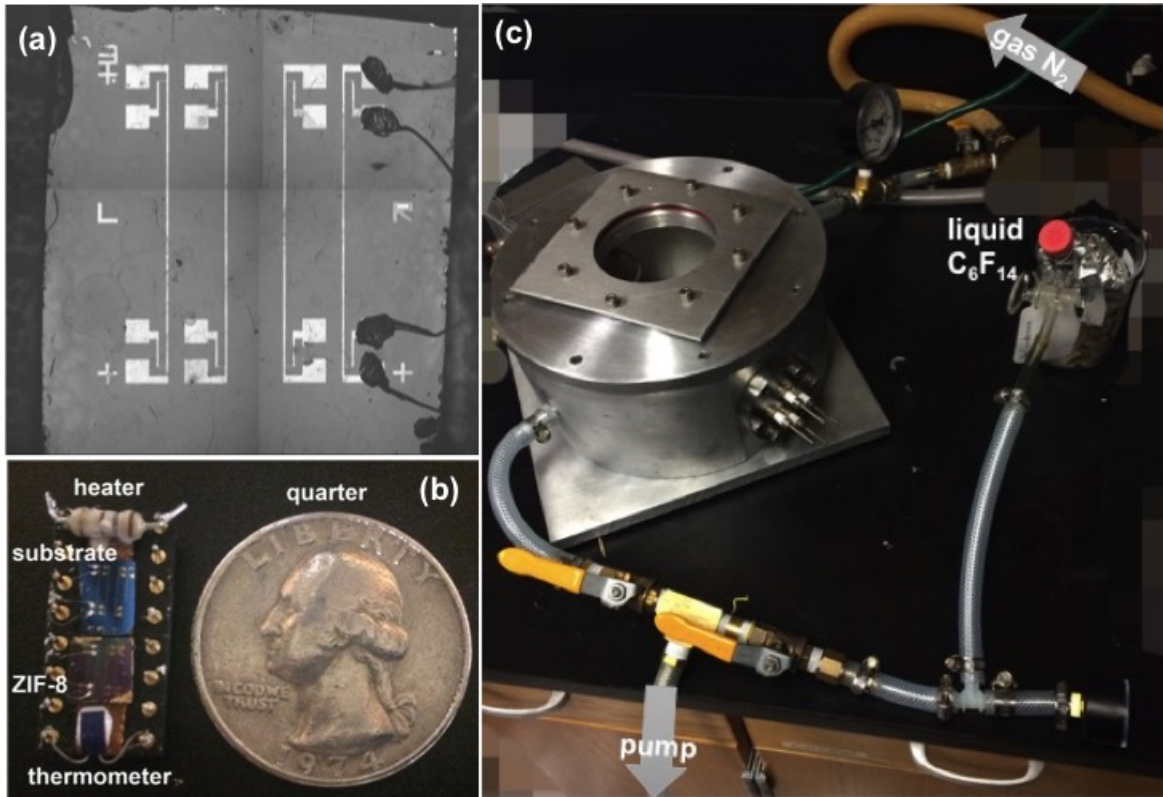


Figure 2.2. Pictures of processed sample, measurement device and setup. (a) Optical profiler image of the processed sample showing the photolithography pattern on ZIF-8 film with measurement contacts, where the filament with the best microscopic morphology is picked for gold-wire contact and final measurement. (b) Real measurement device compared with a quarter. (c) Measurement chamber with N₂ and C₆F₁₄ sources

each sample, in which sections with the best adhered filament were used for measurement. The measurement device was made by putting the sample with ZIF-8 film alongside a bare substrate sample with the identical filament pattern as shown in Figure 2.2(b)], where the thermometer and resistive heater are used to determine temperature coefficient dR/RdT of the filaments. By measuring the difference between the sample with film and that of the bare reference substrate, the cross-plane thermal conductivity can be determined

given the fact that the filament width ($w = 30 \mu\text{m}$) is much larger than the film thickness ($t = 300 \text{ nm}$), so that the heat flow through the film is primarily in the vertical direction.

ZIF-8 thin film samples were measured in a chamber with inlets connected to a N_2 cylinder and a liquid perfluorohexane bottle, and an outlet connected to a mechanical pump. The setup is shown in [Figure 2.2(c)]. The sample was first measured in air, and then in vacuum after pumping for at least 20 min. To change the gas environment in the chamber (to either N_2 or C_6F_{14}), the desired gas was fed into the chamber using the connecting valve, while the valves of the other gas supply and vacuum pump were kept closed. For N_2 , the valve inlet was closed once the desired pressure in the chamber was obtained. For C_6F_{14} , additional time was allowed for the vapor of C_6F_{14} bottle to equilibrate through the chamber at the specified pressure. After measurement, the chamber was vented from vacuum to the highest partial pressure used in the measurement, and then pumped carefully back to each chosen partial pressure before reaching vacuum, and finally vented with N_2 to air pressure.

2.4. Gas Adsorption in ZIF-8

The adsorption isotherm results of ZIF-8 in N_2 and C_6F_{14} are shown in Figure 2.3. The so-called adsorption isotherm is to examine the gas loading at different pressures by measuring the mass change of the sample in adsorption equilibrium under a certain gas environment. The N_2 sorption isotherms at 298 K and subsequently at 77 K were measured, and the results are shown in Figure 2.3(a). At room temperature N_2 adsorption is rather negligible, as seen in the 298 K curve at the bottom of Figure 2.3(a) ($2.5 \text{ cm}^3/\text{g}$; $\sim 0.6\%$ total surface capacity). The observed shallow linear N_2 adsorption [Figure 2.3(a)

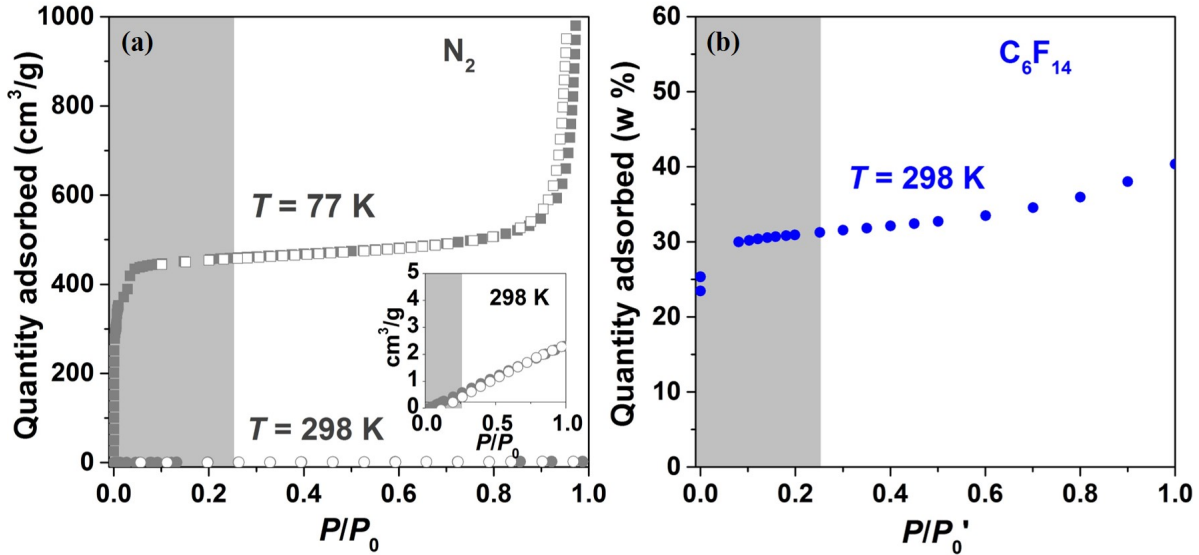


Figure 2.3. Isotherm results of ZIF-8 in (a) N_2 environment and (b) C_6F_{14} environment, where the grey area below P/P_0 and $P/P'_0 = 0.25$ indicates the pressure window where the thermal conductivity was measured. On the left figure P_0 is the saturation pressure of nitrogen, while on the right figure P/P'_0 corresponds to the partial pressure (0-100)% of C_6F_{14} . Adsorption and desorption processes are demonstrated by filled and open symbols, respectively.

inset] is consistent with the sorbates minuscule molecular polarizability and, therefore, weak van der Waals interaction with the framework. In contrast, at low temperature, significant physisorption of N_2 is possible. For a prepared bulk ZIF-8 sample, N_2 adsorption at $T = 77\text{ K}$ culminates in pore saturation at $437\text{ cm}^3/g$ around $P/P_0 = 0.05$. Unlike N_2 , C_6F_{14} shows significant adsorption with a 30% weight adsorption even at room temperature in Figure 2.3(b), which is equivalent to approximate 23 C_6F_{14} molecules per unit cell of ZIF-8. The adsorbed mass at a given relative pressure point was the difference of mass gain at that point relative to the mass recorded in dry N_2 flow.

For C_6F_{14} , a kinetic adsorption measurement was further conducted as shown in Figure 2.4. By 3 minutes the adsorption loading was stabilized at $10\text{ }\mu\text{g}/\text{cm}^2$, corresponds

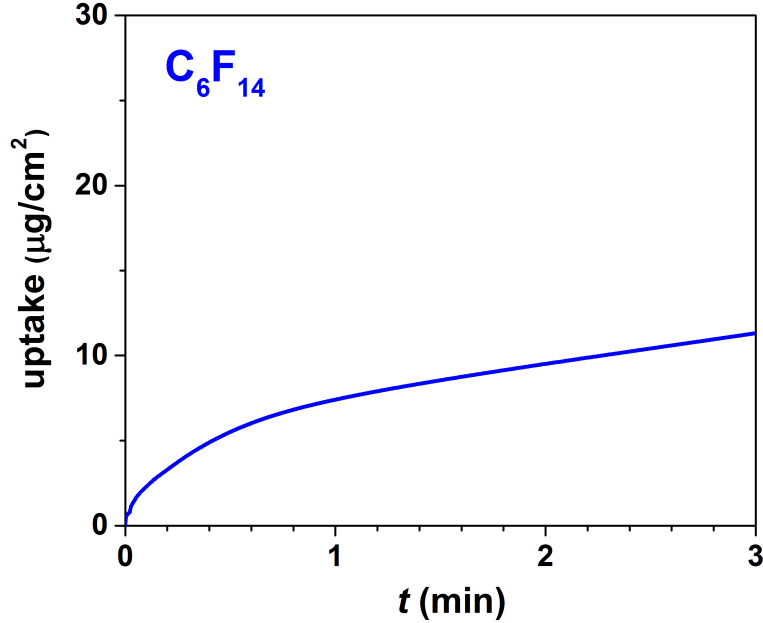


Figure 2.4. Time-dependent adsorption measurement of C_6F_{14} in ZIF-8.

to approximately two C_6F_{14} molecules per unit cell. So at each designated pressure, the sample was allowed to stabilize in the chamber for at least 3 minutes prior to measurement in order to ensure enough time for adsorption equilibrium.

2.5. Thermal Conductivity Under Ambient Gas Pressure

The measured thermal conductivity (κ) of ZIF-8 thin films are shown in Figure 2.5. The in-air thermal conductivity is reproducible among three different thin film samples ($\kappa_{\text{sample1}} = 0.33 \text{ W}/(\text{m} \cdot \text{K})$, $\kappa_{\text{sample2}} = 0.29$, and $\kappa_{\text{sample3}} = 0.23 \text{ W}/(\text{m} \cdot \text{K})$) and slightly higher than the predicted ZIF-8 value ($\kappa = 0.165 \text{ W}/(\text{m} \cdot \text{K})$), confirming the expected order of magnitude.[41] The effect of adsorbed gas analytes was then studied with the benefit of our controlled gas chamber set-up demonstrated in Figure 2.2(c). Thermal

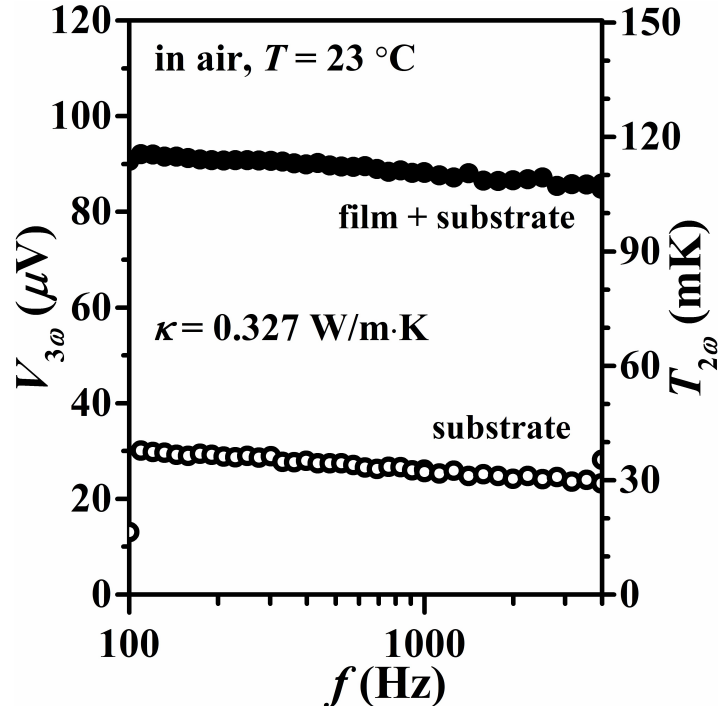


Figure 2.5. The 3ω data of ZIF-8 thin film in air at room temperature.

conductivity of the ZIF-8 film was observed to change by less than a percent in the presence and absence of different gas analytes. The thermal conductivity results of ZIF-8 films are shown in Figure 2.6(a) for C_6F_{14} (blue) and N_2 (grey) environments as compared to ambient air ($P_{\text{gauge}} = 1 \text{ atm}$) and house vacuum ($P_{\text{gauge}} = 0.02 \text{ atm}$) measurements. As shown for the C_6F_{14} ambient pressure (Figure 2.6(a), blue) the lowest thermal conductivity occurs in vacuum. As the gas pressure of C_6F_{14} increases to its vapor pressure the thermal conductivity of the ZIF-8 thin film only slightly increases by 1% despite appreciable adsorption of C_6F_{14} to the MOF surface at these relative pressures as indicated by a C_6F_{14} isotherm. Interestingly, when the thin films were re-exposed to nitrogen atmosphere (grey) from vacuum, the thermal conductivities exhibited a similar trend to the films that

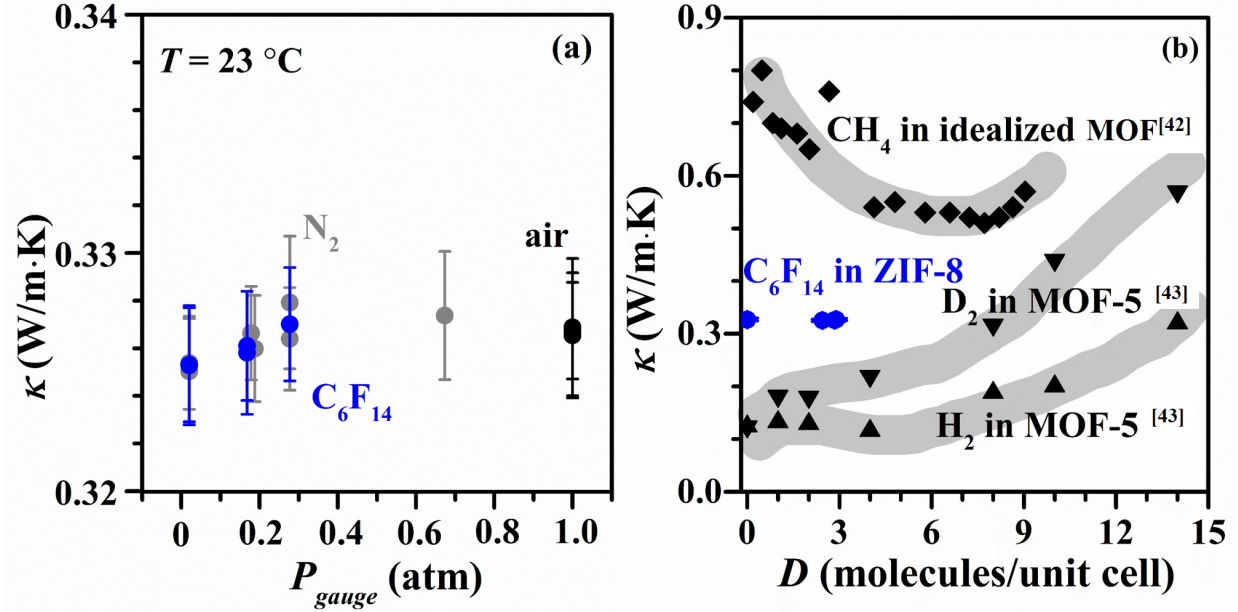


Figure 2.6. (a) Measured thermal conductivity of ZIF-8 thin film during the gas tests in N_2 and C_6F_{14} . The error bars are derived from the statistical standard deviation of 3ω voltage at various frequencies between $f = 100$ and 4,000 Hz. The measurements were taken at least three minutes after stabilizing at each partial pressure to make sure that the adsorption amount was steady (b) Comparison of the experimental pressure-dependent thermal conductivity of this work (blue) with prior simulation[42, 43] (black), with guides to the eye (grey) to illustrate trends.

were exposed to perfluorohexane vapor pressure ($P_{gauge} = 0.28$ atm, blue) although the N_2 adsorption is proved to be negligible at room temperature [Figure 2.3(a)].

The pressure study can be modeled equivalently in terms of number of molecules per ZIF-8 unit cell. Figure 2.6(b) converts the pressure-dependent thermal conductivity result in Figure 2.6(a) to the molecule density scale using the isotherm results in Section 2.4. In our measurement results (blue), C_6F_{14} has an approximate density of $D = 2\sim 3$ C_6F_{14} molecules per unit cell of ZIF-8 as estimated from the corresponding isotherm data in Figure 2.3(b). However, this saturated amount of C_6F_{14} inside ZIF-8 seems to neither

hinder heat transfer by phonon scattering with host lattice, nor enhance the thermal transport through gas molecules in voids, unlike the predicted increasing[43] or decreasing[42] trend in prior simulations on other MOFs with different adsorbed gases [black symbols and grey shaded guides to the eye in Figure 2.6(b)]. While surprising, it is possible that the proposed[43] enhancement in lattice thermal conductivity due to the additional heat transfer channels provided from the adsorbed gas molecules, may be minimal for C_6F_{14} , which has a very low thermal conductivity ($\kappa_{liquid} = 0.056 \text{ W}/(\text{m} \cdot \text{K})$)[52] in comparison to other fuel gases such as hydrogen[53] ($\kappa_{gas} = 0.18 \text{ W}/(\text{m} \cdot \text{K})$). Note that even for hydrogen, the thermal conductivity of MOF with adsorbed hydrogen[43] does not show significant increase below a certain adsorption threshold ($D = 4$ molecules per unit cell). On the other hand, in comparison to CH_4 , the heavier gas molecule C_6F_{14} is more likely to induce phonon scattering effects than CH_4 . However, contrary to predictions in the Babei *et al*s simulated work, any scattering effects from C_6F_{14} did not seem to affect the thermal conductivity of ZIF-8.

In conclusion, the thermal conductivity of ZIF-8 was measured experimentally for the first time with thin film studies. Additionally, we demonstrated a way to conduct in-situ measurements at room temperature under different gases and pressures. The results show reproducibility among samples, and vacuum thermal conductivities compare favorably to prior simulation studies on MOFs. From the series of gas adsorption tests investigated, ZIF-8 thin-film thermal conductivity is slightly lower in vacuum than that in air by about 1%, but generally independent of the presence of gas molecules regardless of the quantity adsorbed by the MOF up to atmospheric pressure. While the thermal conductivity in ZIF-8 is relatively unaffected by adsorbed gases and vapors, it is possible that such an

effect might be more pronounced at higher pressures and with more thermally conductive sorbates. This technique demonstrates a viable pathway for obtaining MOF thermal conductivities to probe these effects in future studies.

2.6. Future Work

Unlike simulation studies of adsorption-dependent thermal conductivity of MOF, the real experiment is limited by the amount of adsorption molecule density in order to see a pronounced trend of thermal conductivity change with gas adsorption. In the future it may help to select a gas adsorbate that has a higher vapor pressure or higher saturation pressure, which would lead to larger gas molecule density. Our chamber setup is robust enough to hold positive pressures. Specifically, gases with a heavier molecular weight may have larger scattering effect on thermal conductivity, as long as the molecule is not too big to prevent it from entering the MOF lattice. On the other hand, gases with higher thermal conductivity may induce more enhancement in MOF lattice for heat transport, for example hydrogen and helium gases. Given the safety concern of having H_2 in a circuit setup, helium may be a more practical adsorbate. But helium adsorption in MOFs is usually considered to be negligible at room temperature and ambient pressure, which is the reason for using He as a carrier gas in adsorption measurements.[54, 55]

Another future study is the temperature dependence measurement of MOF thermal conductivity. Prior simulation predicted that the temperature effect would be trivial on MOF-5 thermal conductivity[38] between $T = 200$ and 400 K, which was further proved experimentally between $T = 200$ and room temperature on MOF-5 single crystals[39]. But it would be advantageous to verify those predictions at higher temperatures or on

other MOFs in our measurement chamber, where the sample temperature could be raised above room temperature by employing the integrated Peltier cooler unit. Because the molecular dynamics simulation is based on ideal assumptions that could be different in real experiments and applications, and higher temperature condition would be of more interest for studying the exothermic process of fuel gas adsorption.

Based on the 3ω method, a new approach called “buried 3ω ” needs to be developed in the future where the filaments are buried *below* the film. In this method, the filaments are deposited prior to the film of interest, so it would be possible to measure a film with a high porosity or a rough surface morphology. The method philosophy be similar to those implemented on metal inverse opals[56] and nanowire arrays[57], but not just sensitive to high- κ films. More theoretical derivation and Matlab simulation need to be developed to prove the method feasibility before experimental implementation.

CHAPTER 3

Indium Gallium Zinc Oxide Thermal Conductivity and Morphology Comparison

This chapter comprehensively studies the thermal conductivity of IGZO thin films fabricated with different techniques, given the prior research reviewed in Section 3.1. Section 3.2 describes the diverse growth methods of thin-film IGZO, as well as the post-growth sample processing for facilitating thermal conductivity measurement. Section 3.3 introduces the two theoretical approaches in this study: molecular dynamics simulations and a minimal thermal conductivity model. Section 3.4 summarizes the results of film morphology study using X-ray and temperature-dependent thermal conductivity measurement using 3ω method. Section 3.5 discusses the morphology-property correlation and analyzed the thermal conductivity dependence of IGZO thin films on temperature, crystallinity, porosity and shelf-time.

3.1. Prior Research

To our knowledge, there are only a few prior comparative studies on crystalline, semi-crystalline, and amorphous IGZO thermal conductivity κ , and those were conducted at room temperature, only. Seo *et al.*[27] studied the thermoelectric performance of sputtered IGZO thin films and reported that, remarkably, the more ordered crystalline film has a factor of 7 *lower* thermal conductivity than the less ordered semi-crystalline film. This counter-intuitive variation of thermal conductivity on morphology begs confirmation,

as well as motivating a more detailed temperature-dependent study to achieve a better understanding of the underlying physics. Thermal conductivity for sputtered a-IGZO thin films[58] was also reported, but again only at room temperature, thereby limiting the utility in comparing with theory.

This work will examine the temperature-dependent thermal conductivity of IGZO thin films fabricated with different techniques that are systematically analyzed and compared. Growth methods for comparison include pulsed laser deposition (PLD), sputtering, and spray-[59] and spin-combustion[18] solution processing. Among the PLD films, a series was grown under different conditions to vary the crystallinity, from amorphous (a-), to semi-crystalline (semi-c-), to single-crystal-like (c-) phases. Ab-initio molecular dynamics is also employed to determine the local structure of amorphous IGZO and to compare the room-temperature atomic displacements in a- and c-IGZO. X-ray studies, including X-ray diffraction (XRD), grazing incidence wide angle scattering (GIWAXS) and X-ray reflectivity (XRR), complement the thermal conductivity studies to assess the film density, porosity, crystallinity, and crystal orientation of the films processed by various means.

Following the theoretical literature, we will adopt the term “vibrons” [60] to refer to the generic vibrational modes responsible for thermal transport in amorphous materials, since, strictly speaking, phonons represent relevant modes of heat propagation only in crystalline materials. We note that in all morphologies, the heat is primarily conducted through vibrons rather than electrons, because even for highly doped IGZO films with electrical conductivity $\sigma = 100$ S/cm the electronic contribution to the thermal conductivity is only $\sigma_e = 7.3 \times 10^{-2}$ W/(m·K) according to Wiedemann–Franz law — less than 10% of even the poorest thermally conducting PLD film. The electrical conductivity σ of IGZO can be

tuned in a wide range[19] ($\sigma = 10^{-3} \sim 10^2$ S/cm) to target various applications, but all the films under study were grown to have relatively low $\sigma < 5 \times 10^{-1}$ S/cm to guarantee negligible electron contribution to the thermal conductivity.

3.2. Film Preparation

3.2.1. Film Growth Techniques

Three different IGZO growth techniques were used: two physical deposition methods (PLD and sputtering) and one chemical synthesis method (combustion-based solution process). To facilitate thermal conductivity measurements, all films were grown on sapphire substrates for their high thermal conductivity.

We first discuss the PLD films. Film growth was carried out with a $\lambda = 248$ nm KrF excimer laser having a $\Delta t = 25$ ns pulse duration and operated at $f = 2$ Hz. $\text{InGaO}_3(\text{ZnO})_1$ films of $d = 200$ nm thickness were grown by PLD from dense, hot-pressed targets (25 mm diameter). The $E = 200$ mJ/pulse beam was focused onto a 1.5 mm \times 2.5 mm spot size. The target was rotated at 5 rpm to prevent localized heating, and fixed at 10 cm away from the substrates. The deposition oxygen ambient pressure for all films was 25 mTorr.

For PLD films, X-ray diffraction revealed how different substrate growth temperatures could induce morphologies from crystal-like to amorphous, as well as an intermediate morphology exhibiting both crystalline and amorphous features (semi-crystalline)[61]. Single-crystal-like $\text{InGaO}_3(\text{ZnO})_1$ films (c-IGZO) were grown by first depositing a thin (5 nm) ZnO film at 700 °C from a ZnO target prior to the 200 nm thick IGZO film at 600 °C from a $\text{InGaO}_3(\text{ZnO})_2$ target. The relatively low deposition temperature for the IGZO was used to prevent excessive loss of zinc. The film was then post-annealed at

900 °C for 9 hours. Semi-crystalline $\text{InGaO}_3(\text{ZnO})_1$ films (semi-c-IGZO) were grown by depositing an IGZO film directly on sapphire at 600 °C from a $\text{InGaO}_3(\text{ZnO})_2$ target, followed by a post anneal at 600 °C for 6 hours. During the anneal of c- and semi-c-IGZO, further loss of zinc is prevented by placing a blank sapphire substrate over the film, and the stoichiometry of $\text{InGaO}_3(\text{ZnO})_1$ for the finished films was confirmed by the energy dispersive spectrum (EDS). The amorphous films were deposited by PLD at 25 °C, hence, the loss of zinc was relatively minor; three targets were used to deposit the amorphous $\text{InGaO}_3(\text{ZnO})_1$ films: $\text{InGaO}_3(\text{ZnO})_2$, ZnO, and Ga_2O_3 targets. They are deposited in a cyclic fashion, 32 pulses $\text{InGaO}_3(\text{ZnO})_2$, 4 pulses ZnO, 4 pulses Ga_2O_3 ; EDS confirms a stoichiometry of $\text{InGaO}_3(\text{ZnO})_1$. Note: To deposit a monolayer of $\text{InGaO}_3(\text{ZnO})_2$ would require an excess of 40 pulses, hence, the three constituents of the film described above are not stratified but mixed on a sub unit-cell level. A computer controlled shuttle was used to alternate ablation between targets. No post deposition anneal was required for the amorphous films.

Sputtered a-IGZO films were grown by magnetron sputtering under an Ar and O_2 mixture (Ar : O_2 = 20 sccm : 1 sccm, deposition pressure $P = 3 \times 10^{-3}$ Torr) using a target with In:Ga:Zn ratio of 1:1:1, to match the PLD stoichiometry. The films were annealed in air at 350 °C for 1 hour after deposition, resulting in 50-nm-thick films on sapphire substrates.

For solution-processed a-IGZO, both spray combustion synthesis[59] and spin-coating combustion synthesis[18] were used to deposit the films. Solutions were prepared with $\text{In}(\text{NO}_3)_3 \cdot x\text{H}_2\text{O}$, $\text{Zn}(\text{NO}_3)_2 \cdot x\text{H}_2\text{O}$, and $\text{Ga}(\text{NO}_3)_3 \cdot x\text{H}_2\text{O}$ in 2-methoxyethanol to yield a 0.05 M metal concentration. Next, 55 μL NH_4OH and 100 μL acetylacetone were

added into 10 mL of the metal nitrate solutions and stirred overnight at 25 °C. Prior to spray- or spin-coating, the precursor solutions were combined in the same molar ratio In:Ga:Zn= 1 : 1 : 1, and stirred for 2 hours. For spray-coating, substrates were maintained at 300 °C on a hot plate while 0.05 M precursor solutions were loaded into the spray gun and sprayed intermittently (60 s cycles) onto sapphire substrates until the desired thickness (50 nm) was obtained. The nozzle-substrate distance was 20 cm. For multilayer 50-nm thick spin-coated devices, 0.05 M precursor solutions were spun at 3500 rpm for 30 s, and then annealed for 10 min at 300 °C; this was repeated 15 times to achieve the desired thickness. For one-step 50 nm single-layer devices, precursor solutions with concentrations of 0.5 M were spin-coated at 2000 rpm for 60 s, and then annealed for 30 min. All solution processed films were then post-annealed at 300 °C for 1 hour in clean dry air.

3.2.2. Sample Processing

Several processing steps were conducted on the films to enable the 3ω measurements. An 80-nm-thick SiN_x layer was deposited by plasma enhanced chemical vapor deposition (PECVD) at 300 °C on all the samples to electrically isolate the IGZO films,¹ followed by photolithographically patterned gold filaments deposited by thermal evaporation and lift-off. The gold filaments are typically 120 to 150 nm thick with a 10-nm chromium adhesion layer underneath. The width of the gold filament is $2b = 30 \mu\text{m}$, designed to be much larger than the thickness of the films ($t = 200 \text{ nm}$ for the PLD-grown films, and

¹For all the samples the leakage resistance between the filament and substrate exceeded $1 \text{ G}\Omega$, except for the spray-combustion film ($R \sim 0.5 \text{ M}\Omega$), whose behavior was consistent with other films of comparable density. So we include this data for completeness but with larger error bars in Figure 3.5(b), arising from the power dependence of the thermal conductivity.

$t = 50$ nm for the sputtered and solution-processed films) so the heat flow is predominantly in the vertical cross-plane direction. The completed devices were loaded into an Oxford variable temperature insert (VTI) helium gas flow cryostat with coaxial shielded leads for temperature dependence study ranging from $T = 18$ to 300 K.

3.3. Simulation and Modeling

3.3.1. Ab Initio Molecular Dynamics Simulation

Molecular dynamics simulations were carried out to determine the atomic structure of a- and c-IGZO in order to better explain the thermal conductivity results. The atomic structures of all the three phases are illustrated in Figure 3.1, whereby panel (a) is a molecular dynamic simulation of the amorphous phase, panel (c) is the known superlattice-like structure of the crystalline phase, and panel (b) is schematically drawn to have intermediate order between these two extremes, representing the semi-crystalline phase. Amorphous InGaZnO structure was generated using first-principles molecular dynamics liquid-quench simulations as implemented in the Vienna Ab-initio Simulation Package (VASP)[62, 63, 64, 65]. The calculations are based on density functional theory within generalized gradient approximation (GGA) with the PBE (PerdewBurkeErnzerhof) functional[66]. The initial cell $\text{In}_{18}\text{Ga}_{18}\text{Zn}_{18}\text{O}_{72}$ with rhombohedral structure and a density of $\rho = 6.33$ g/cm³ was melted at $T = 3000$ K for 6 ps to remove the crystalline memory; the melt was then rapidly quenched to $T = 100$ K at the rate of 200 K/ps. These simulated cooling rates are known from previous work[61] to effectively match the coordination number of atoms in the simulated film to X-ray scattering data from experimental amorphous films grown at the substrate temperatures investigated here. During

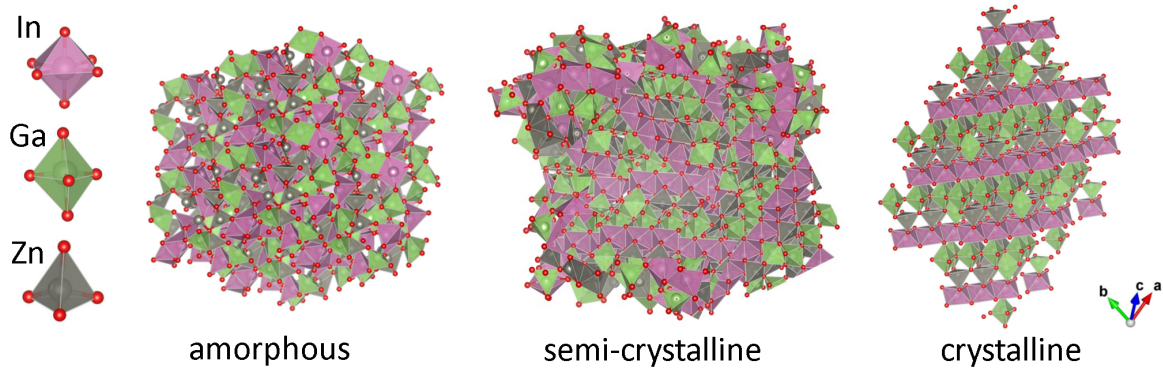


Figure 3.1. (a) The atomic structure of amorphous IGZO calculated from ab-initio molecular dynamics liquid-quench simulations (b) Schematic representation of semi-c-IGZO, indicating more order than amorphous, but less order than crystalline. (c) Crystal structure of rhombohedral InGaZnO_4 , where the Ga and Zn atoms are distributed randomly within the double layer. The small red spheres represent oxygen atoms, and cations are shown as polyhedrals.

melting and quenching processes, a cut-off energy of $E = 260$ eV was used and the k-point sampling was restricted to Γ -point only. Finally, the structure was equilibrated at $T = 300$ K for 6 ps with a cut-off energy of $E = 300$ eV. All simulations were carried out within NVT ensemble with Nose-Hoover thermostat using integration time step of 2 fs. The resulting atomic structures were plotted using VESTA software[67]. For crystalline InGaZnO_4 , the experimental crystal structure was employed and the atomic coordinates were optimized using ab-initio density functional calculations[68].

3.3.2. Modeling: Porosity-adapted Cahill-Pohl (p-CP) Model

Because we anticipate particularly low thermal conductivity for our amorphous materials, we consider a simplified limit-case model proposed by Cahill and Pohl[69, 70] which predicts a lower bound or minimal thermal conductivity κ_{\min} . In the model, heat

is transmitted by the random walk of damped and localized Einstein oscillators having different sizes and frequencies such that they follow the density of states of an acoustic phonon mode. The generalized argument proposes that physically decoherent but coupled atoms cannot have a lower thermal conductivity than $\kappa_{\min}(T)$, with a wealth of experimental data on bulk materials and thin films cited therein to support this conclusion. The minimum thermal conductivity of an amorphous material is expressed as [70],

$$(3.1) \quad \kappa_{\min}^{\text{CP}}(T) = \left(\frac{\pi}{6}\right)^{\frac{1}{3}} k_B n^{\frac{2}{3}} \sum_i v_i \left(\frac{T}{\Theta_i}\right)^2 \int_0^{\frac{\Theta_i}{T}} \frac{x^3 e^x}{(e^x - 1)^2} dx,$$

where k_B is Boltzmann constant, n is the atom density per unit volume, v_i the speed of sound for each polarization i , and $\Theta_i = v_i(\hbar/k_B)(6\pi^2 n)^{1/3}$, the Debye cutoff frequency expressed as a temperature. The sound velocity of two transverse modes (i.e. shear) v_s and one longitudinal mode (i.e. compression) v_c can be determined as[71, 72]:

$$(3.2) \quad v_s = \sqrt{G/\rho_f}, \quad v_c = \sqrt{(K + \frac{4}{3}G)/\rho_f},$$

$$G = \frac{E}{2(1 + \nu)}, \quad K = \frac{E}{3(1 - 2\nu)}$$

where shear modulus G , bulk modulus K can be determined from Young's modulus E and Poisson's ratio ν .

Considering that all the films under study have different levels of porosity ($P = 4-40\%$ as shown in Table 3.1), the CP minimum thermal conductivity here has been adapted for porosity (p-CP model):

$$(3.3) \quad \kappa_{\min}(T) = f(P) \cdot \kappa_{\min}^{\text{CP}}(T),$$

where $f(P)$ is a porosity-adjusted factor that links the porous-film thermal conductivity κ to the dense counterpart κ_0 . This factor will be discussed further with two models in Section 3.5.2.

3.4. Results of Morphology and Thermal Conductivity

3.4.1. Film Morphology Results

Before the 3ω processing and measurement, the morphology of the three PLD samples with different crystallinities were examined both by XRD (Cu K α $\lambda = 1.54 \text{ \AA}$) as shown in Figure 3.2(a), and by GIWAXS at the synchrotron (20 keV, $\lambda = 0.62 \text{ \AA}$) with a two-dimensional detector (MarCCD 165) as shown in Figure 3.2(c)-(e). Since data were measured with different incident wavelengths, all figures were plotted as a function of $Q(= 4\pi\sin(\theta)/\lambda)$ for comparison. The simulated IGZO and Al₂O₃ powder diffraction spectra were generated by CrystalMaker® software based on crystal structural information obtained from inorganic crystal structure database (ICSD 247980 for IGZO and 10425 for Al₂O₃) with Cu K α wavelength as shown in (a) and (b) as dashed peaks, in order to determine the Miller indices and separate the substrate and film diffraction peaks, respectively. The amorphous film grown by PLD shows no crystalline diffraction peaks in the XRD pattern in Figure 3.2(a), and presents an amorphous diffraction halo in the 2D GIWAXS image Figure 3.2(c). For semi-c- and c-IGZO films, there are strong diffraction peaks in Figure 3.2(a) and diffraction rings in Figure 3.2(d) and (e), respectively, which indicates semi-crystalline structures and highly oriented features along the c-axis of the IGZO crystals in both films. The Miller indices of each diffraction peak were identified by matching with a simulated IGZO spectrum. Grain size analysis was performed by using

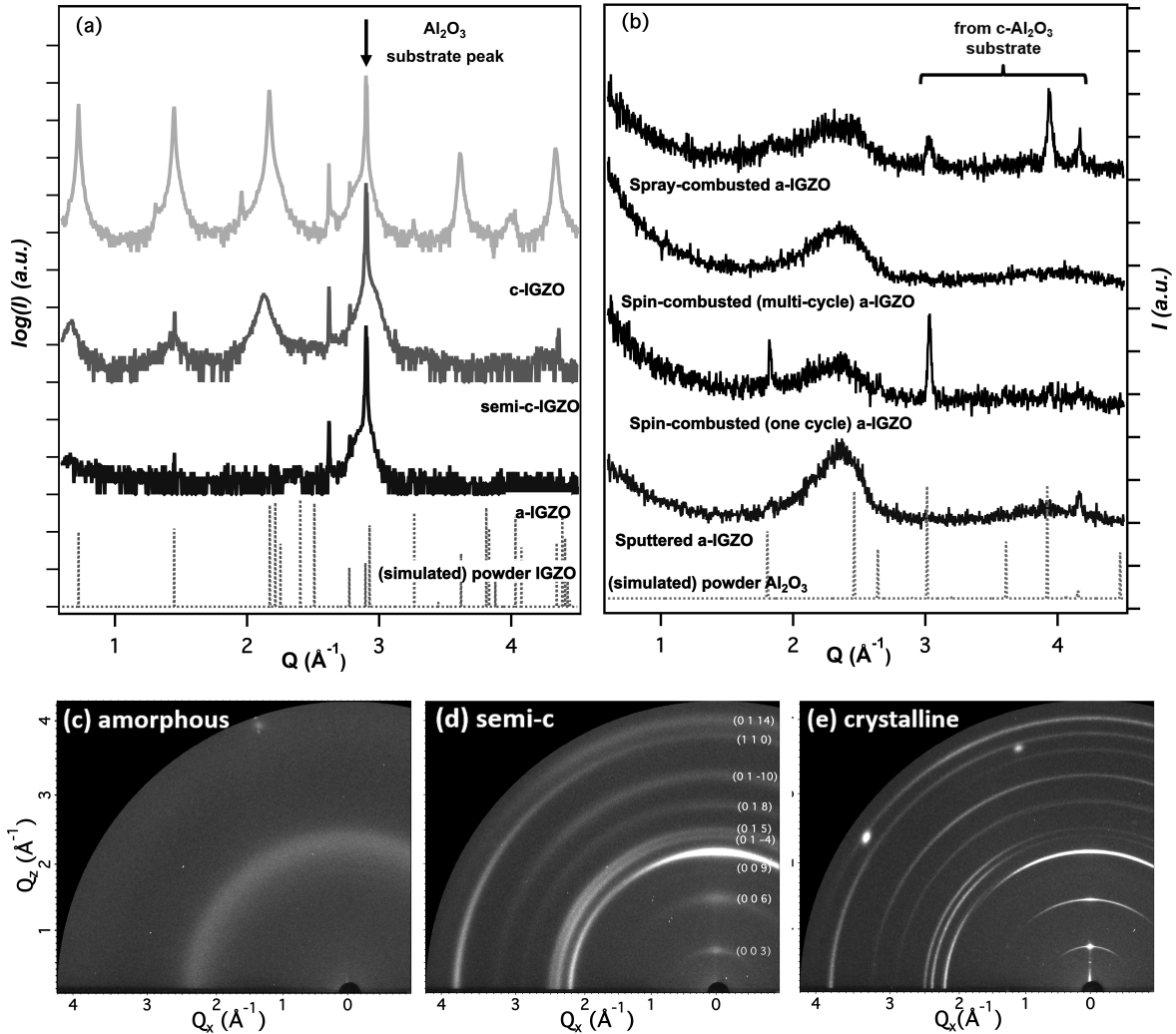


Figure 3.2. (a) XRD patterns of PLD-grown a-, semi-c-, and c-IGZO films. (b) GIWAXS study for sputtered and solution-processed a-IGZO. (c-e) Two-dimensional GIWAXS patterns of PLD-grown a-, semi-c- and c-IGZO films respectively, corresponding to those shown in (a).

the (009) diffraction peaks from the XRD data, and the grain size was determined to be $D = 6.9$ nm for the semi-c film and $D = 37.7$ nm for the c-IGZO film by applying the Scherrer equation[73]. This indicates that after annealing at 900 °C for 9 hours, c-IGZO has much a larger coherence length along the c-axis. Note that the measured grain size

D above is still much smaller than the thickness of the PLD films $t = 200$ nm, therefore in the limit of $D \ll t$ vibrons are more likely to be scattered by grain boundaries rather than film-substrate interface, so we anticipate that interface effects will be negligible.

For samples grown by other methods (sputtering and combustion), the GIWAXS data (Cu $K\alpha$ $\lambda = 1.54$ Å) shown in Figure 3.2(b) indicate broad amorphous diffraction peaks ($Q = 2.36$ Å⁻¹) which confirm that the as-deposited films are amorphous. The difference between Figure 3.2(a) and (b) is: XRD patterns in (a) were taken under Bragg-Brentano geometry, while GIWAXS in (b) under grazing incident geometry. In GIWAXS setup by fixing incidence angle near the critical angle of IGZO thin film, the X-ray penetration depth is much shallower than the XRD result in (a), which explains why no intense (006) peak from the substrate near $Q = 2.90$ Å⁻¹ was seen in (b). A few crystalline diffraction peaks, for example peaks shown in $Q = 3 - 4.2$ Å⁻¹ for spray-combustion IGZO film, were observed in Figure 3.2(b). These peaks match well with the simulated Al₂O₃ powder diffraction peaks shown as the grey trace at bottom of Figure 1(b). Therefore, they most likely came from substrates when X-ray was projected on the edge of small sapphire substrate.

The X-ray reflectivity technique was used to extract the film electron density and convert it to mass density based on the known stoichiometry (In: Ga: Zn: O = 1:1:1:4). The roughness root mean square is $RMS \approx 1$ nm for samples grown by PLD, and $RMS = 0.6$ nm for sputtered ones. All the solution-based combustion films have $RMS < 0.7$ nm[59]. We interpret the fraction of the reduced density as the porosity P , evaluated

Table 3.1. X-ray reflectivity results on the density and porosity of films fabricated by physical deposition (i.e. PLD[74] and sputter) and chemical synthesis[59] (i.e. spray and spin combustion), in order from low to high porosity.

Growth Method	ρ_f (g/cm ³)	P (%)
PLD	6.12	4.4
Sputter	5.86	8.4
Spray	5.85	8.6
Multi-cycle Spin	5.09	20.5
Single-cycle Spin	3.82	40.0

by comparing the film density ρ_f with the bulk density ρ_b :

$$(3.4) \quad P = 1 - \frac{\rho_f}{\rho_b}.$$

The reference single crystal bulk density $\rho_b = 6.40$ g/cm³ was calculated from the Inorganic Crystal Structure Database (#247980).

The density and porosity values of all the films are summarized in Table 3.1. The three PLD films with different morphologies are assumed to share the same high density and low porosity. On the other hand, the films grown by combustion show large variations in porosity, where the multi-cycle spin-combustion film is almost five times as porous as the spray-combustion film, which itself has a density close to that of the physically deposited films. (Table 3.1). Given the hot substrate throughout the spray-combustion process, one can expect spray-combustion films to trap very little of the gaseous combustion products (e.g. N₂, CO₂ and H₂O) in the material, yielding dense films similar to those fabricated by physical deposition[59]. With spin-combustion, on the other hand, the substrate is cold upon deposition, and combustion takes place in a subsequent step. The single-cycle film is observed to have about half the porosity of multi-cycle film (Table 3.1). This is

reasonable given that, unlike the multi-cycle film which had an annealing process after each spin cycle, the single-cycle film has only one chance to release the gaseous products during the final annealing and consequently is prone to having a higher porosity, double that of the multi-cycle film.

3.4.2. Thermal Conductivity Results

The temperature-dependent thermal conductivity of IGZO thin films is characterized from 18 K to 300 K using the 3ω technique on all the IGZO films. An example of 3ω dataset is shown in Figure 3.3 with a picture of the measurement device as inset where a processed film is put right next to a processed substrate. By comparing the signal difference between the filament on film and bare substrate, the cross-plane thermal conductivity for each film at each temperature can be deduced. The results on all the different IGZO samples are summarized in Figure 3.4, where the different shades of the symbols in panel (a) represent different morphologies and the different symbol themselves refer to different growth methods across the panels (a), (b) and (c). In Figure 3.4, all the physically deposited films [PLD-grown films in panel (a) and sputtered films in panel (b)] follow an empirical power law with temperature $\kappa \sim T^{0.6}$ from 18 K to room temperature, as shown by the dashed guiding lines. For the three combustion processed a-IGZO samples in Figure 3.4(c), the dense spray-combustion film exhibits the same temperature dependence $\kappa \sim T^{0.6}$ as the physically deposited IGZO films in Figure 3.4(a), while the two porous spin-combustion a-IGZO films show deviations with reduced thermal conductivities at both the low-end and high-end temperatures relative to this power law. It should be

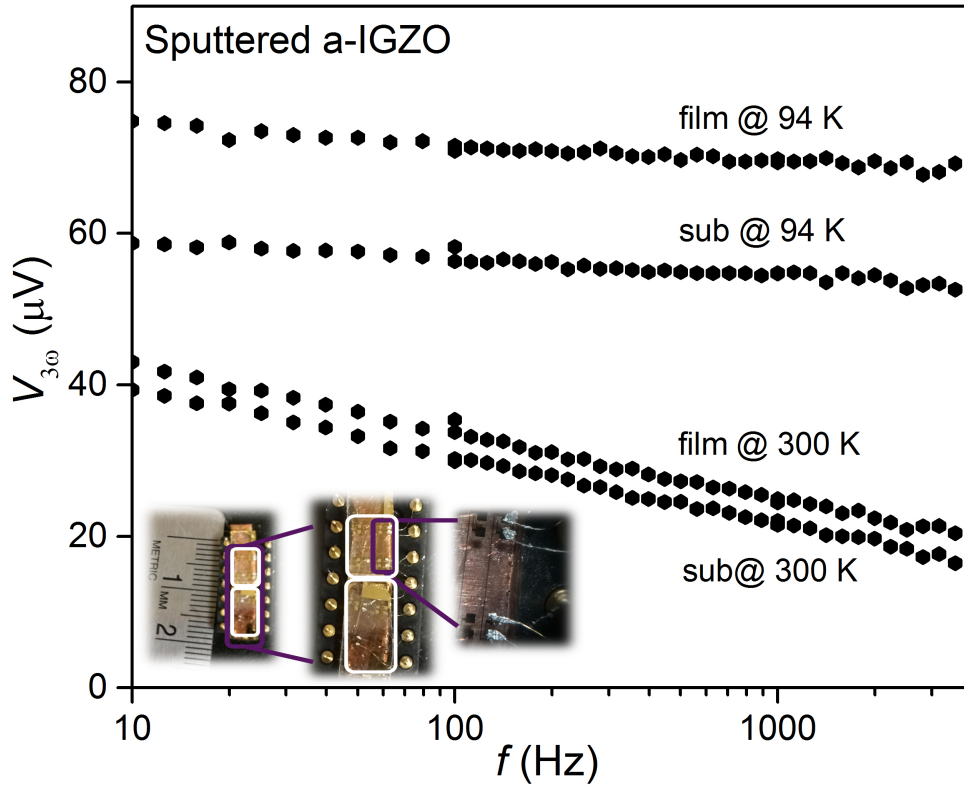


Figure 3.3. 3ω raw data of the sputtered a-IGZO film at $T = 300$ K and 94 K, with the measurement device picture as inset.

noted that these latter two porous samples differ by a constant factor throughout the whole temperature range.

3.5. Discussion

3.5.1. High-density PLD Films: Role of Crystallinity

It is remarkable that all the three phases of PLD samples (a-, semi-c- and c-IGZO) show the same power-law temperature dependence $\kappa \sim T^{0.6}$ in Figure 3.4(a). Increasing temperatures should excite a broader spectrum of vibrons with different mean-free-path length scales. Although there is no obvious underlying cause for the similar temperature

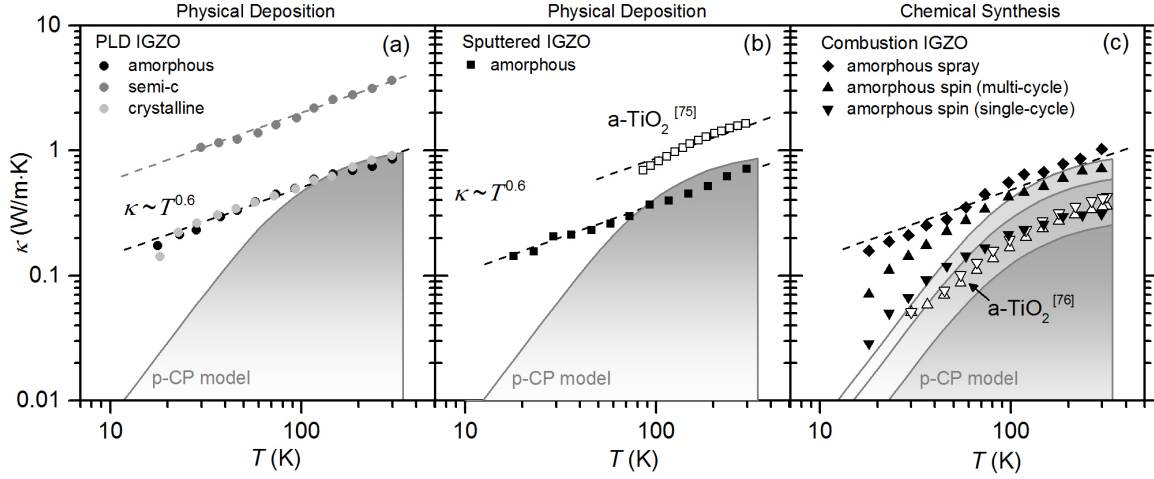


Figure 3.4. Temperature dependence of the thermal conductivity of all IGZO films under study, including (a) PLD films in different phases, (b) sputtered a-IGZO, and (c) combustion-processed a-IGZO. Comparison with another amorphous oxide[75, 76] a-TiO₂ is shown as open symbols, and the dashed lines are a guide to the eyes showing the empirical power law of the temperature dependence $\kappa \sim T^{0.6}$ which holds over this temperature range. The grey areas are “forbidden” — below the theoretical minimum thermal conductivities based on the p-CP model (Eq. 3.3) where the porosity factor is adopted from the percolation theory (Eq. 3.6). In (c), the three p-CP curves correspond to the porosity of spray, multi-cycle, and single-cycle spin-combustion films respectively from the top to the bottom.

dependence of all three phases, their common power-law behavior suggests that all three phases have similar energy density of states and that they only differ by a common scaling factor for the mean-free path at all energies.

For PLD-grown IGZO films in Figure 3.4(a), the a-IGZO almost perfectly overlaps the c-IGZO, both of which have a much lower thermal conductivity than that of semi-c-IGZO thin film. When the room-temperature behavior is plotted as a function of substrate temperature during deposition in Figure 3.5(a), a striking non-monotonic behavior emerges in the dependence of the thermal conductivity on crystalline order. A similar result was

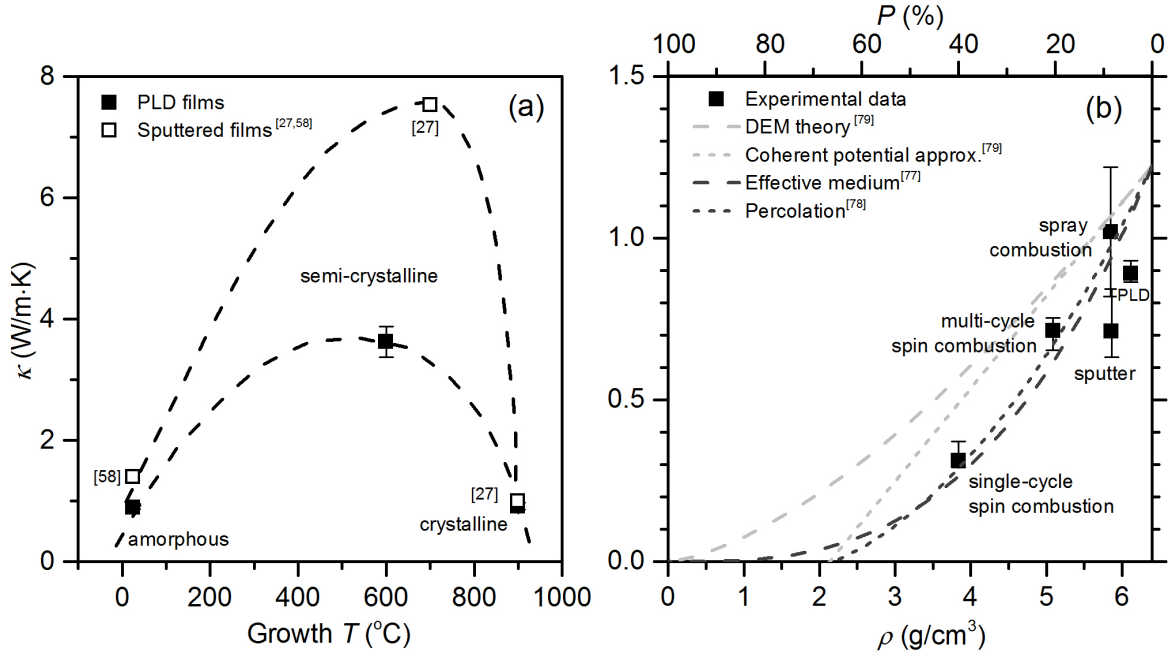


Figure 3.5. (a) Room-temperature thermal conductivity of a-, semi-c and c-IGZO resulting from different substrate growth temperatures. The films from this work are PLD grown, and those of Refs. 27, 58 are sputtered. The dashed lines in (a) are merely guides to the eye. (b) Room-temperature thermal conductivity of a-IGZO films as a function of density (bottom x) or porosity (top x) caused by different growth methods. Best fits to the experimental data are shown with black dashed and dotted lines by an effective medium model by Gesele[77] *et al.* and a percolation model by Kirkpatrick[78], respectively. For completeness, the lines in grey show two other models used for porous silica[79], which do not appear to fit our data. The representative error bars in both panels come from: 1) the variation of $\Delta T_{2\omega, f}$ across the film in the frequency sweep ($< 10\%$), and 2) the variation of measured thermal conductivity with heating power ($< 15\%$ for all samples [Footnote 1 on Page 40]). The temperature signal in 2ω across the IGZO layer is estimated to be about 10–15% of the total temperature drop through the sample ($\text{SiN}_x/\text{IGZO}/\text{sapphire}$ substrate)

seen previously in room temperature experiments of sputtered IGZO films[27, 58], also plotted in Figure 3.5(a) for comparison.

The intermediate-order semi-c IGZO exhibited the highest thermal conductivity [Figure 3.4(a), Figure 3.5(a)]. Crystalline and amorphous IGZO, on the other hand, show a relatively low and equal thermal conductivity. This counter-intuitive result could be explained by employing the structure of different phases of IGZO simulated by molecular dynamics simulations in Figure 3.1. The amorphous result is the easiest to explain, consistent with the strong scattering of vibration modes that one would expect from the minimal short-range order in an amorphous structure [80] [Figure 3.1(a)]. Crystalline c -axis aligned IGZO, however, is the most ordered film, yet its thermal conductivity is just as low as the amorphous film. This may be a result of the experiment measuring only out-of-plane c -axis thermal conductivity, and its superlattice-like structure with alternate stacking of In-O layers and Ga/Zn-O blocks [81] in Figure 3.1(c), creating regularly varying acoustic impedances. This is analogous to the thermal transport in superlattices[82, 83] and materials with planar defects perpendicular to c -axis[84], where the stacking interfaces effectively act like scatterers and significantly suppress the cross-plane c -axis thermal conductivity.

Finally, the other unexpected behavior is the significant *enhancement* of thermal conductivity for the semi-crystalline phase. One would naively think that semi-crystalline behavior would be an average of crystalline and amorphous, but a qualitatively different behavior is seen in the peak semi-c-IGZO conductance in Figure 3.5(a). This work reproduces a similar result in Refs.27, 58 on sputtered IGZO films, also shown in Figure 3.5(a). One explanation might be that individual grains have a large $a - b$ plane conductivity[85, 86] which for half the grains is randomly oriented out-of-plane as illustrated in Figure 3.5(b). Another explanation may be that grain boundary scattering

dominates the reduced thermal conductivity of the crystalline state, and the medium range order of the semi-crystalline state blurs the grain boundaries and allows crystalline regions to be continuously connected through an amorphous network.

3.5.2. Low-density Spin-combustion Films: Role of Porosity

Returning to Figure 3.4(c), the thermal conductivity of the combustion processed films is examined to understand the role of porosity. To check the validity of these results, they can be compared to similarly processed films in the literature. Spin-combustion a-IGZO data are comparable to a-TiO₂ prepared by a sol-gel process[76] with porosity $P = 30\%$, since both are solution-processed and porous. The consistently low thermal conductivity appears correlated with their similarly high porosity. Note that the poor thermal conductivity of the porous a-IGZO films might seem attractive for thermoelectric applications, but in practice such materials would not serve this purpose, because the electrical conductivity would also decrease significantly given the large porosity.

The thermal conductivities of the two spin-combustion films follow the same convex downwards temperature dependence in Figure 3.4(c), and exhibit lower thermal conductivity compared with physically deposited dense films in Figure 3.4(a)(b). These two low-density films only differ by a constant factor throughout the entire temperature range in Figure 3.4(c), and the proportionality factor can be explained by their different porosities.

Gesele *et al.*[77] reported an effective medium model for porous Si and the following correlation between porosity and thermal conductivity:

$$(3.5) \quad f(P) = (1 - P)^3,$$

where κ_0 is the thermal conductivity of a dense bulk. In the limit of phonon mean free path l much smaller than pore size a , the phonon hydrodynamics model[87] takes pore size into consideration to arrive at this expression. Due to the amorphous nature of the thin film, the phonon mean free path of a-IGZO film can be quite short of order several atomic bonds, for example[58] $l = 0.35$ nm, which is much smaller than the typical pore size[59] $a = 2 - 3$ nm determined by positron annihilation spectroscopy for solution-processed porous films.

Alternatively to the effective medium model, percolation theory[88] can be adopted to explain the thermal conduction dependence on porosity, by regarding the porous a-IGZO film as a network of thermally conducting channels and insulating voids. Kirkpatrick[78] proposed the following reduction factor for conductivity in the percolation picture, in the low-porosity limit:²

$$(3.6) \quad f(P) = [(1 - P) - 1.52P(1 - P)].$$

Both the effective medium and percolation models fit the room-temperature experimental results equally well, as is shown in Figure 3.5(b). For the model calculation, $\kappa_0 = 1.23$ W/(m · K) is assumed, which is the averaged dense-film thermal conductivity calibrated by single-cycle spin and PLD a-IGZO films using Eq. 3.5. Unlike the effective

²This expression was shown to be valid for porosities up to 40%. [78]

medium model, the percolation model has a threshold porosity $P_c = 65.8\%$ above which κ becomes vanishingly small since beyond this point the material only consists of isolated interpenetrating a-IGZO clusters with no covalently connected path for heat conduction.

There are other theories modeling the thermal conductivity in heterogeneous materials, for example the differential effective medium (DEM) theory and coherent potential approximation[89] [Figure 3.5(b)]. Compared with these theoretical predictions in grey, the a-IGZO system exhibits a more dramatically decreased thermal conductivity with increasing porosity. Although previous experimental results of thermal conductivity of porous silica matched these models well[79], these other models are not able to capture the sharper decrease of thermal conductivity with porosity observed in our combustion processed films.

3.5.3. Comparison with p-CP model

There have been many theoretical modelings of amorphous thermal conductivity. In the absence of a lattice, some theories describe generic thermal modes of vibration around equilibrium lattice positions in terms of vibrons, including propagating modes (propagons) and non-propagating modes (fractons)[60]. Although linear temperature dependence $\kappa \sim T$ is commonly observed[90, 91] and explained with resonant scattering[92] or phonon-assisted fracton hopping[93], a large amount of work shows deviations[94, 51, 95] from this linear behavior, including the present study. Jagannathan *et al.*[96] proposed that the strong anharmonic coupling of phonon and fracton can quench the fracton hopping rate and lead to slower rise of κ with increasing T . Then several lattice-dynamics-based numerical calculation were conducted[97, 98] including the contribution from non-propagating

vibrational states. More recently a Green-Kubo mode analysis[99] was developed taking anharmonic atomic interactions into consideration.

Given this diversity of theories, we therefore chose to compare the data to a porosity-adjusted Cahill-Pohl model discussed in Section 3.3.2 due to the simplicity and universality of this theory. The p-CP curves for different a-IGZO are plotted as an upper boundary of the grey areas in Figure 3.4(a), (b), and (c). Note that in the low T limit, the integral in Eq. 3.1 yields a constant, leading to the temperature dependence $\kappa \sim T^2$, seen as an asymptotic power-law slope on the left of the log-log plot. On the other hand, in the high T limit, κ approaches a constant, as seen on the right of the p-CP curves. The porosity factor $f(P)$ in the p-CP model (Eq. 3.3) is adopted from the percolation theory (Eq. 3.6) due to its better fit with our experimental data [Figure 3.5(b)]. For calculating $\kappa_{\min}^{\text{CP}}(T)$, $E = 130$ Gpa is taken from a past report[58] on IGZO. Poisson's ratio ν does not vary much among thin films: For example, $\nu = 0.33 - 0.42$ for a-Si:H films[100], $0.25 - 0.4$ for a-C:H films[100], and $\nu = 0.3$ for a-SiN_x films[101], 0.27 for poly-c SiN_x films[102]. So in the absence of direct Poisson's ratio for IGZO, we use that of another transparent conducting oxide ITO thin film[103] $\nu = 0.35$.

Figure 3.4(a) and (b) show consistency with the p-CP model in that the measured thermal conductivities remain at or above the model value. Below 30 K, the data exceed the κ_{\min} value by half an order of magnitude. Whereas the CP model assumes that the lifetime of all vibrational modes is half an oscillation period, the observed difference at low T between the measured data and the CP model shows that the longer-wavelength modes must be significantly longer-lived than half an oscillation period.

For combustion processed films, the p-CP model fits the increasingly porous films remarkably well [Figure 3.4(c)], correctly predicting the low- and high-temperature deviations below the empirical $\kappa \sim T^{0.6}$ fit, including the general downwards curvature in the temperature dependence. In this regard, it appears that porous films serve as exemplary Cahill-Pohl minimal thermal conductors, provided that the correct porosity factor $f(P)$ is identified for scaling the CP model. The percolation model[78] for $f(P)$ gives the best fit curves shown here.

3.5.4. Long-term Room Temperature Instability

After the temperature dependence study described above, thermal conductivity instability was also observed within about 2 years of storage. The cross-plane thermal conductivity measurement of PLD IGZO thin films are repeated at room temperature on three occasions within 19 months, between which the samples have been kept in a desiccant with 1/6 atmosphere pressure. Following the first measurement (i.e. $t = 0$ month in Figure 3.6), the samples were kept in a desiccant jar pumped down to 1/6 atmosphere pressure, and taken out for repeating the 3ω measurements in air at room temperature after several months (i.e. $t = 9$ and 19 months) and then returned to the same storage environment.

Figure 3.6 summarizes the thermal conductivity κ of the three PLD films as a function of storage time. The initial values of κ for post-annealed films at $t = 0$ are the same as those in Figure 3.4(a) at 300 K. Examining the time dependence, the thermal conductivities of semi-c-IGZO and c-IGZO thin films decreased, while that of a-IGZO does not change significantly, as shown in Figure 3.6. Compared with c-IGZO where the thermal

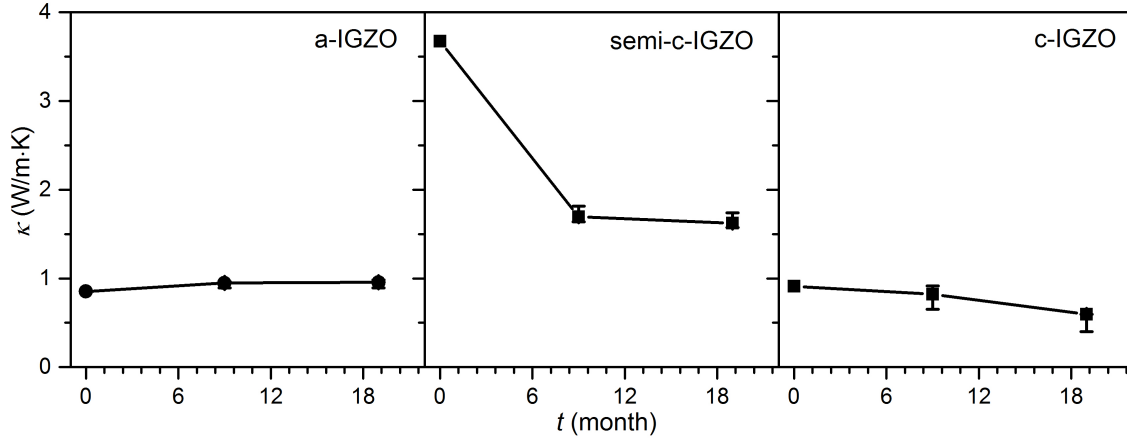


Figure 3.6. Room-temperature thermal conductivity as a function of over one and a half years of storage time.

conductivity reduced only slightly with each measurement, the change in semi-c-IGZO film is more significant: its thermal conductivity dropped to half of the original result after 9 months of storage, and proceeded to drop slightly further after 19 months of storage. Two possible reasons for the decreasing thermal conductivity are discussed below.

Structural changes can be one possible reason for reducing the thermal conductivity with longer storage time. In order to investigate the possible structure change in semi-c-IGZO, XRD was conducted again on the semi-c-IGZO thin film after the 19-month storage Figure 3.7. It shows that the film still maintains the diffraction signatures of semi-crystalline phase, but there are minor shifts of the first three peaks ($\Delta_{2\theta} < 1^\circ$), and most apparently near $2\theta = 30^\circ$. This may indicate some structural relaxation in crystal orientation caused by residual strain in the film. The amorphous film, on the other hand, cannot reorient with time under residual strain since there is no order, and the c-axis aligned crystalline films are already aligned in their lowest energy orientation.

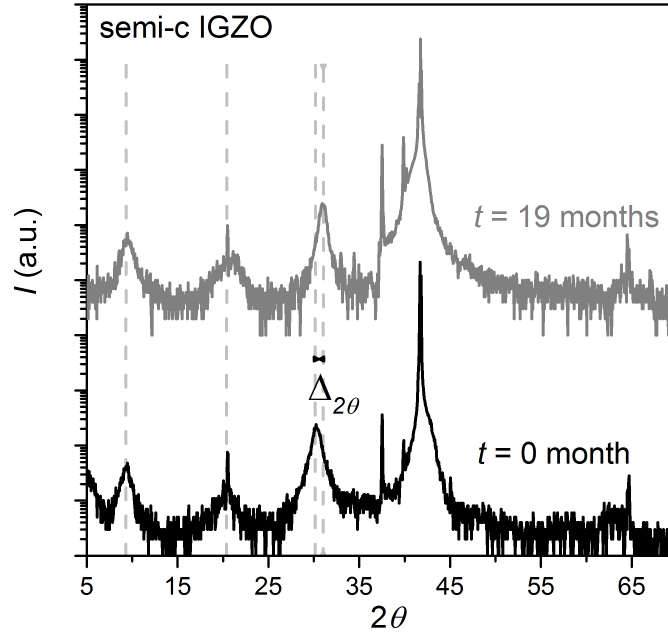


Figure 3.7. XRD pattern of semi-c IGZO film shows peak shifts after 19-month storage, most apparently around $2\theta = 30^\circ$.

A remaining possible explanation for the reduced thermal conductivity is the diffusion of oxygen vacancy defects. One widely accepted mechanism for electrical conduction in TCOs is that oxygen vacancies act as donors contributing to free-carrier concentration [19, 104]. Since the films under study were capped with SiN_x insulation layer to facilitate the 3ω measurement, new vacancies are not likely to be generated given that the film is effectively sealed. But pre-existing vacancies may still play a role if they are able to diffuse to regions of the sample where they may impede thermal conductivity. It is known both experimentally and computationally that vacancies interrupt heat transport by scattering vibrational modes and consequently reducing the thermal conductivity [105, 106, 107, 108, 109]. If in the present system oxygen vacancies were to diffuse from the bulk of the grains to the grain boundaries, the vacancies at the grain boundaries may disrupt thermal

conductivity from grain-to-grain. Since the grain size in semi-c-IGZO is only about 1/6 of that in c-IGZO as shown in Section 3.4.1, the smaller grain size results in a greater volume percentage of grain boundaries in semi-c-IGZO than c-IGZO film. This may explain why the reduction in thermal conductivity is more drastic in semi-crystalline film. Given the fact that there exist no grain boundaries in amorphous systems, vacancies cannot diffuse to these low-energy boundaries to further suppress heat transport. This is consistent with the observation that a-IGZO thin film maintains almost the same in thermal conductivity over the full 19-month storage. Meanwhile, the grain size in c-IGZO is much larger than that in semi-crystalline phase, leading to a significant reduction in volume fraction of grain boundaries in c-IGZO. This may explain why the thermal conductivity decrease in c-IGZO is not as dramatic as that in semi-c-IGZO.

A remark is warranted on the role of dryness for the long-term storage. Given that the sample is effectively sealed from the environment by the silicon nitride cap layer, these samples likely would have exhibited the same behavior in any room temperature ambient. However, one can speculate that if the cap layer were instead air-permeable allowing IGZO exposure to ambient moisture and oxygen present, the oxygen vacancy diffusion at grain boundaries may be significantly affected by the different ambient condition. Although the volume fraction of grain boundaries would not change, the pre-existing vacancies could be filled with hydrogen and oxygen from the ambient [110] and increasing the thermal conductivity, or at least making the reduction of thermal conductivity less drastic. And the time scale of the change of such an exposed film may be different, since the moist air acts as an activated oxidizing environment.

3.6. Future Work

To further test the conjecture of phonon interface scattering in c-IGZO along c -axis, in the future it would be helpful to measure in-plane vs. cross-plane thermal conductivity in c-IGZO. If the conjecture is valid, the in-plane thermal conductivity would be considerably larger than the cross-plane value already measured here. This requires patterning narrow filaments as illustrated in Section 5.1.

Additionally, the correlation between electron and phonon transport is worth a systematic study. In transparent conducting oxides such as InO[61] and ZITO[111], a highest Hall mobility was observed at the onset of crystallinity, where the structural characteristics were claimed to be responsible (e.g. bond distance, bond angle and connected chains). In our study of thermal conductivity, or to some extent phonon mobility, the intermediate semi- c phase similarly manifests the maximum in Figure 3.5. Similar to our observation, one report after our publication demonstrated a high thermal conductivity of semi- c -IGZO similar to our result, but another semi- c -IGZO phase with larger grain size having a dramatically reduced κ which is even lower than c-IGZO.[112] So the structural change from amorphous to crystalline phase may affect the phonon transport in transparent conducting oxides. Linking the phonon and electron transport properties together may help the community better understand the structure and finally tune the property at will for various applications.

Finally as another potential future application, thermally insulating films could be fabricated in large area using one-cycle spin-combustion process to compete with aerogel. Aerogel is a synthetic material with extremely high porosity and low thermal conductivity

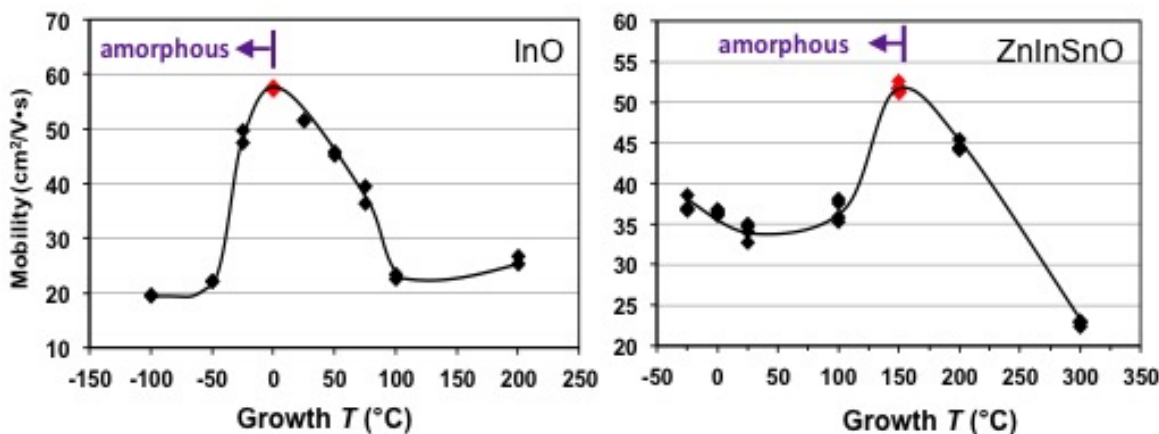


Figure 3.8. Hall mobility of transparent conducting oxides InO[61] and ZITO[111], both of which demonstrate a maximum mobility at the transition from amorphous to crystalline phase.

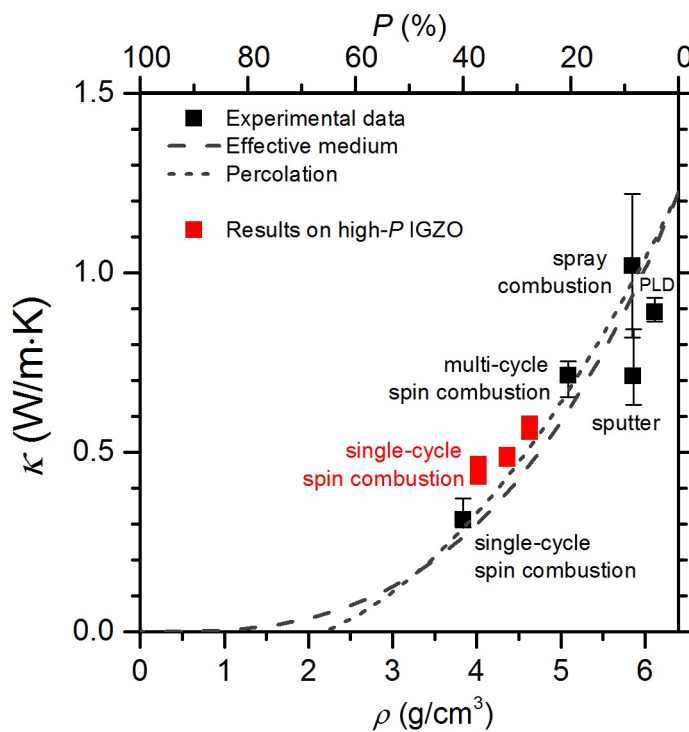


Figure 3.9. Latest results on high-porosity IGZO thin films (red) grown by one-cycle spin-combustion process, compared with original results.

($\kappa \approx 0.02 \text{ W}/(\text{m} \cdot \text{K})$)[113] comparable with air, and has been used for thermal insulation in architectural purposes, vehicle and space launch applications[114, 115]. Inspired by the porosity-dependent thermal conductivity in our study [Figure 3.5(b)] where the percolation model shows a threshold porosity $P_c = 65.8 \%$, it may be promising to fabricate high-porosity oxides around or even above this porosity to explore the possibility of ultra-low thermal conductivity. Further efforts have been made on the thermal conductivity of high-porosity IGZO with the results shown in Figure 3.9, which is consistent with the model prediction and previous measurement results in black. For the growth side, it requires more progress in growing higher porosity $P > 40 \%$ by using one-cycle spin-combustion. Then the buried 3ω method proposed in Section 2.6 can be adopted to measure the thermal conductivity of these highly porous films.

CHAPTER 4

Candidate $p \times n$ -Type Transverse Thermoelectrics

This chapter focuses on a type of energy-conversion materials: $p \times n$ -type transverse thermoelectrics, specifically five candidate compounds and band structure calculations on two representative candidates. Though the overall thesis focuses on thin film materials, this chapter will examine the general paradigm of transverse thermoelectrics, and the subsequent chapter will address the thin-film variety of $p \times n$ -type transverse thermoelectrics. The criteria for identifying $p \times n$ TTE is derived in Section 4.1. Section 4.2 identifies five different ambipolar compounds as $p \times n$ candidates, and evaluates their thermoelectrical performance by calculating the transverse $z_{\perp}T$ and characteristic angles. Among these compounds, two promising bulk crystalline candidates are picked to study their band structure by using density functional theory calculation in Section 4.3, in order to develop a better understanding of the underlying causes of $p \times n$ -type behavior.

4.1. Criteria for identifying $p \times n$ -Type Candidates from Calculated Seebeck Tensors

The Materials Genome paradigm employs high-throughput computation tool to accelerate the discovery and design of new materials[116]. Although the Seebeck tensor can be directly calculated in such Materials Genome searches, the criteria to distinguish $p \times n$ TTE from this Seebeck tensor has been missing. This section develops the necessary

criteria to identify $p \times n$ TTE's, thereby facilitating the discovery of new $p \times n$ TTE under the Materials Genome project.

There are two possibilities for identifying whether the Seebeck tensor of a material represents a $p \times n$ TTE. If the principle axes of the Seebeck tensor used in the calculation are aligned with the crystalline axes, then it is straightforward to identify the $p \times n$ character, however, off-diagonal components of the Seebeck tensor can also occur in some low symmetry materials whose principle axes are *not* aligned with the crystal axes of the calculation. So here we propose the two equivalent criteria for identifying a $p \times n$ TTE, below:

Criteria I: A material with a diagonalized Seebeck tensor is a $p \times n$ -type TTE if the Seebeck coefficient along one principle axis has the opposite sign as the other two Seebeck coefficients along the remaining principle axes.

Criteria II: A material with general Seebeck tensor is a $p \times n$ -type TTE if the tensor has non-zero determinant but can be rotated to have a zero on at least one diagonal.

Since Criteria I is straightforward and represents the original criteria put forth in the discovery of $p \times n$ -type TTE — namely that the Seebeck coefficient is p -type along one axis and n -type along an orthogonal axis, the rest of this section focuses on the alternate criterion II to derive the conditions for identifying a transverse thermoelectric even when the Seebeck tensor includes off-diagonal terms. This latter formulation will be more helpful in rapidly sorting candidate materials in a Materials Genome search, since it can handle non-diagonalized Seebeck matrices. In the Seebeck effect, a thermoelectric field \mathbf{E} is generated from a temperature gradient ∇T , where the Seebeck tensor is defined in the

relation $\mathbf{E} = -\mathbf{S}\nabla T$. If the S_{ii} diagonal component of \mathbf{S} is zero, then the thermoelectric field \mathbf{E} will be orthogonal to a temperature gradient ∇T applied in the i -direction, resulting in Criteria II.

To convert Criteria II to a mathematical statement, we must first identify the linear algebra operation equivalent to rotating a given Seebeck tensor to an arbitrary basis until one of the diagonal terms is zero. The rotation matrix to transform a three-dimensional tensor can be parameterized with three angles, ϕ , θ , and α , according to the Roe Convention:

$$(4.1) \quad \mathbf{R} = \begin{bmatrix} \cos \phi & -\sin \phi & 0 \\ \sin \phi & \cos \phi & 0 \\ 0 & 0 & 1 \end{bmatrix} \begin{bmatrix} \cos \theta & 0 & \sin \theta \\ 0 & 1 & 0 \\ -\sin \theta & 0 & \cos \theta \end{bmatrix} \begin{bmatrix} \cos \alpha & -\sin \alpha & 0 \\ \sin \alpha & \cos \alpha & 0 \\ 0 & 0 & 1 \end{bmatrix}$$

$$= \begin{bmatrix} \cos \phi \cos \theta \cos \alpha - \sin \phi \sin \alpha & -\cos \phi \cos \theta \sin \alpha - \sin \phi \cos \alpha & \cos \phi \sin \theta \\ \sin \phi \cos \theta \cos \alpha + \cos \phi \sin \alpha & -\sin \phi \cos \theta \sin \alpha + \cos \phi \cos \alpha & \sin \phi \sin \theta \\ -\sin \theta \cos \alpha & \sin \theta \sin \alpha & \cos \theta \end{bmatrix},$$

which is able to rotate any tensor from the original x, y, z unprimed basis, to any x', y', z' prime basis.

For an arbitrary 3D Seebeck tensor with non-zero off-diagonal terms

$$\mathbf{S} = \begin{bmatrix} S_{xx} & S_{xy} & S_{xz} \\ S_{yx} & S_{yy} & S_{yz} \\ S_{zx} & S_{zy} & S_{zz} \end{bmatrix},$$

after a transformation to the primed basis $S' = \mathbf{R} \mathbf{S} \mathbf{R}^T$ and division by $\cos^2 \theta$, the last diagonal term on the bottom right of the matrix would become

$$\begin{aligned} \mathbf{S}'_{zz} = [\mathbf{R} \mathbf{S} \mathbf{R}^T]_{zz} &= S_{xx} \cos^2 \phi \tan^2 \theta + S_{yy} \sin^2 \phi \tan^2 \theta + S_{zz} \\ &+ 2S_{xy} \cos \phi \sin \phi \tan^2 \theta + 2S_{xz} \cos \phi \tan \theta + 2S_{yz} \sin \phi \tan \theta. \end{aligned}$$

If this component is zero, then it is possible for the thermoelectric field $\mathbf{E} = -\mathbf{S}\nabla T$ to be made orthogonal to a temperature gradient ∇T applied along the z axis, satisfying Criteria II. Setting this transformed S'_{zz} term to zero leads to a quadratic equation for $\tan \theta$

$$(S_{xx} \cos^2 \phi + 2S_{xy} \cos \phi \sin \phi + S_{yy} \sin^2 \phi) \tan^2 \theta + (2S_{xz} \cos \phi + 2S_{yz} \sin \phi) \tan \theta + S_{zz} = 0.$$

For a quadratic expression $Ax^2 + Bx + C = 0$, a real solution only exists when the term $B^2 - 4AC$ is non-negative, or equivalently,

$$(S_{xz} \cos \phi + S_{yz} \sin \phi)^2 - S_{zz}(S_{xx} \cos^2 \phi + 2S_{xy} \cos \phi \sin \phi + S_{yy} \sin^2 \phi) > 0.$$

Regrouping terms and dividing by $\sin \phi$ gives another quadratic expression,

$$(S_{yz}^2 - S_{yy}S_{zz}) \tan^2 \phi + 2(S_{xz}S_{yz} - S_{xy}S_{zz}) \tan \phi + (S_{xz}^2 - S_{xx}S_{zz}) > 0.$$

which is a parabola $y = Ax^2 + Bx + C > 0$ with $x = \tan \phi$. This parabola will only have non-negative values when:

(a) it is an upward parabola meaning that $A > 0$, such that in the limit of large $|\tan \phi|$

the first term dominates, namely

$$S_{yy}S_{zz} - S_{yz}^2 < 0. \text{ or}$$

(b) it intersects the y axis ($\phi = 0$) at a positive value meaning $C > 0$, such that in the limit of small $\tan \phi$ the third term dominates, namely

$$S_{xx}S_{zz} - S_{xz}^2 < 0, \text{ or}$$

(c) if it is a downward parabola with a negative intersection with y axis, the maximum of this parabola is positive, namely plugging into the inequality the solution $x = -B/2A$ describing the maximum value of the downwards parabola, or equivalently $\tan \phi = -(S_{xz}S_{yz} - S_{xy}S_{zz})/(S_{yz}^2 - S_{yy}S_{zz})$, then

$$(S_{xz}^2 - S_{xx}S_{zz})(S_{yz}^2 - S_{yy}S_{zz}) - (S_{xz}S_{yz} - S_{xy}S_{zz})^2 < 0$$

$$S_{zz}(S_{xx}S_{yy}S_{zz} + 2S_{xz}S_{yz}S_{xy} - S_{zz}S_{yz}^2 - S_{yy}S_{xz}^2) < 0$$

$$S_{zz} \det \|\mathbf{S}\| < 0.$$

In linear algebra, the minor of a matrix M_{ij} is the determinant of the matrix after the i th row and j th column have been removed. By this definition, we can rewrite the conditions (a) and (b) above, where the left sides of (a) and (b) would become M_{xx} and M_{yy} .

Empirically the first two conditions are redundant, as can be independently verified from the definition of positive and negative definite matrices[117]. So it can be shown that only one of (a)+(c) or (b)+(c) is sufficient to correctly identify all TTE's. In the language of linear algebra, it is equivalent to saying that the Seebeck tensor \mathbf{S} is indefinite.

This means the tensor is *neither* positive definite (all eigenvalues positive), *nor* negative definite (all eigenvalues negative), *nor* semi-definite (contains zero eigenvalues)[117].

4.2. Candidate Materials in Ambipolar Bulk Compounds

4.2.1. Candidate Materials

This section focuses on ambipolar bulk compounds that manifest the anisotropic ambipolar conduction, namely dominated by p -type and n -type conduction in two orthogonal crystal axes, respectively. Some artificial materials like superlattices[30, 118] can also be tailored to be transverse thermoelectrics, as will be discussed in the subsequent chapter. By going through the literature of ambipolar materials with thermoelectric characterization and evaluating their TTE characteristics as below, we were able to identify the following 5 materials as $p \times n$ -type TTE candidates. Because a determination of the TTE characteristics requires the Seebeck coefficient, electrical resistivity, and thermal conductivity in both the p -type and n -type orthogonal directions, it is rare that the published literature contains enough information to definitively identify $p \times n$ -type TTE's. But with reasonable assumptions, such as assuming temperature-independent thermal conductivities, or using theoretical Seebeck tensors when the experimental Seebeck is missing, one can arrive at a fair estimate of the performance of candidate TTE materials.

The five candidate compounds from our literature search are identified below. When plotting these data, we will use solid symbols for data that is experimentally measured, and open symbols for data that represents published theoretical values, or that is estimated with assumptions.

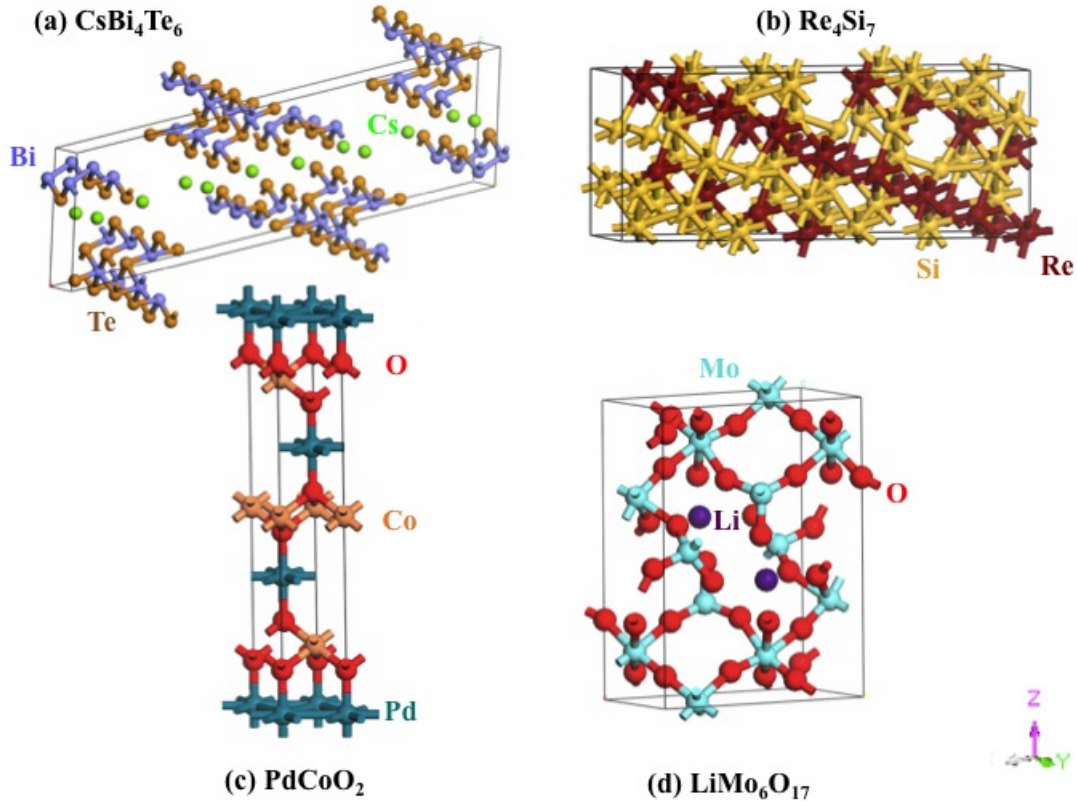


Figure 4.1. Crystal structure of (a) CsBi_4Te_6 , (b) $\text{ReSi}_{1.75}$, (c) PdCoO_2 and (d) $\text{LiMo}_6\text{O}_{17}$.

(1) CsBi_4Te_6 , which crystallizes in the monoclinic space group $C2/m$, has a layered structure composed of $[\text{Bi}_4\text{Te}_6]^-$ alternative layers with intercalated Cs^+ ions [Figure 4.1(a)]. Due to its significant anisotropy in the carrier effective mass, the anisotropic thermoelectric properties were examined[119] using steady-state technique in three crystal orientations: a -axis which is parallel to the $[\text{Bi}_4\text{Te}_6]^-$ layers, b axis or needle direction along which needle-shaped samples are usually formed, and c -axis which is perpendicular to Cs atom layer. With all this information, the transverse figure of merit is calculated for as-prepared samples from $T = 1.5$ K to 300 K, shown in Figure 4.1(a).

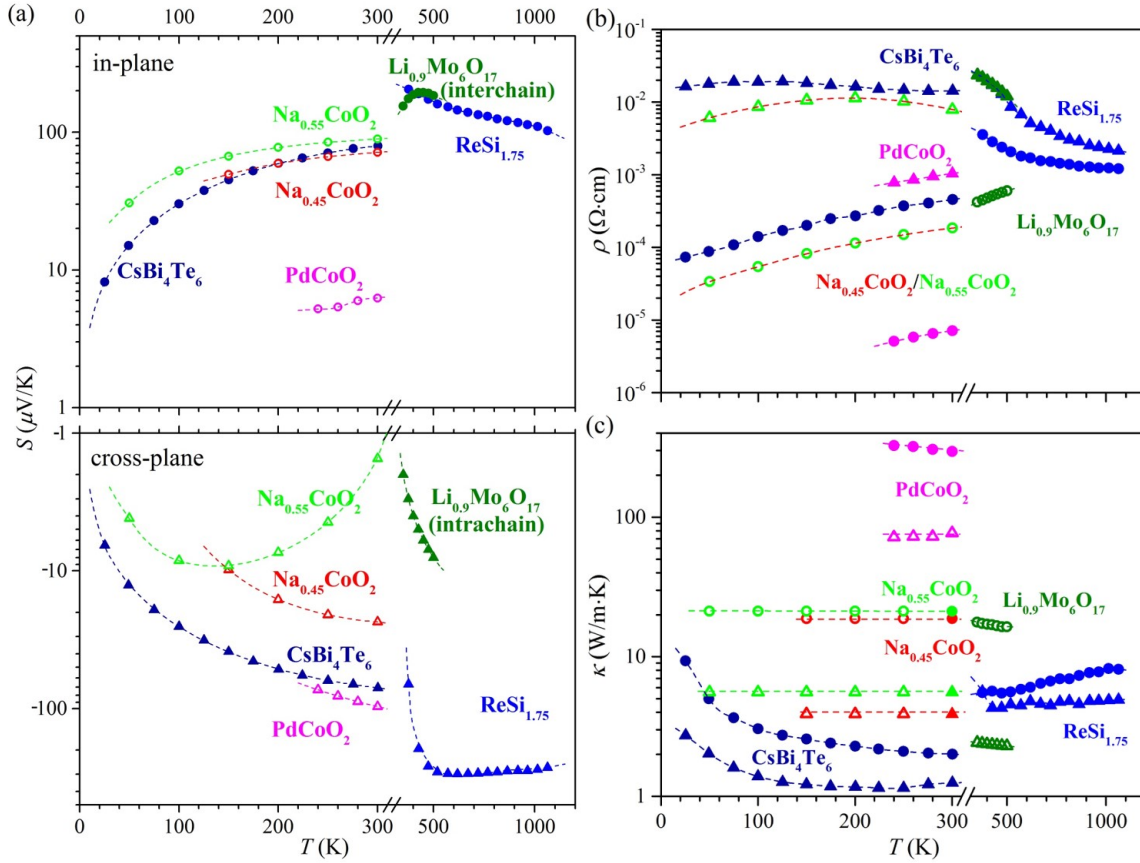


Figure 4.2. Thermoelectric characteristics of the five compounds CsBi_4Te_6 , $\text{ReSi}_{1.75}$, PdCoO_2 , Na_xCoO_2 and $\text{Li}_{0.9}\text{Mo}_6\text{O}_{17}$: (a) Seebeck coefficient (top panel for positive, bottom panel for negative), (b) electrical resistivity, and (c) thermal conductivity. The circles and triangles represent the values for in-plane (interchain for $\text{Li}_{0.9}\text{Mo}_6\text{O}_{17}$) and out-of-plane (intrachain for $\text{Li}_{0.9}\text{Mo}_6\text{O}_{17}$), respectively. Solid symbols are experimental data from previous studies, while hollow ones represent those calculated theoretically or assumed constant within the temperature range.

(2) $\text{ReSi}_{1.75}$, which is another monoclinic crystal with Si vacancies [Figure 4.1(b)], is also a promising candidate for superior thermoelectric performance, since it shows p -type conduction in a axis [100] and n -type conduction in c axis [001]. Both its electrical resistivity and Seebeck coefficient demonstrate anisotropy [120, 121, 122] in four-point

measurements. The thermal conductivity data is lacking, so back-calculated from zT and resistivity values for a and c axes respectively[123].

(3) There are some cobalt oxides exhibiting outstanding ambipolar characteristics, which can be utilized as $p \times n$ -type thermoelectrics. PdCoO_2 is a hexagonal delafossite oxide with alternative triangular lattice layers as shown in Figure 4.1(c), exhibiting metallic transport properties in-plane and meanwhile acting as poorer metal in the out-of-plane direction. The exceptionally low resistivity of PdCoO_2 helps to generate a relatively high transverse thermoelectric figure of merit. In order to calculate the figure of merit, we use the Seebeck coefficient calculated by Boltzman theory[124], resistivity measured with four-probe method[125], and thermal conductivity determined by steady-state technique and a finite element model[126].

(4) Besides PdCoO_2 , Na_xCoO_2 shows ambipolar properties in Seebeck coefficient with $x = 0.45$ and 0.55 , which was obtained theoretically by the Boltzmann transport method[127]. But to our knowledge the resistivity and thermal conductivity for these two materials have not been characterized in the literature. Meanwhile, NaCo_2O_4 ($x = 0.5$ for Na_xCoO_2) has been extensively studied because of its potential to be an outstanding thermoelectric material. So for this work, we assume that $\text{Na}_{0.45}\text{CoO}_2$ and $\text{Na}_{0.55}\text{CoO}_2$ have similar resistivity[128] as NaCo_2O_4 . The thermal conductivities of different stoichiometries were calculated within the GreenKubo theory, and were assumed to be temperature-independent[129].

(5) It was recently found that a quasi-one-dimensional metal $\text{Li}_{0.9}\text{Mo}_6\text{O}_{17}$, a low-temperature conductor known as “lithium purple bronze”, possesses a highly anisotropic

thermopower. Its monoclinic unit cell is shown in Figure 4.1(d). Above room temperature, it shows a p -type interchain Seebeck coefficient perpendicular to the chains (c -axis) with an n -type metallic intrachain conduction along the chains (b -axis) because the weak electron-interchain transport at high temperatures is dominated by the thermally activated carriers from the valence band[130]. Given the measured Seebeck coefficient and inter-chain resistivity above room temperature, the lack of thermal conductivity and intra-chain resistivity data were extrapolated to higher temperatures from previous studies[131, 132].

4.2.2. Thermoelectric Performance Analysis

In addition to $z_{\perp}T$, there are three critical angles that differentiate the performance of these ambipolar compounds as TTEs since the heat flow and electric field are in different directions in $p \times n$ -type TTEs. These geometric “figures of merit” have no analog in standard longitudinal thermoelectric materials. First, we will define the angle θ_{zT} as the angle between the principle crystal axes and the electrical current \mathbf{J} that results in the maximum figure of merit. Second, we will define the angle between the current \mathbf{J} and thermal flow \mathbf{Q} in TTE at maximum figure of merit as θ_{JQ} . Finally, the current \mathbf{J} and thermal flow \mathbf{Q} can be perfectly orthogonal as per the definition of a transverse thermoelectric. The angle where this occurs is not necessarily the same as the angle that gives maximum $z_{\perp}T$, so we define the angle θ_{\perp} as the angle between the principle crystal axes and the electrical current \mathbf{J} such that the thermal flow is orthogonal to this current, $\theta_{JQ} = 90^{\circ}$. The remainder of this section will calculate and discuss these three angles θ_{zT} , θ_{JQ} , and θ_{\perp} as well as the transverse figure of merit $z_{\perp}T$.

As an example, we will consider a $p \times n$ -type transverse thermoelectric with p -type conduction dominating the a -axis, and n -type conduction along the c -axis.[30] When the angle θ_{zT} between the principle axes (a , c axes for example) and the current \mathbf{J} satisfies

$$(4.2) \quad \cos \theta_{zT} = \frac{1}{1 + \sqrt{\frac{\kappa_{cc}/\kappa_{aa}}{\rho_{cc}/\rho_{aa}}}},$$

the transverse figure of merit is maximized to be

$$(4.3) \quad z_{\perp}T = \frac{(S_{p,aa} - S_{n,cc})^2 T}{(\sqrt{\rho_{aa}\kappa_{aa}} + \sqrt{\rho_{cc}\kappa_{cc}})^2},$$

where $S_{p,aa}$ and $S_{n,cc}$ are p -type and n -type Seebeck coefficient for the principle material axes of anisotropy a (in-plane axis) and c (cross-plane axis) respectively at temperature T , ρ is electrical resistivity and κ is thermal conductivity. Note that compared with the conventional longitudinal figure of merit, the transverse $z_{\perp}T$ is enhanced by having a large a positive Seebeck coefficient for the p -type conduction direction and a large negative one for the n -type direction according to this equation.

With all the parameters including Seebeck coefficient, electrical resistivity and thermal conductivity obtained from previous literature in Figure 4.2, the transverse figure of merit $z_{\perp}T$ [Figure 4.3(a)] with the optimized angle θ_{zT} between current and principle axis [Figure 4.3(b)] can be calculated by using Equation 4.3. $z_{\perp}T$ is plotted in the temperature range from $T = 20 - 1100$ K with a break in the T -axis between room temperature and 400 K accompanied by a change in scale. The values of $z_{\perp}T$ of the various materials shown here span from 10^{-5} to 1 within this temperature range, most of which are below $z_{\perp}T = 0.1$ making them not as competitive as conventional thermoelectric materials

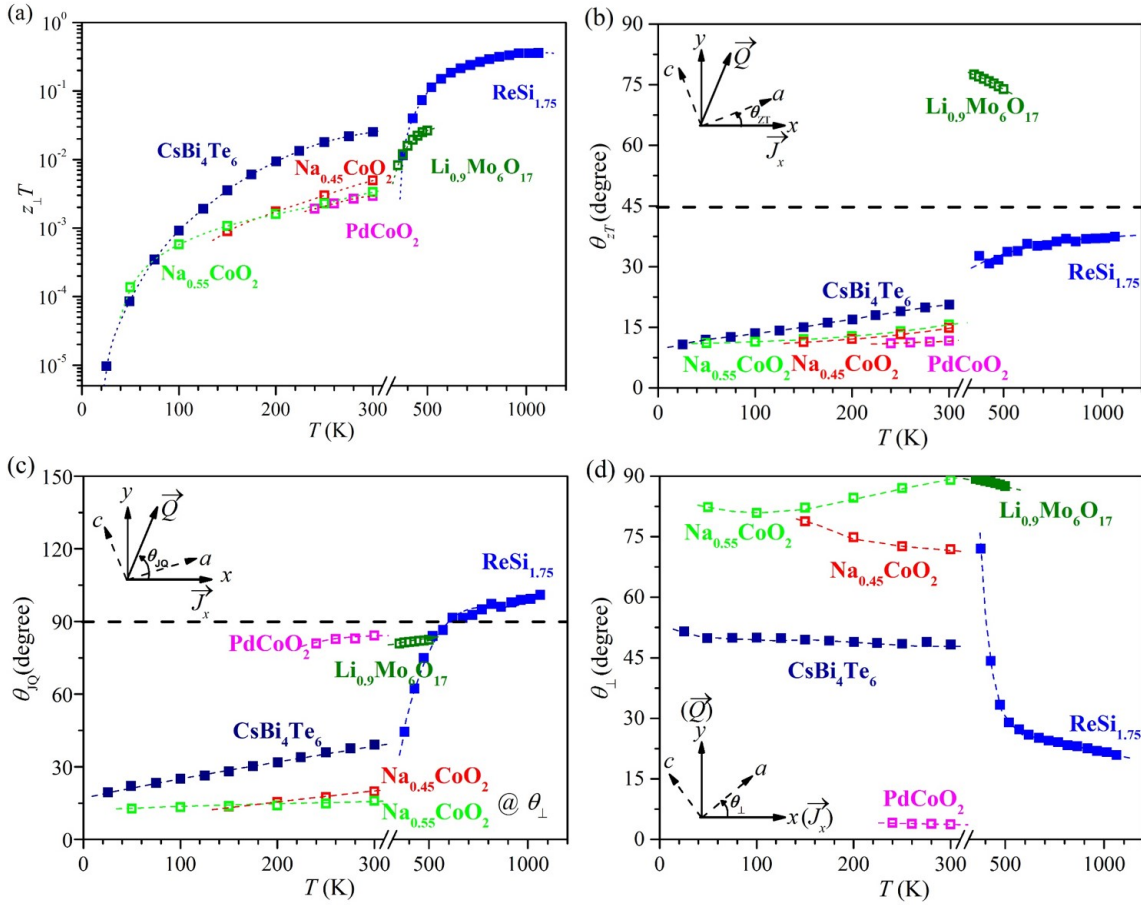


Figure 4.3. (a) Optimized transverse figure of merit $z_{\perp}T$ at (b) the optimized angle θ_{zT} between the current and principle axis shown in the inset, both as a function of temperature. (c) The current-heat angle θ_{JQ} between the current \mathbf{J} and induced heat \mathbf{Q} . (d) The angle between the current and principle axis θ_{\perp} that leads to perpendicular heat and current flow.

at this stage of materials research. However, given that these characterizations were made before the $p \times n$ TTE paradigm was even known, no attempt at optimizing TTE materials performance has been attempted yet, and there should be room for significant improvement with minimal effort using the now standard lexicon of methods developed for improving standard thermoelectrics.

Among all the ambipolar compounds, $\text{ReSi}_{1.75}$ stands out as the most competitive compound with the $z_{\perp}T$ orders of magnitude higher than the others, albeit at the highest temperature range. As its anisotropy becomes more and more significant with increasing temperature above $T = 600$ K, eventually the optimal $z_{\perp}T = 0.36$ is achieved around $T \approx 1060$ K due to the large difference of Seebeck coefficient between two principle axes. Note again, that improved thermoelectric characteristics are expected for this and other materials in the future with standard thermoelectric engineering optimization tricks such as doping. The band structure of $\text{ReSi}_{1.75}$ will be calculated in Section 4.3 to obtain fundamental insight of its ambipolar behavior. According to Equation 4.2, the angle θ_{zT} corresponding to optimal $z_{\perp}T$ should be 45° under isotropic of thermal conductivity and electrical resistivity, *i.e.* $\kappa_{cc}/\kappa_{aa} = \rho_{cc}/\rho_{aa}$. Thus a dashed line is plotted as a guide to the eyes at $\theta_{zT}=45^{\circ}$ in Figure 4.3(b), and $\text{ReSi}_{1.75}$ has a θ_{zT} closest to this angle for all the materials presented here..

The second important angle θ_{JQ} is the angle between current \mathbf{J} and induced heat flow \mathbf{Q} as shown in Figure 4.3(c). In the transport basis rotated by an angle θ whereby the current flows in the x -direction, the diagonal Seebeck tensor in the crystal basis is

transformed as follows

$$\begin{aligned}
(4.4) \quad \mathbf{S}_{2D} &= \begin{bmatrix} \cos \theta & -\sin \theta \\ \sin \theta & \cos \theta \end{bmatrix} \begin{bmatrix} S_{p,aa} & 0 \\ 0 & S_{n,cc} \end{bmatrix} \begin{bmatrix} \cos \theta & \sin \theta \\ -\sin \theta & \cos \theta \end{bmatrix} \\
&= \begin{bmatrix} S_{p,aa} \cos^2 \theta + S_{n,cc} \sin^2 \theta & (S_{p,aa} - S_{n,cc}) \sin \theta \cos \theta \\ (S_{p,aa} - S_{n,cc}) \sin \theta \cos \theta & S_{p,aa} \sin^2 \theta + S_{n,cc} \cos^2 \theta \end{bmatrix} \\
&= \begin{bmatrix} S_{xx} & S_{xy} \\ S_{yx} & S_{yy} \end{bmatrix},
\end{aligned}$$

leading to the off-diagonal term S_{xy} necessary for inducing transverse thermoelectric behavior. The total heat flux density \mathbf{Q} is proportional to the current density \mathbf{J}

$$(4.5) \quad \mathbf{Q} = \mathbf{\Pi} \cdot \mathbf{J} = (T\mathbf{S}) \cdot \mathbf{J},$$

where $\mathbf{\Pi}$ is the Peltier tensor equal to the product of Seebeck tensor \mathbf{S} and temperature T according to the second Thomson relation. Therefore, the longitudinal and transverse heat flow density are

$$\begin{aligned}
(4.6) \quad Q_x &= (S_{p,aa} \cos^2 \theta + S_{n,cc} \sin^2 \theta) T J_x, \\
Q_y &= (S_{p,aa} - S_{n,cc}) \sin \theta \cos \theta T J_x.
\end{aligned}$$

Since the x axis will be defined parallel to the current density vector \mathbf{J} , the angle between \mathbf{J} and its induced heat flow density \mathbf{Q} satisfies $\tan \theta_{JQ} = Q_y/Q_x$, which yields the current-heat angle

$$(4.7) \quad \theta_{JQ} = \arctan \frac{(S_{p,aa} - S_{n,cc}) \sin \theta \cos \theta}{S_{p,aa} \cos^2 \theta + S_{n,cc} \sin^2 \theta}.$$

as shown in Figure 4.3(c). With the dashed-line guide to the eye at 90° in Figure 4.3(c), it can be easily seen that PdCoO_2 , $\text{Li}_{0.9}\text{Mo}_6\text{O}_{17}$ and $\text{ReSi}_{1.75}$ have almost perpendicular heat flow \mathbf{Q} relative to the current \mathbf{J} when operating at the optimized performance angle θ_{zT} .

Finally we define the angle θ_\perp between the principle axes (a , c axes for example) and the current \mathbf{J} such that a perfectly perpendicular heat flow results relative to the applied current, *i.e.* $\theta_{JQ} = 90^\circ$. Equivalently, for a current J_x in the x -direction, there is no resulting x -component of heat flow Q_x , *i.e.*

$$(4.8) \quad (S_{p,aa} \cos^2 \theta + S_{n,cc} \sin^2 \theta) T J_x = 0.$$

Therefore,

$$(4.9) \quad \theta_\perp = \arctan \sqrt{-S_{p,aa}/S_{n,cc}}.$$

θ_\perp is shown in Figure 4.3(d) for candidate compounds. If the current direction x is rotated by θ_\perp relative to the crystal axis a , the effective heat flow would be all along the orthogonal direction.

4.3. Band Structure Calculation

To obtain an insightful understanding of the underlying causes of $p \times n$ -type TTE in areal material, we calculate the band structure and Seebeck tensor of two promising TTE compounds in collaboration with Prof. Jiong Yang's Group at the Materials Genome Institute in Shanghai University. Although the engineering approach of energy band

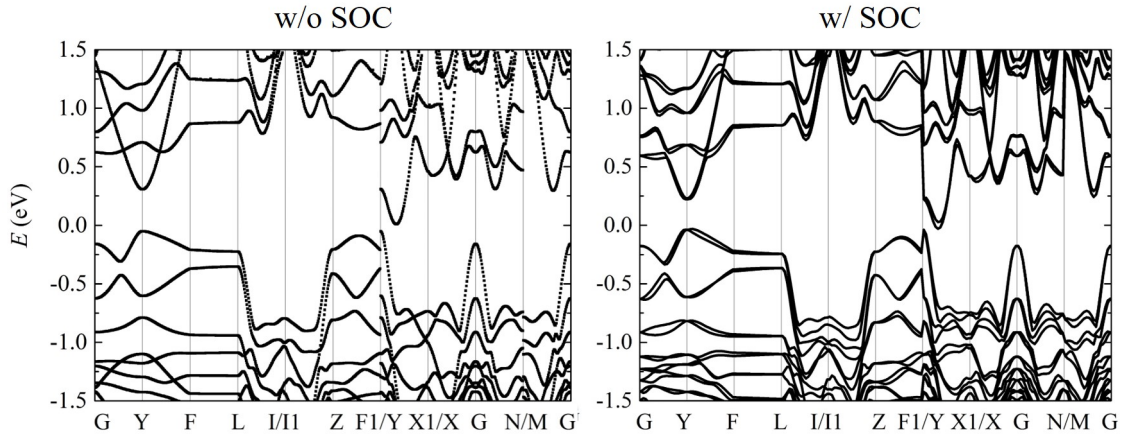


Figure 4.4. The band diagram of $\text{ReSi}_{1.75}$ without and with spin-orbit coupling in (a) and (b), respectively.

calculation is already well known for optimizing the performance of conventional thermoelectrics, for TTE the understanding of the structure-property-performance relationship behind ambipolar behavior in these compounds is still limited.

The first-principle calculations here use Vienna *ab initio* Simulation Package (VASP)[133, 64], and a recently developed strongly constrained and appropriately normed (SCAN) meta-generalized gradient approximation (meta-GGA)[134]. A plane-wave cut-off energy of 520 eV and an energy convergence criterion of 10^{-4} eV for self-consistency are adopted throughout the calculations. The transport property is determined by Boltzmann Transport Properties (BoltzTraP) program with the output from VASP[135, 136]. Fermi surfaces are plotted with Xcrysden[137]. Transport and Fermi surface calculations require very dense K -point samplings. Specifically, the K -point mesh is $42 \times 42 \times 56$ for $\text{ReSi}_{1.75}$, and $89 \times 89 \times 39$ for PdCoO_2 .

$\text{ReSi}_{1.75}$ is chosen as a promising compound for $p \times n$ -type TTE given its highest $z_{\perp}T$ among all candidates reviewed here and a θ_{JQ} closest to 90° , as illustrated in Section 4.2.2.

The standard DFT calculation usually disregards spin-orbit coupling (SOC), which however may break the energy band degeneracy (especially in heavy elements such as rhenium) and lead to changes in band structure. To verify our calculation, the band structures are calculated with and without spin-orbit coupling as shown in Figure 4.4. These two band structure are similar enough that we adopt the calculation without SOC for the purpose of simplicity and calculation efficiency. The electronic band structure of $\text{ReSi}_{1.75}$ is shown in Figure 4.5(a) with five different Fermi energy levels F1-F5 around the middle of the band gap. As the Fermi energy shifts from the valence band to conduction band (i.e. from F1 to F5), the transition of the Fermi surface in Figure 4.5(c) first shows a shrinking Fermi surface area from panel F1 as the Fermi energy approaches the middle of the gap in panel F3 indicating the minimum electrical conduction. Examining the shape of this Fermi surface, when the Fermi energy is near the top of the conduction band as F1 and F2 in Figure 4.5(c), the Fermi surface manifests a heavy effective mass along Γ -Z, and a light effective mass along Γ -X and Y.

One can use this qualitative information about the relative effective masses to make predictions about the directionality of the Seebeck tensor. Given the fact that the Seebeck tensor of two parallel bands is weighted by the electrical conductivity tensor, the Seebeck tensor component is expected to be small in S_{zz} , and large in S_{xx} and S_{yy} around F1 and F2. Similarly for F4 and F5 in Figure 4.5(c) when the chemical potential is near the bottom of the conduction band, the Fermi pocket shows a heavy effective mass along Γ -X, and a light effective mass along Γ -Y and Z. So near the F4 and F5 the Seebeck tensor components are expected to be small in S_{xx} , and large in S_{yy} and S_{zz} .

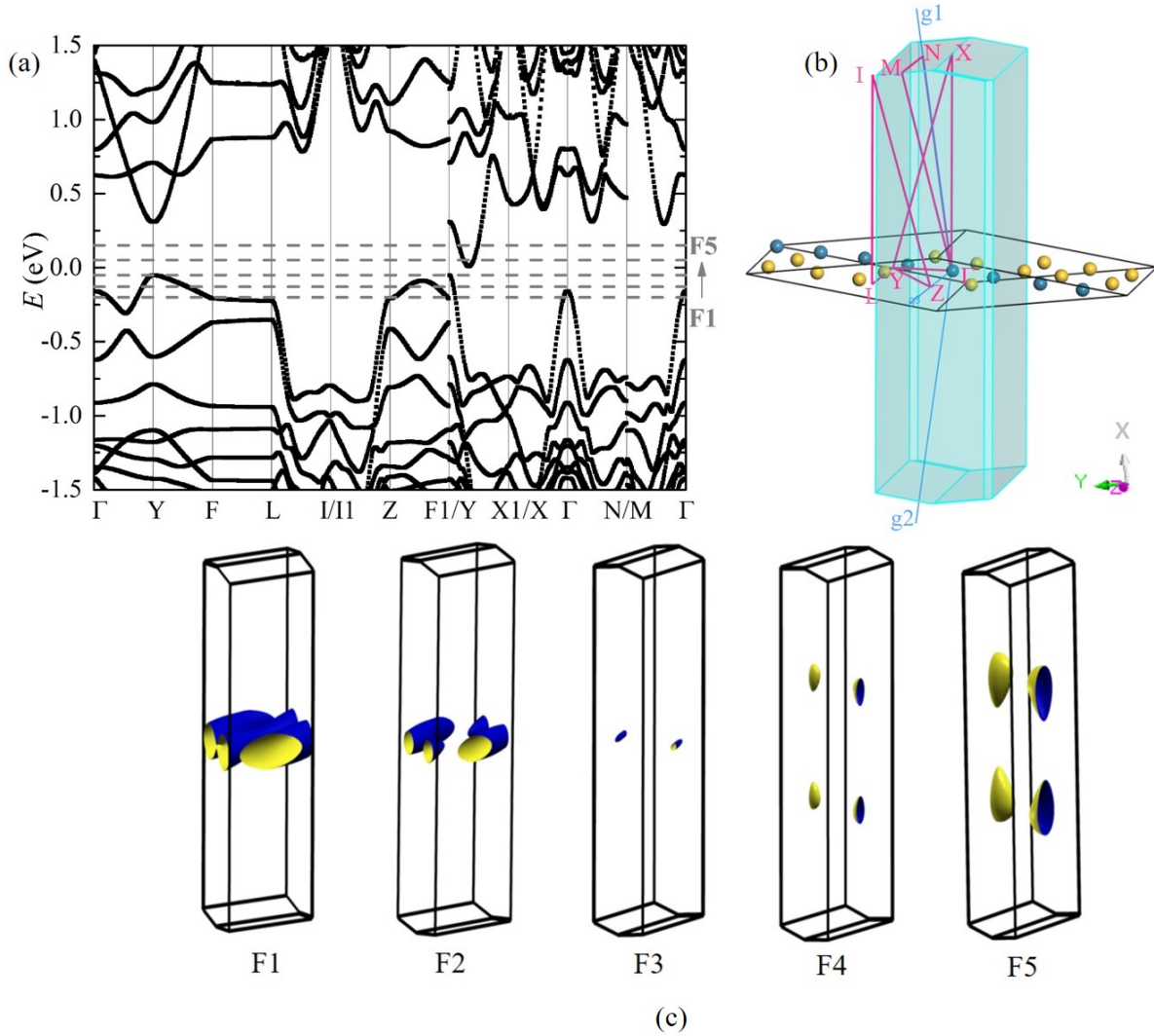


Figure 4.5. (a) Calculated band structure of $\text{ReSi}_{1.75}$, with labeled Fermi levels F1-F5. The Brillouin zone with the real-space lattice are plotted in (b), with labeled high-symmetry points in reciprocal space. (c) The Fermi surfaces at different fermi level as labeled in (a).

From the band structure of $\text{ReSi}_{1.75}$, the full Seebeck tensor was calculated which turned out to have non-zero off-diagonal terms S_{xz} and S_{zx} , requiring the analysis of Section 4.1 to confirm the transverse thermoelectric character. These two terms S_{xz} and S_{zx} , which by symmetry must be equal, were similar but not equal in the resulting calculation,

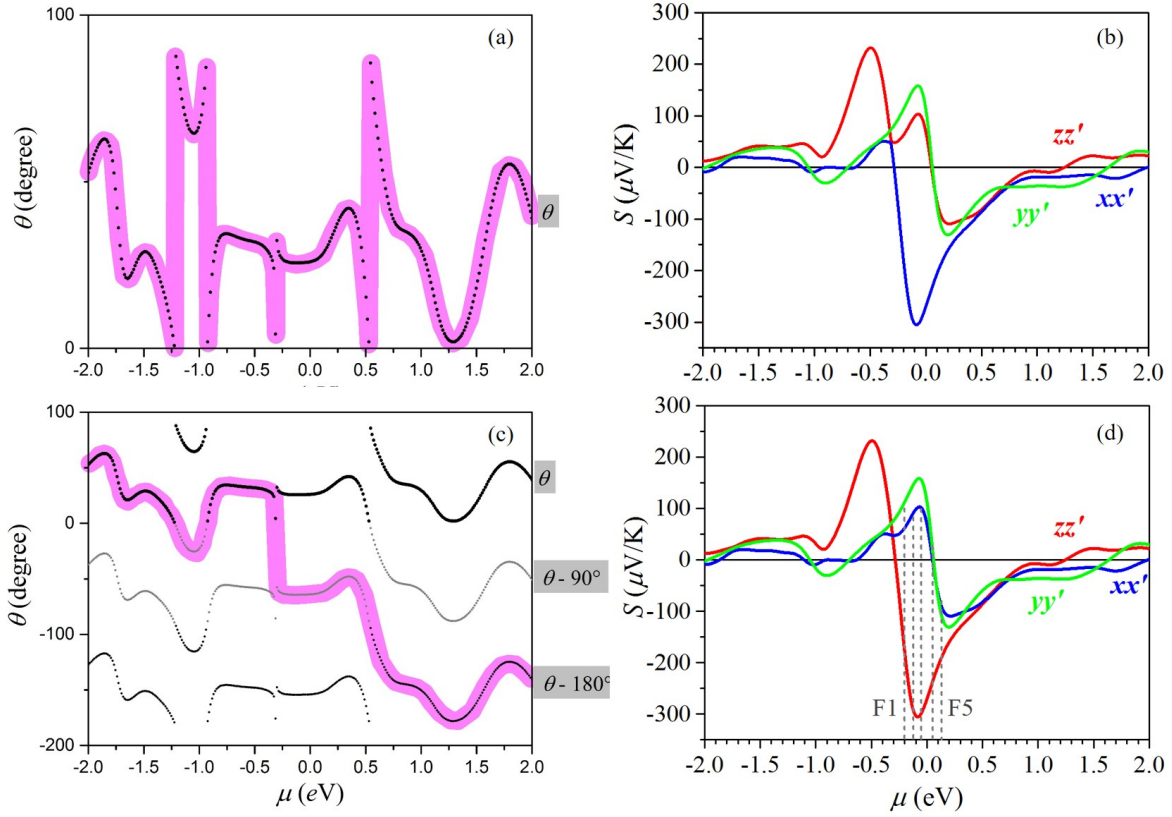


Figure 4.6. Correcting for 90-degree phase slips in the calculated Seebeck tensor. (a) As-calculated rotation angle θ_{xz} for Seebeck tensor diagonalization according to Equation 4.10, where the pink trace highlights the angle oscillation between 0 to 90°. (b) As-calculated Seebeck components according to Equation 4.11. (c) The three curves of θ_{xz} , $\theta_{xz} - 90^\circ$, and $\theta_{xz} + 90^\circ$, among which the pink background highlights a continuous trace of θ_{xz} with 90° phase slips. (d) Corrected Seebeck tensor components considering the value slips corresponding to θ_{xz} phase slips in (c), where the dashed lines are the same chemical potentials F1-F5 (from left to right) as those in Figure 4.5(a).

due to errors inherent in the difficult task of calculating transport characteristics from first principles. So for the purpose of estimating a value for $S_{xz} = S_{zx}$, the average of these two values is taken.

The non-zero off-diagonal terms warrant a more thorough discussion, as they have no analog in standard thermoelectrics. In low-symmetry crystals the principle axes of the diagonalized Seebeck tensor may vary with temperature and chemical potential, and they are not necessarily aligned with the principle axes of the crystalstructure, itself. The chemical-potential dependence of the S_{xz} , S_{xx} , and S_{zz} terms means that the principle axes of the Seebeck tensor may rotate by a chemical-potential-dependent angle θ_{xz} in the $x - z$ plane as the chemical potential changes, where

$$(4.10) \quad \theta_{xz} = \frac{1}{2} \arctan \frac{2S_{xz}}{S_{xx} - S_{zz}}.$$

Note, for example, that if the off-diagonal component S_{xz} is zero, then the angle θ_{xz} is likewise zero. With this rotation, the Seebeck elements in the diagonalized tensor become

$$(4.11) \quad \begin{aligned} S'_{xx} &= \frac{S_{xx} + S_{zz} \pm \sqrt{(S_{xx} - S_{zz})^2 + 4S_{xz}^2}}{2}, \\ S'_{yy} &= S_{yy}, \\ S'_{zz} &= \frac{S_{xx} + S_{zz} \mp \sqrt{(S_{xx} - S_{zz})^2 + 4S_{xz}^2}}{2}. \end{aligned}$$

To diagonalize the Seebeck tensor, Figure 4.6(a)(b) shows dependence of the *as-calculated* rotation angle θ_{xz} and Seebeck components on the chemical potential according to Equation 4.10 and 4.11, respectively, assuming the upper positive sign is taken for S'_{xx} and the upper negative sign is taken for S'_{zz} . The angle θ_{xz} jumps abruptly as observed in Figure 4.6(a), indicating 90-degree phase slips. Note that in Equation 4.11 the values S'_{xx} and S'_{zz} are interchangeable given different signs in the definition, so there is no way to

assign the definitive value for S'_{xx} and S'_{zz} . Therefore, the only way to determine consistency is to try to find a solution whereby the angle θ_{xz} changes slowly and continuously, and removes any false discontinuities since the equation is only correct modulo 90° . To identify phase slips in θ_{xz} , the curve is plotted together with θ_{xz} plus/minus multiples of 90° in Figure 4.6(c). A continuous trace highlighted in pink identifies 90° phase slips from the grey to the black curve and vice versa within certain chemical potential ranges. Correspondingly the Seebeck components are corrected as shown in Figure 4.6(d).

After correcting for the Seebeck phase slips in Figure 4.6(d) where the Fermi levels are labeled in F1-F5, the consistency between Seebeck calculations and the band diagram in Figure 4.5(a) is interpreted. Near F2 and F3 (*i.e.* the top of the valence band), S'_{zz} reached the minimum in negative while S'_{xx} and S'_{yy} are at their positive maximum values, where the largest difference between the *n*-type and *p*-type occur near these Fermi levels leading to the maximum thermopower for TTE. Consistent with our expectation described in the previous paragraph according to the effective mass, around the minimum of conduction band (*i.e.* F4 and F5), S'_{zz} is much larger than S'_{xx} although they both become negative as an *n*-type behavior.

The other representative material picked for band structure calculation is PdCoO₂ since the current-heat angle in this material is close to 90° as shown in Figure 4.3(c). The band diagram result in Figure 4.7(a) is plotted from the Γ point along the three crystal axes in reciprocal space, where for a charge neutral chemical potential at $\mu = 0$ there is a metallic band in the in-plane direction between Γ -X and between Γ -Y, and a semiconducting band in the cross-plane direction between Γ -Z. From the band structure result, the Seebeck components are deduced as shown in Figure 4.7(b) with a $89 \times 89 \times 39$

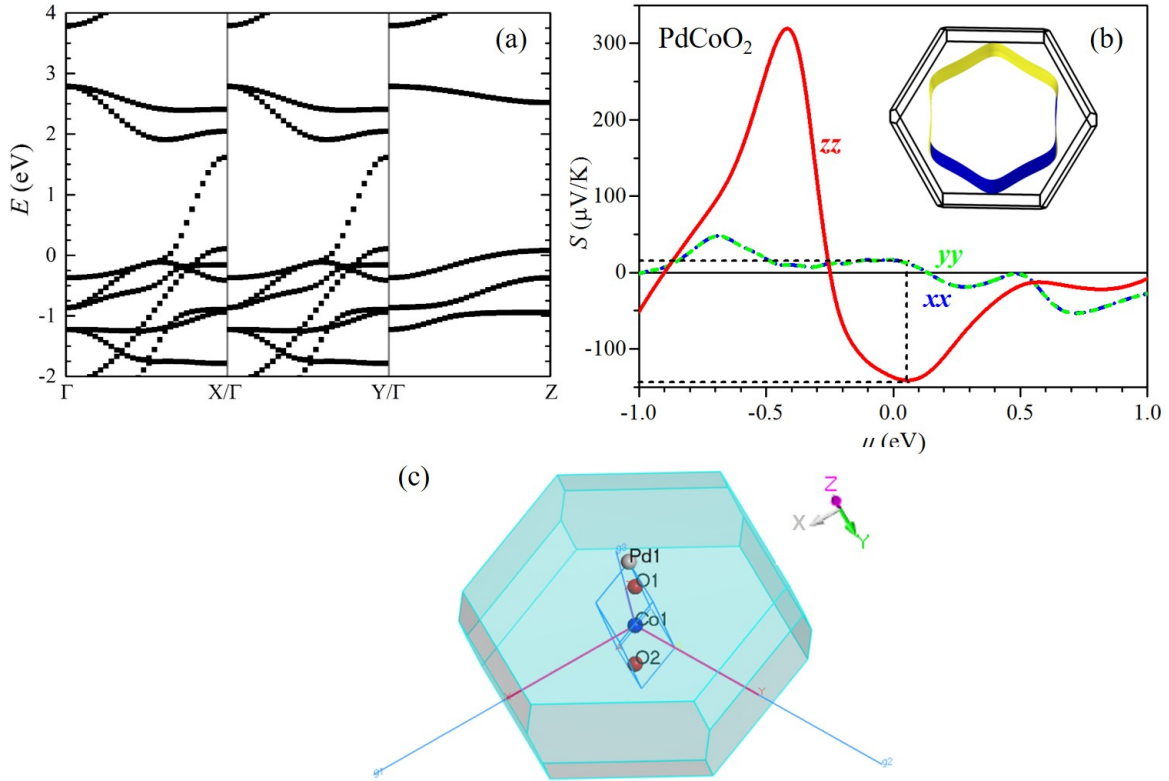


Figure 4.7. (a) Band structure of PdCoO₂ along X, Y, and Z axes. (b) Seebeck coefficient S of PdCoO₂ in three different crystal axes, where the black dashed line indicates a positive in-plane S and a negative cross-plane S with the largest difference in between. The upper right inset in (b) demonstrates the corresponding Fermi surface of PdCoO₂ at this chemical potential $\mu = 0.05$ eV. (c) The real-space atomic structure in the Brillouin zone where the reciprocal axes X, Y, and Z are labeled.

MonkhorstPack K -point sampling used for the primitive unit cell. The two axes in the in-plane direction have the same thermopower given the symmetry. The value of Seebeck coefficient is low in the in-plane direction as one would expect for a metal. The chemical potential $\mu = 0.05$ eV at the dashed line gives a global minimum in the negative cross-plane thermopower S_{zz} as well as a p -type thermopower in the in-plane direction, which corresponds to the Fermi surface drawn in Figure 4.7(b) upper right. Consistently, this

Fermi surface is a symmetric hexagon within the X-Y plane [Figure 4.7(c)] as expected from the isotropic band along Γ and X/Y axis.

4.4. Future Work

With the promising candidates identified in Section 4.2, future experimental work needs to be done to fabricate the single crystals and measure the thermoelectric properties to evaluate $z_{\perp}T$ and critical angles demonstrated in Section 4.2.2. Eventually, new $p \times n$ -type TTE materials can also be rapidly searched using the criteria illustrated in Section 4.1 given the computational capacity of Material Genome community.

CHAPTER 5

Towards Thermal and Electrical Characterization of Thin-Film $p \times n$ -type Transverse Thermoelectrics

Besides the ambipolar compounds discussed in the previous chapter, the $p \times n$ -type behavior can also be achieved by engineering the band structure of intrinsic semiconductor superlattices[30, 32], such as InAs/GaSb type-II superlattice (T2SL). Its band gap can be continuously tuned to zero by varying the thickness of electron/hole well width, which, in principle, allows the T2SL to operate at any temperatures provided that the effective band gap is on par with the thermal energy scale $E_g \sim k_B T$. To evaluate the figure of merit for this material as TTE, electrical and thermal transport measurements are required.

This chapter demonstrates the electrical and thermal characterization of InAs/GaSb type-II superlattice (T2SL) as a thin-film $p \times n$ -type TTE. In addition to the cross-plane thermal conductivity measurement using a wide filament described in Section 2.3, this Section 5.1 introduces the in-plane thermal conductivity characterization technique called 2-wire 3ω method, followed by a case study on a InAs/AlSb T2SL. For electrical characterization, Section 5.2 discusses improvements in a data analysis technique called Fourier-domain Mobility Spectrum Analysis (FMSA) to deconvolve the magnetotransport data and deduce the characteristics of both electrons and holes in a multi-carrier system. Although the thermal conductivity and electrical transport will be measured on a generic T2SL, not one specifically designed to be a $p \times n$ TTE, the results here will establish a

proof-of-concept of which methods of analysis work as planned, and which have uncovered subtleties that will need more advanced consideration to attack the problem at hand.

5.1. Thermal Characterization: 2-wire 3ω Method

Compared with cross-plane thermal conductivity, in-plane thermal conductivity can only be derived when the heat conduction from the filament on the film surface to the substrate is two-dimensional, whereby the filament width should be smaller than or of the same order as the film thickness so that the in-plane components of heat conduction are of the same order as the out-of-plane components. As shown in Figure 5.1(a), the measurement device for determining in-plane thermal conductivity has two filaments (1 wide 1 narrow) on both the film and substrate[138] where half the film is etched. Empirically, the narrow filament width should be close to or smaller than the film thickness t , and the wide filament width should be at least one order of magnitude larger than the film thickness t . Figure 5.1(b) gives a mask design example. The $4\text{-}\mu\text{m}$ -wide narrow filament and $80\text{-}\mu\text{m}$ -wide narrow filament therein should be suitable for measuring a film with $t = 5\text{ }\mu\text{m}$ or below. For films in sub-micron thickness, e-beam lithography is needed to pattern narrow filaments below a $1\text{ }\mu\text{m}$ linewidth.

The in-plane thermal conductivity is determined by an iterative fitting process using the equations described below. The generalized heat conduction for a multi-layer system is derived as [140]

$$(5.1) \quad \Delta T = \frac{-P}{\pi l \kappa_{y1}} \int_0^\infty \frac{1}{A_1 B_1} \frac{\sin^2(b\lambda)}{b^2 \lambda^2} d\lambda,$$

$V_{3\omega}^{f,wide}$ from the wide filaments, as described in Section 2.3. By fitting to the temperature oscillation converted from 3ω voltage from the narrow filament on the substrate (or substrate plus dielectric layer, for conductive samples), namely $V_{3\omega}^{s,narrow}$, the filament width $2b$ (as well as top-layer dielectric film thickness and dielectric thermal conductivity if for conductive samples) can be first calibrated. These parameters, as well as the cross-plane thermal conductivity of the thin film of interest derived from the wide filaments, together can be plugged into fitting the temperature oscillations obtained from $V_{3\omega}^{f,narrow}$ from the narrow filament on the film, after which the thin-film in-plane thermal conductivity can be determined. The conversion between 3ω voltage and 2ω temperature oscillation is performed by using Equation 2.2.

Due to lack of availability of an InAs/GaSb T2SL designed specifically as a $p \times n$ TTE, a 2-wire 3ω measurement was conducted on a similar T2SL InAs/AlSb to examine the temperature dependence of both cross-plane and in-plane conductivity.[86] This material is widely used as the cladding layer in interband cascade lasers (ICL), where the continuous wave performance degrades rapidly once the injection current becomes high enough to heat the ridge. So measuring the thermal conductivity would provide useful information for ICL simulations and guide optimization of device performance.

The cladding sample consisted of a 7- μm -thick (8 ML n-InAs/8 ML AlSb) SL layer and a 500-nm GaSb buffer layer grown on the n-GaSb substrate. For the sample processing, half of the cladding sample was left unetched, whereas the other half was etched to a depth of 7 μm to the buffer layer. Then, a 70-nm-thick SiN_x layer was deposited by plasma enhanced chemical vapor deposition (PECVD) over the full area of sample surface. With

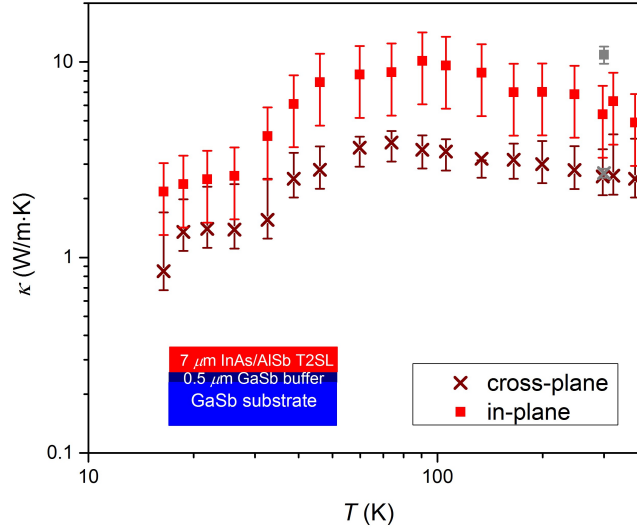


Figure 5.2. Temperature-dependent in-plane and cross-plane thermal conductivity of InAs/AlSb T2SL, where the grey datapoints are room-temperature results from Reference [138].

photolithography, 300-nm-thick nickel filaments of widths $W_1 = 80 \mu\text{m}$ and $W_2 = 7 \mu\text{m}$ patterned were deposited on the sample.

InAs/AlSb was measured in a cryogenic system from $T = 15 \text{ K}$ to 324 K , as the results shown in Figure 5.2. First, the cross-plane thermal conductivity was deduced from the differential 3ω voltage between the wide filaments on the etch and unetched sides, namely the filaments on T2SL film and buffer layer respectively. Then the 3ω voltage from the narrow filaments is used to fit the in-plane thermal conductivity. The characterization indicates a slight increase of the thermal conductivities down to $T \approx 77 \text{ K}$, followed by a more rapid drop at lower temperatures. The cross-plane thermal conductivities are consistently about a factor of $2.5 \sim 3.0$ smaller than the in-plane thermal conductivities, resulting from the interface scattering of phonons along the c -axis of superlattice. The

cross-plane κ at room temperature is consistent with previous study[138] only conducted at room temperature.

Similar to InAs/AlSb T2SL measured here, InAs/GaSb as TTE candidate is expected to have a higher in-plane κ than that in the cross-plane direction. Besides the room-temperature measurement was performed elsewhere[138], the temperature-dependent study needs to be done to enable the figure of merit estimate in a wide temperature range, given the potential flexibility of $p \times n$ -type in operation temperature.

5.2. Electrical Characterization: Fourier-domain Mobility Spectrum Analysis

Parallel conduction, in which multiple carrier species contribute simultaneously to the total electrical conduction, is common effect in many narrow-gap semiconductors, such as the $p \times n$ -type transverse thermoelectrics where electrons and holes with different mobilities and densities coexist. In the past few decades, a great deal of research has analyzed magnetotransport data as a function of magnetic field to extract the electrical properties of each carrier species in such samples with mixed conduction. Gold and Nelson [141] conducted a multi-carrier fit to study the Hg vacancy in HgCdTe, a common narrow-gap infrared detector material, but prior knowledge of the carrier type and number of species is required a priori for this method. The concept of mobility spectrum analysis was first proposed by Beck and Anderson [142], where their mathematical procedure deduced a qualitative spectral envelope giving the maximum possible carrier conductivity for each spectral mobility in HgCdTe and GaAs/AlGaAs heterostructures. Combining the two above techniques together, Meyer *et al.*[143] presented a hybrid mixed conduction analysis. The first automated algorithm without subjective intervention called quantitative

mobility spectrum analysis (QMSA) was developed by Antoszewski *et al.*[144] and Meyer *et al.*[145], and later an improved version called improved QMSA (i-QMSA)[146] was introduced. Kiatgamolchai *et al.*[147] employed a different approach using the maximum entropy principle, and invented the maximum entropy mobility spectrum analysis (MEMSA), claiming that compared with i-QMSA their technique requires fewer data points and is less sensitive to experimental noise. Most recently, the high resolution mobility spectrum analysis (HRMSA)[148] was reported to have improved robustness and greater resolution, but the underlying algorithm has not been published and it may be computationally slower than other methods.

We introduce a new method called Fourier-domain Mobility Spectrum Analysis (FMSA), which has an intuitively simple algorithm, fast convergence, low computational cost, simplicity of implementation, and good fitting accuracy. The algorithm is described in the following section, followed by its demonstration on various synthetic datasets to verify reliability.

5.2.1. Algorithm

The electrical conductivity tensor components for a multi-carrier system are based on the Drude model in the classical physics regime. The longitudinal and transverse conductivities are expressed as

$$(5.2) \quad \begin{aligned} \sigma_{xx}(B_j) &= \sum_i^M \frac{n_i e \mu_i}{1 + \mu_i^2 B_j^2} = \sum_i^M A_{xx}^{ij} [s_p(\mu_i) + s_n(\mu_i)] \\ \sigma_{xy}(B_j) &= \sum_i^M \frac{\alpha_i n_i e \mu_i^2 B_j}{1 + \mu_i^2 B_j^2} = \sum_i^M A_{xy}^{ij} [s_p(\mu_i) - s_n(\mu_i)] \end{aligned}, \quad \text{where} \quad \begin{aligned} A_{xx}^{ij} &= \frac{1}{1 + \mu_i^2 B_j^2} \\ A_{xy}^{ij} &= \frac{\mu_i B_j}{1 + \mu_i^2 B_j^2} \end{aligned}.$$

Here α_i is a sign constant which is -1 for electrons and $+1$ for holes, and A_{xx}^{ij} and A_{xy}^{ij} transform the conductivity spectra $s_n(\mu)$ and $s_p(\mu)$ into the conductivities $\sigma_{xx}(B)$ and $\sigma_{xy}(B)$, respectively. The spectral carrier conductivities $s_n(\mu_i) = n_i e \mu_i$ and $s_p(\mu_i) = p_i e \mu_i$ correspond to a number density of electrons n_i or holes p_i with mobility μ_i . The index i and j refer to the indices of the mobility and the magnetic field, respectively. The conductivity at the j^{th} value of the magnetic field $\sigma(B_j)$ is the sum over all M mobilities with the index i , where M is the total number of the spectral mobilities. In order to evaluate the fit, the error is calculated at each magnetic field, and the total average error is defined as

$$(5.3) \quad \chi^2 = \sum_j \frac{1}{N} \frac{[\sigma_{xx}(B_j) - \sigma_{xx}^{exp}(B_j)]^2 + [\sigma_{xy}(B_j) - \sigma_{xy}^{exp}(B_j)]^2}{[\sigma_{xx}^{exp}(B_j)]^2 + [\sigma_{xy}^{exp}(B_j)]^2}.$$

This represents the sum of the squared error fraction at all the magnetic fields divided by the number of total number of data points N .

The novelty of the present method is to fit the spectral conductivities $s_n(\mu)$ and $s_p(\mu)$ with an iterative “up/down” adjustment in *both* the mobility domain and its Fourier reciprocal domain, in succession. Here we define “mobility domain” as the traditional space for the spectral conductivity $s(\mu)$ where carrier mobility μ is the independent variable; meanwhile its reciprocal space “Fourier domain” is the Fourier transform of the spectral conductivity $\tilde{S}(\mu^{-1})$ where the reciprocal mobility μ^{-1} serves as the independent variable with the units of magnetic field. The transformation between the mobility spectrum $s(\mu)$ and its Fourier spectrum $\tilde{S}(\mu^{-1})$ is implemented using discrete Fourier transform (DFT)

and inverse inverse discrete Fourier transform (iDFT) as shown below

$$(5.4) \quad \begin{aligned} \tilde{S}(\mu_i^{-1}) &= \sum_{k=1}^M s(\mu_k) e^{-\frac{2\pi i}{M}(k-1)(l-1)} \\ s(\mu_k) &= \frac{1}{M} \sum_{l=1}^M \tilde{S}(\mu_i^{-1}) e^{-\frac{2\pi i}{M}(k-1)(l-1)}, \end{aligned}$$

where l and k are the indices of the variable μ for mobility domain and μ^{-1} for Fourier domain, respectively.

FMSA saves much computational effort compared with prior MSA methods. Unlike prior methods[144, 145, 146] requiring separate computational algorithm for the envelope from Beck and Anderson[142] as the initial guess, the iterative process begins with a constant carrier conductivity for all the mobility points equally spaced on a log-scale axis, for instance $s_n = s_p = 1$ S/m. The full FMSA follows the protocol in Figure 5.3(a) mainly consisting of two subroutines: mobility-domain up/down in Figure 5.3(b) and Fourier-domain up/down in Figure 5.3(c).

5.2.1.1. Mobility-domain up/down. In the mobility domain, the fitting procedure is intuitively simple, with a flow chart shown in Figure 5.3(b). One first considers a spectral conductivity at a certain mobility point with an index k . The carrier conductivity $s_n(\mu_k)$ or $s_p(\mu_k)$ is tentatively increased by multiplying by a certain factor $(1 + f)$ and a comparison is made to see if the total error χ^2 is reduced. If the total error is decreased, the change is made; otherwise the conductivity is reduced by multiplying by the factor $(1 - f)$. The spectral point is modified only if the adjustment could decrease χ^2 . If neither moving up nor down can enhance the fit, then the next mobility point with a different index k is considered. The typical value used for f is 2 % from the beginning of

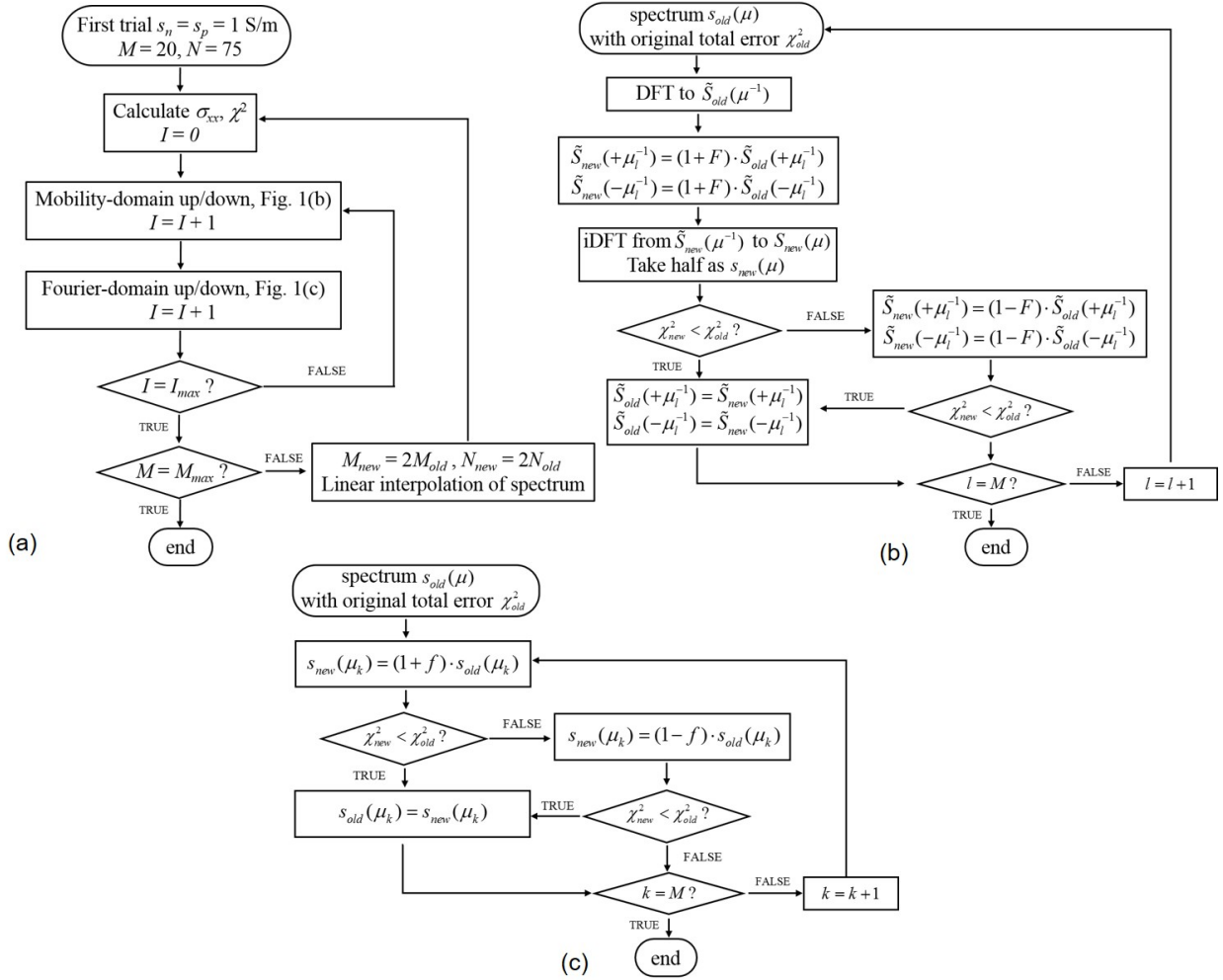


Figure 5.3. Flow chart of (a) the full FMSA general procedure with (b) mobility-domain up/down and (c) Fourier-domain up/down. Note that the multiplicative adjustment factors f and F are reduced with each iteration I , as described in the text.

each resolution step, and it is linearly decreased to 0.005 % at the end of that resolution step. We refer to the mobility-domain as a local adjustment since at every iteration the modification is made only at a single mobility point.

5.2.1.2. Fourier-domain up/down. A Fourier-domain adjustment is introduced here to complement mobility-domain up/down just described. As the flow chart shows in

Figure 5.3(c), the spectrum $s(\mu)$ is first Fourier transformed into its Fourier spectrum $\tilde{S}(\mu^{-1})$. The modification is then made simultaneously on two symmetric Fourier spectral points $\tilde{S}(+\mu_i^{-1})$ and $\tilde{S}(-\mu_i^{-1})$. The up/down adjustment for a given index l in Fourier-space is made analogously to the mobility-domain method, and its adjustment factor $F = f$ uses the same percent values from 2 % to 0.05 % as used in the mobility-domain up/down iteration immediately prior. Because modifications in the reciprocal space affect all the points in the real space, we refer to this Fourier-domain up/down technique as globally affecting the mobility spectrum.

In general, the local mobility-domain adjustment can suppress the extraneous spectral features, while the global Fourier-domain up/down is able to reconstruct accurate linewidths and generate smoother fittings. The success of the FMSA technique in alternating between these two local and global domains is demonstrated with synthetic datasets in the following section.

With the adjustments switching between the two domains described above, the FMSA method is able to achieve rapid convergence to a rough spectrum as the initial guess, and then progressively increases resolution as the convergence rate slows down. After fitting the initial guess with a low resolution $M_0 = 20$ where M_0 is the number of spectral points, then the resolution is increased to $M_1 = 40$ and finally $M_2 = 80$ during the three-step resolution improvement. Meanwhile the number of fitted conductivity data points N spanning the whole B range (0.01-15 T) is also increased from $N_0 = 75$, $N_1 = 150$ to finally $N_2 = 300$. Every time the spectral resolution is doubled, the first guess of the fitting spectrum $s(\mu)$ at higher resolution is linearly interpolated in this log scale, while the fitted data also has twice the resolution with the data points doubled at equal spacing

along a logarithmic scale of the full B -field range of data from 0.01-15 T. The number of data points in the Fourier-domain doubles as the mobility-domain resolution doubles since the Fourier transform and its inverse both sum over the same number of points M .

5.2.2. Results of Pure FMSA

The fitting procedure is tested on various synthetic datasets below. In synthetic datasets, each carrier distribution is a Gaussian-like peak

$$(5.5) \quad s(\mu) = A \cdot e^{-\frac{(\mu - \mu_0)^2}{2w^2}},$$

where A , μ_0 and w are constants defining the amplitude, central mobility and width of the carrier peak in $s(\mu)$, respectively. Taking this assumed conductivity spectrum, a conductivity tensor is calculated using the mapping matrices A_{xx} and A_{xy} in Eq. 5.5, and then the resulting conductivities $\sigma_{xx}(B)$ and $\sigma_{xy}(B)$ are substituted for input experimental data. The FMSA method then generates a fit, which is compared with the originally assumed spectrum to test the effectiveness of this technique. Such synthetic datasets have no measurement noise and assume perfect sample homogeneity, but are nonetheless helpful as a means of controllably testing the algorithm[142, 146, 147, 148]. The mobility range spans almost four orders of magnitude from $\mu_{min} = 670 \text{ cm}^2/(\text{V}\cdot\text{s}) (= 1/B_{max})$ to $\mu_{max} = 1,000,000 \text{ cm}^2/(\text{V}\cdot\text{s})(= 1/B_{min})$, where this lower limit on reliability is set by the maximum magnetic field in the magnetotransport measurement $B_{max} = 15 \text{ T}$ in this simulation, and the higher limit is determined by the lowest magnetic field $B_{min} = 0.01 \text{ T}$ in this simulation. A convergence plot is introduced in Figure 5.6 to plot the total error trend χ^2 as a function of iteration index I throughout the fitting process.

We begin by conducting an MSA fit in direct-domain only to illustrate the limitations of such a simple approach. For the first synthetic dataset, a carrier system is assumed where there coexist one electron species and one hole species with $\mu_{c,1} = 40,000 \text{ cm}^2/(\text{V}\cdot\text{s})$, $w_1 = 2236 \text{ cm}^2/(\text{V}\cdot\text{s})$, and $\mu_{c,2} = 2,000 \text{ cm}^2/(\text{V}\cdot\text{s})$, $w_2 = 173 \text{ cm}^2/(\text{V}\cdot\text{s})$ respectively (Figure 5.4). The whole procedure is a three-step fitting with different spectral resolutions ($M_{0,1,2} = 20, 40$ and finally 80), each of which has iterations $I_0 = I_1 = I_2 = 2,000$. With only mobility-domain adjustment, a fairly good fit can be obtained judging from the conductivity fit in Figure 5.4(a), but the spectral fit needs improvement in Figure 5.4(b)). The peaks are too broad, resulting in a large deviation in the peak amplitude and linewidth. As the iterations continue, the local mobility-domain fit ceases to show improvement. From a signal analysis perspective, comparison between the final fit and the synthetic dataset clearly indicates that “high frequency” components in the signal are missing. Thus we transform the data to the Fourier domain to fit the Fourier coefficients associated with high frequencies thereby narrowing the peaks and lifting up the amplitude.

By implementing mobility-domain and Fourier-domain up/down alternately, a superior fit can be achieved with more accurate linewidth and amplitude. Figure 5.5 shows the spectra examined throughout the process of FMSA. With the same iteration number as in Figure 5.4, this full FMSA also implements two thousand iterations for each resolution step, resulting in a total of $I = 6,000$. In the lowest resolution with $M_0 = 20$ in Figure 5.5(a) through (d), the constant conductivity initial condition is slowly raised to a zigzag of the correct order in magnitude of conductivity after $I_0 = 200$ iterations of mobility-domain and Fourier-domain up/down coupled together in Figure 5.5(a). With more iterations, the wings of the peaks are suppressed, leading to a rough peak shape with

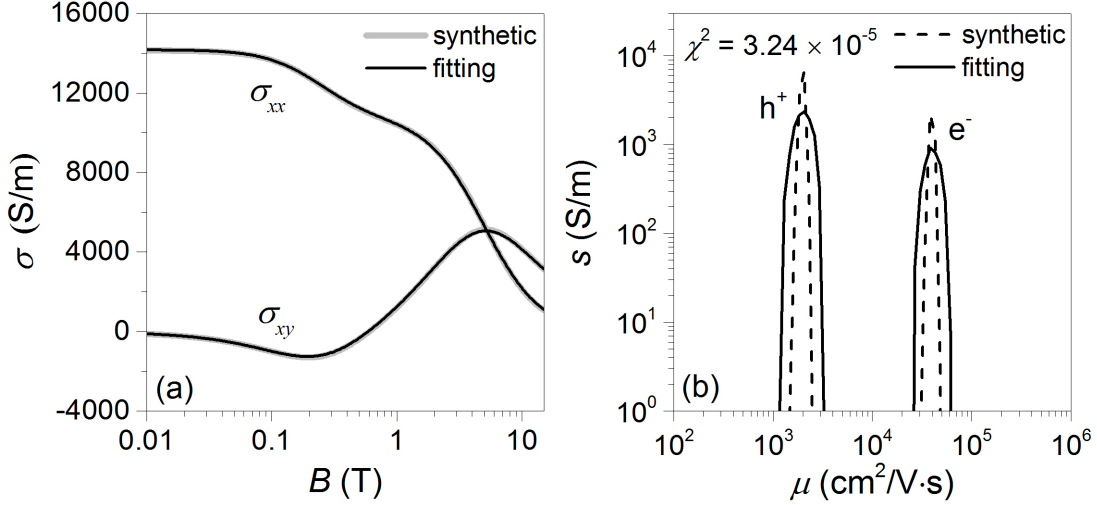


Figure 5.4. The conductivity and spectral fit after $I = 6,000$ iterations ($I_0 = I_1 = I_2 = 2,000$) of mobility-domain up/down technique alone ($M_0 = 20, M_1 = 40, M_2 = 80$), resulting in the total error $\chi^2 = 3.24 \times 10^{-5}$. The synthetic system has two species (one electron and one hole).

accurate amplitude halfway through the first resolution step with $M_0 = 20$ and $I_0 = 1,000$ in Figure 5.5(d). Each time the resolution is doubled, the fitting error reaches its next convergence rapidly, because the peak shape barely changes after two hundred iterations at $M_1 = 40$ and $M_2 = 80$ as shown in Figure 5.5(e) (h). So most of the feature recovery happens in the lowest-resolution step $M_0 = 20$ which also contains smallest number of fitting data points $N_0 = 75$, saving a significant amount of computational cost given the low resolution of the calculation. The resultant spectrum in this first resolution step serves as an envelope for the following fitting process, and is much more accurate than the Beck and Anderson envelope in QMSA[148], which needs a separate algorithm to generate the initial guess. In Figure 5.6 where the convergence trend of the full FMSA (Figure 5.5) and the mobility-domain up/down only (Figure 5.4) are plotted alongside each other,

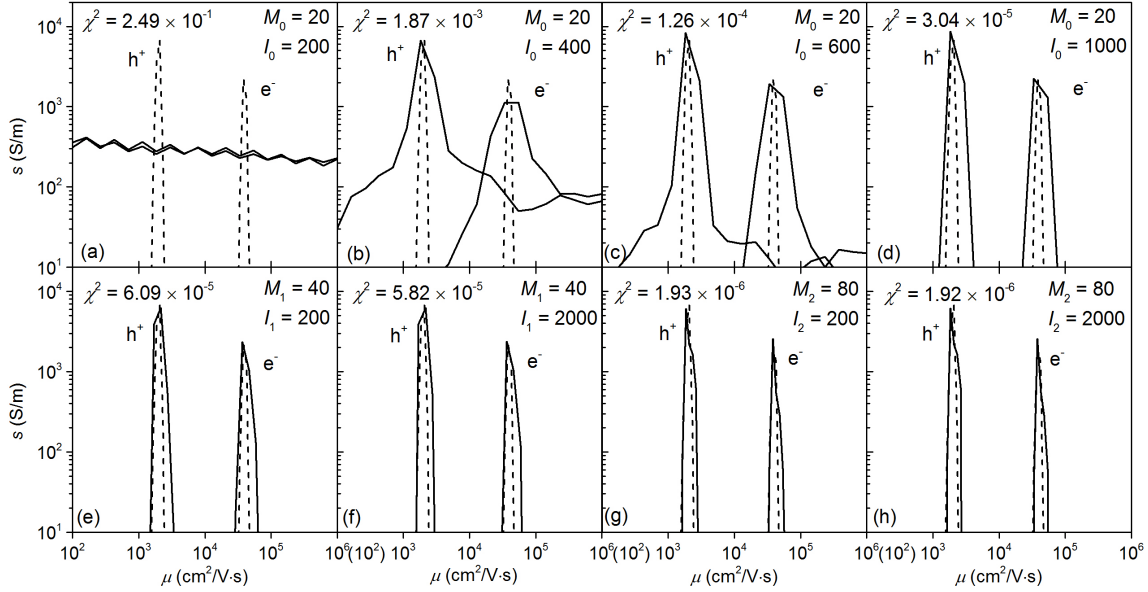


Figure 5.5. The spectral fit corresponding to the same synthetic dataset as Figure 5.4 examined throughout the full FMSA process, i.e. mobility-domain along with Fourier up/down techniques. Compared with Figure 5.4(b), it arrives at a mobility spectrum with an order of magnitude higher accuracy $\chi^2 = 1.92 \times 10^{-6}$, given the same total number of iterations $I = 6,000$.

it can be seen that the full FMSA combination of both mobility- and Fourier-domains converges more rapidly to lower errors than the mobility-domain adjustment alone when given the same number of iterations I . In fact, the $M_0 = 20$ initial round of full FMSA iteration achieves better accuracy than the $M_2 = 80$ final round of mobility-domain-only convergence, and finally reaches a total error over one order of magnitude lower than the that of mobility-domain adjustment alone. The large error spikes are due to the sudden transition in the number of mobility points M , but note that the FMSA method causes them to vanish quickly after only several iterations. FMSA is powerful in resolving wide peaks as well. Since this is a technique based on Fourier spectrum adjustment, the high

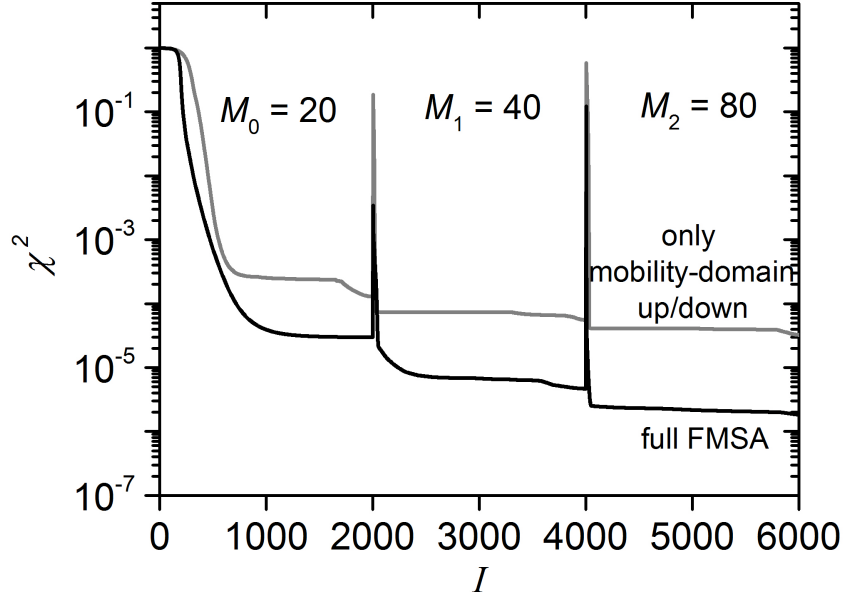


Figure 5.6. Convergence comparison of the squared-error χ^2 for the full FMSA (black) and for only the mobility-domain up/down technique (grey). The FMSA achieves more than an order of magnitude lower error.

frequency noise in the spectrum can be nicely suppressed during the Fourier up/down process, leading to smooth fitting features. As an example in Figure 5.7, a hole species coexists with an electron species with a broad mobility distribution[146]. FMSA is able to resolve the wide peak with good smoothness and accuracy in linewidth. Besides the simple cases above where only two carrier species are present, more complex systems can also be analyzed reliably with FMSA. Figure 5.8 illustrates an example where there are two electrons and two holes with alternately increasing mobilities[146], leading to three sign changes in σ_{xy} as a function of B as shown in Figure 5.8(a). All the four carriers are deconvolved successfully here in Figure 5.8(b), with special clarity in the three peaks with higher mobilities. The leftmost peak with the lowest mobility is not recovered as accurately because one is approaching the physical limit $\mu \sim 1/B_{max}$. Since the denominator

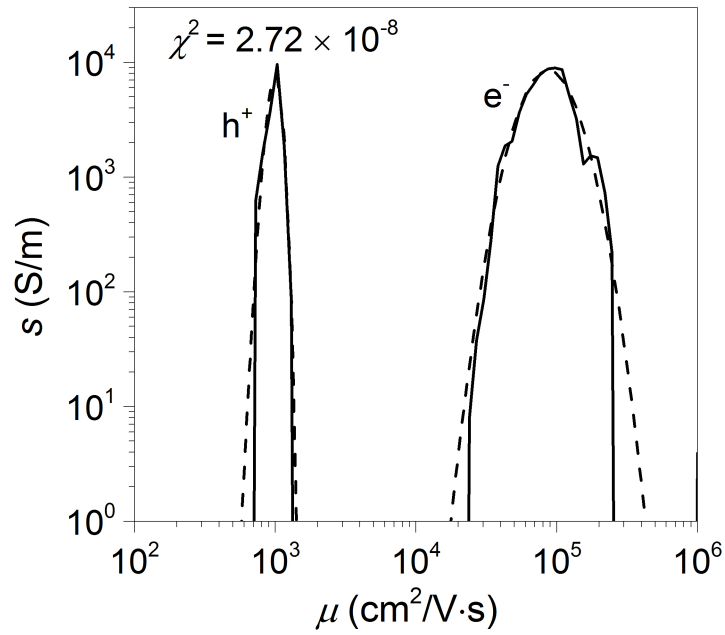


Figure 5.7. Application of FMSA on a system with one narrow and one wide carrier distribution (one electron and one hole species).

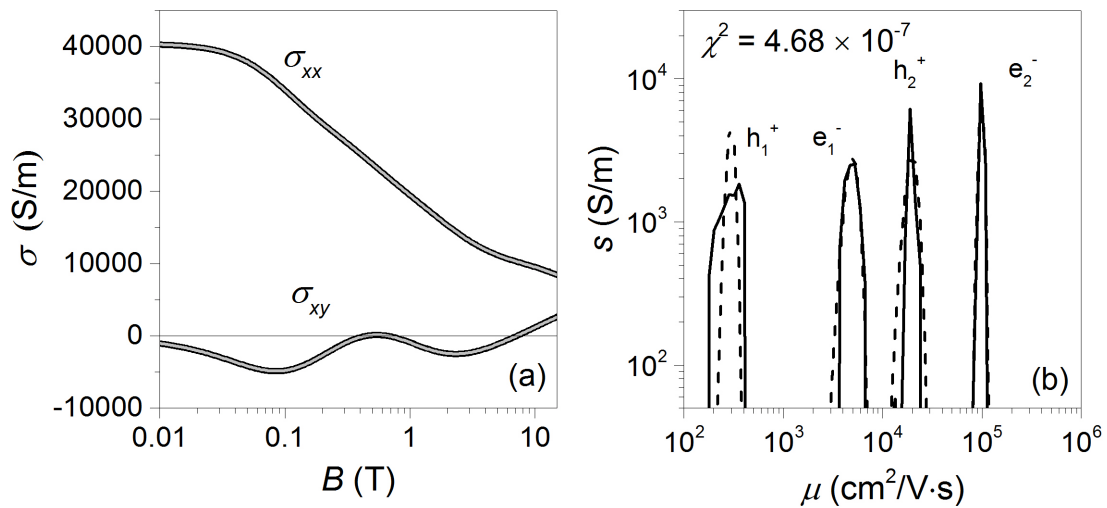


Figure 5.8. Application of FMSA on a system with four carrier species (two electron and two hole species).

of the conductivity definition (Eq. 5.2) approaches a constant value of 1 for the mobility $\mu < 1/B_{max}$, any spectral adjustment would make little difference to the conductivity spectral fit, hence the loss of accuracy. It can be better recovered if a larger B_{max} could be used in real experiments. For better resolve the low mobility carriers, an analysis method is developed to push the mobility limit below $1/B_{max}$, which is introduced in the following section.

5.2.3. Background Subtraction for Resolving Low-mobility Carriers in FMSA

Most MSA methods are based on the Drude model, such as the original quantitative MSA (o-QMSA)[144, 145], improved quantitative MSA (i-QMSA)[146], and our Fourier-domain MSA (FMSA) described in Section. 5.2. But the underlying Drude model also constrains the analysis, and usually one cannot recover meaningful information for carrier species with mobilities much lower than a threshold $\mu_{th} = 1/B_{max}$ defined as the reciprocal of the maximum magnetic field B_{max} in the magnetotransport measurement. According to the Drude definition, the FWHM (full-width-at-half-maximum) of σ_{xx} and the extremum of σ_{xy} occur at the same magnetic field B , whose reciprocal is the carrier mobility. Figure 5.9(a) shows the magneto conductivities for three different electron mobilities $\mu_{th}/10$, μ_{th} , and $10\mu_{th}$ with the same spectral carrier conductivity $s_n = 7,000$ (a.u.). Unlike the distinctly curved datasets for the high mobility $\mu = 10\mu_{th}$ trace, the low mobility data for $\mu = \mu_{th}/10$ are almost indistinguishable from straight lines throughout the whole magnetic field range, and would require an unrealistically large magnetic field $B > 1/\mu = 150$ T to reach the FWHM in σ_{xx} . Of previous efforts to tackle the low-mobility problem, one study was reported based on a multi-carrier fit, but required the

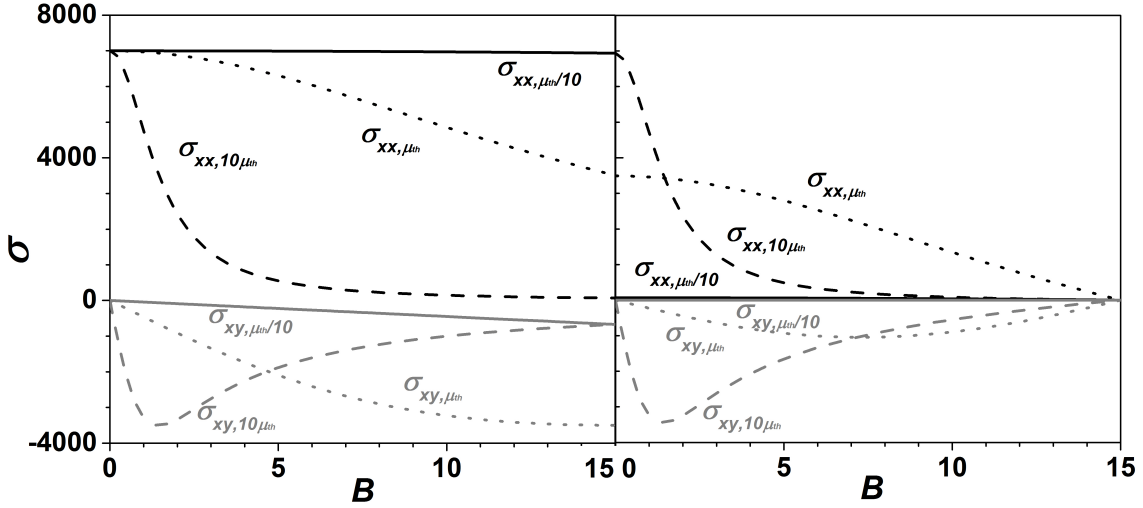


Figure 5.9. (a) Longitudinal (black) and transverse (grey) conductivity curves σ_{xx} and σ_{xy} for different mobilities $\mu_{th}/10$ (solid), μ_{th} (dotted), and $10\mu_{th}$ (dashed). (b) The same conductivities and after background subtraction (BGS) as defined in Eq. 5.6.

number of carriers and the carrier types to be known, defeating the purpose of the MSA method[149]. We propose an analysis that we call the background subtraction (BGS) method, which is executed prior to the standard FMSA. The BGS method serves to remove irrelevant spectral weight from the conductivity contribution of low mobility carriers resulting in a more accurate fit. After introducing the method below, various test results are shown in the subsequent sections to demonstrate the effectiveness of BGS particularly in the low-mobility regimes.

5.2.3.1. Algorithm. For low mobility carriers $\mu B_{max} \ll 1$, the denominators of $A_{xx}(B)$ and $A_{xy}(B)$ approach unity, meaning that low mobility species would result in a constant σ_{xx} independent of B and a sloped σ_{xy} linear with B , as was seen for and in Figure 5.9(a). The key idea of background subtraction is to *subtract these linear contributions* from the conductivities *before* fitting with MSA, thereby reducing the irrelevant spectral weight of

these curves so that the features that distinguish σ_{xx} and σ_{xy} from straight lines are more pronounced, as in Figure 5.9(b). The background subtracted conductivities are defined as

$$(5.6) \quad \begin{aligned} \overline{\sigma_{xx}}(B_j) &= \sigma_{xx}(B_j) - \sigma_{xx}(B_{max}) = \sum_i^M \overline{A_{xx}^{ij}} [s_p(\mu_i) + s_n(\mu_i)] \\ \overline{\sigma_{xy}}(B_j) &= \sigma_{xy}(B_j) - \frac{B}{B_{max}} \sigma_{xy}(B_{max}) = \sum_i^M \overline{A_{xy}^{ij}} [s_p(\mu_i) - s_n(\mu_i)] \end{aligned}$$

where

$$\begin{aligned} \overline{A_{xx}^{ij}} &= \frac{1}{1 + \mu_i^2 B_j^2} - \frac{1}{1 + \mu_i^2 B_{max}^2} \\ \overline{A_{xy}^{ij}} &= \mu_i B_j \left(\frac{1}{1 + \mu_i^2 B_j^2} - \frac{1}{1 + \mu_i^2 B_{max}^2} \right) \end{aligned}$$

Note that the mobility spectra s_p and s_n generated from the background-subtracted fits of Eq. 5.6 are the same as those from the standard method of Eq. 5.2. In MSA with BGS the new error-to-be-minimized is then defined as

$$(5.7) \quad \overline{\chi^2} = \sum_j^N \frac{1}{N} \frac{[\overline{\sigma_{xx}}(B_j) - \overline{\sigma_{xx}^{exp}}(B_j)]^2 + [\overline{\sigma_{xy}}(B_j) - \overline{\sigma_{xy}^{exp}}(B_j)]^2}{[\overline{\sigma_{xx}^{exp}}(B_j)]^2 + [\overline{\sigma_{xy}^{exp}}(B_j)]^2}.$$

With this subtraction step conducted first, the present paper applies the standard FMSA procedure to fit the spectral carrier conductivity s_n and s_p using $\overline{\sigma_{xx}}, \overline{\sigma_{xy}}, \overline{A_{xx}}$ and $\overline{A_{xy}}$ with the up-down adjustment in both direct mobility domain and the Fourier domain alternately as described in Section. 5.2.1.1 and 5.2.1.2. Once the BGS mobility spectra are deduced iteratively by minimizing $\overline{\chi^2}$ from Eq. 5.7, the final fitting error χ^2 from Eq. 5.3 is deduced for these BGS spectra and plotted in Figure 5.10 so that consistent comparison with and without BGS can be made. Also note that the BGS method described below

is not restricted to FMSA and should provide improvements for all Drude-model-based MSA methods.

5.2.4. Results of FMSA with BGS

To verify the effectiveness of BGS method, tests were conducted for FMSA without and with BGS for comparison. Synthetic datasets were employed with a single electron peak following the standard Gaussian lineshape as defined previously in Eq. 5.5. The central mobility value μ_0 shifts by three orders of magnitude ($\mu_0 = 40$ to $40,000 \text{ cm}^2/(\text{V}\cdot\text{s})$), while all the datasets share the same peak linewidth in log scale (i.e. $\mu_0/w \sim 8$ for all cases) for consistent comparison. Taking this assumed conductivity spectrum, the resulting conductivities $\sigma_{xx}(B)$ and $\sigma_{xy}(B)$ for $B = 0 - 15 \text{ T}$ ($B_{max} = 15 \text{ T}$) are used as input experimental data for the method. The FMSA then generates a fit minimizing $\overline{\chi^2}$, and then calculates the error χ^2 with Eq. 5.3 as a measure of the fit accuracy. Here the lower threshold mobility is $\mu_{th} = 1/B_{max} \sim 670 \text{ cm}^2/(\text{V}\cdot\text{s})$.

A plot of total error χ^2 for various μ_0 is shown as Figure 5.10. From the behavior observed therein, the mobility regime can be divided by two bounds $\mu_0 = 2\mu_{th}$, and $\mu_{th}/5$. For systems with carrier species $\mu_0 > 2\mu_{th}$, the mobilities are high enough that they make little contribution to the linear offset $\sigma_{xx}(B_{max})$ and $\sigma_{xy}(B_{max})$. So whether conducting BGS in FMSA makes no large difference in the resultant spectrum as well as the total error in most cases.

As the carrier mobility goes below $\mu_0 = 2\mu_{th}$, BGS begins to offer significant advantages over standard FMSA. First, BGS is able to reduce the total error by as much as four orders of magnitude (Figure 5.10) in the range $[\mu_{th}/5, 2\mu_{th}]$. Regarding the fit spectra,

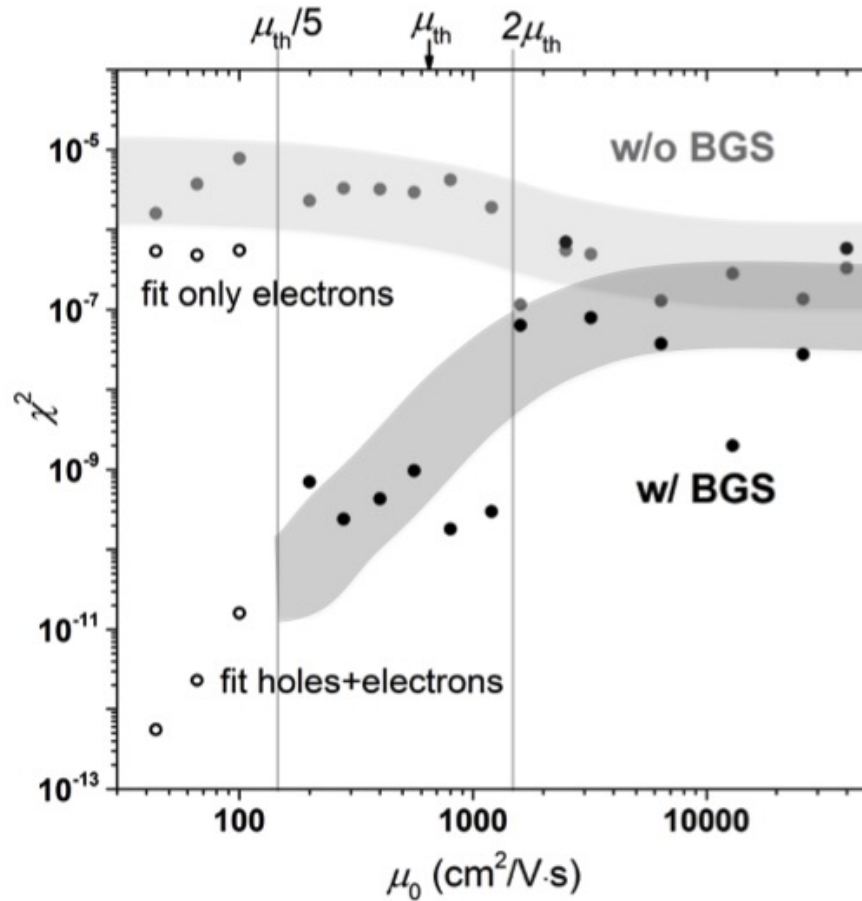


Figure 5.10. Comparison of FMSA total error χ^2 without BGS (grey) and with (black) BGS. The dots represent individual simulation fits, and the shaded regions represent guides to the eye to show the trends. Without BGS, the accuracy is slightly worse at low mobilities with increased χ^2 error. With BGS, the accuracy increases by 3 orders of magnitude for mobilities less than $2\mu_{th}$.

Figure 5.11 shows the advantage of BGS over standard FMSA for three different central mobility values from $\mu_0 = 800 \text{ cm}^2/(\text{V}\cdot\text{s})$ (Figure 5.11, top) to $\mu_0 = 200 \text{ cm}^2/(\text{V}\cdot\text{s})$ (Figure 5.11, bottom), where the purple shaded area is the mobility regime below μ_{th} . At the top $\mu_0 = 800 \text{ cm}^2/(\text{V}\cdot\text{s})$, the spectrum can be well recovered in both cases regardless of whether BGS is included with FMSA. As the peak moves to $\mu_0 = 400 \text{ cm}^2/(\text{V}\cdot\text{s})$, regular

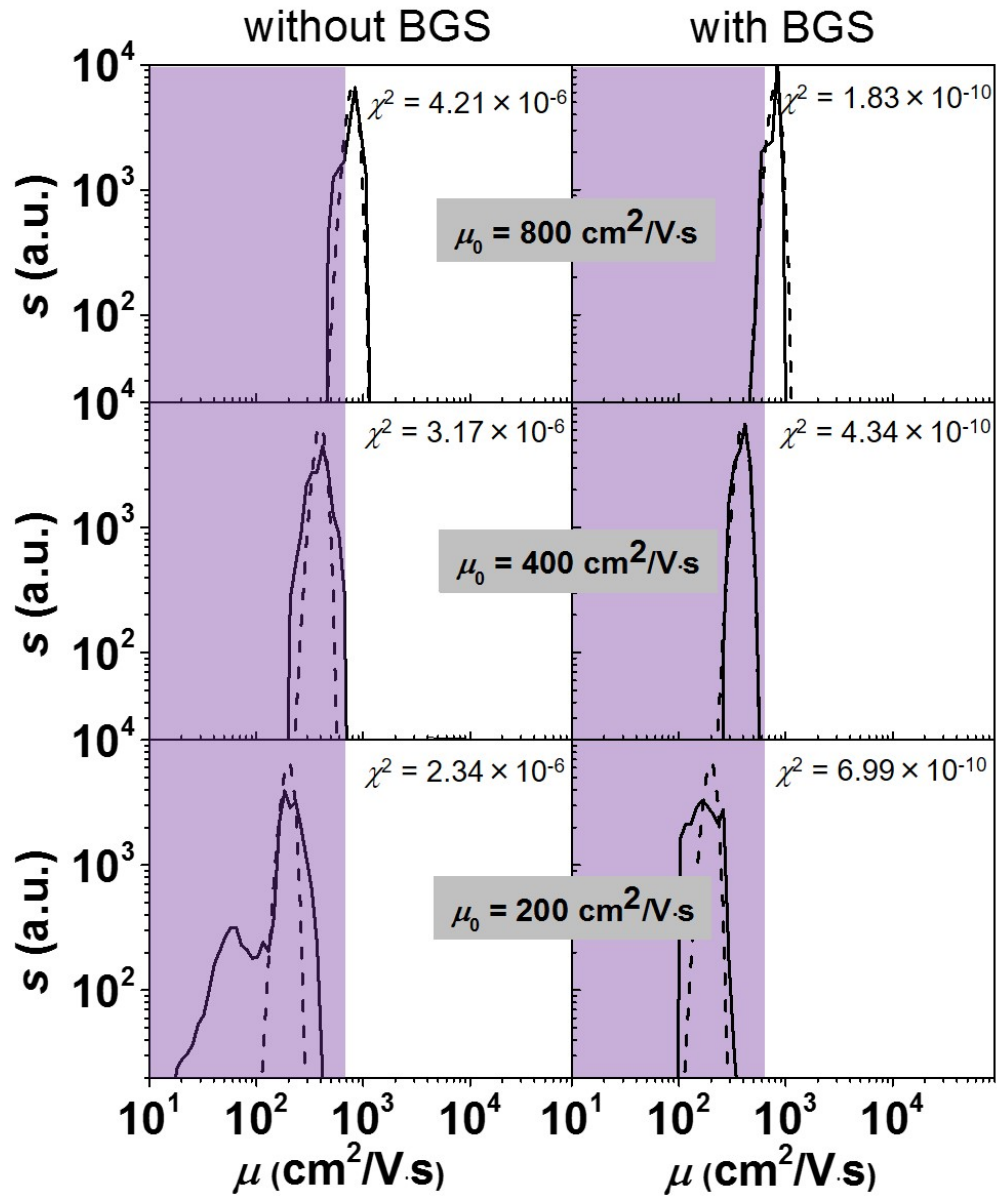


Figure 5.11. Comparison of FMSA fitting spectra without BGS (left) and with BGS (right) for a single electron peak centered at $\mu_0 = 800$, 400 and $200 \text{ cm}^2/(\text{V}\cdot\text{s})$, where the dashed line is the assumed synthetic data and the solid line shows the fit. The purple shaded area is the mobility regime below μ_{th} . Data shows that the BGS method (right) generates more accurate spectra with better lineshapes than standard FMSA (left).

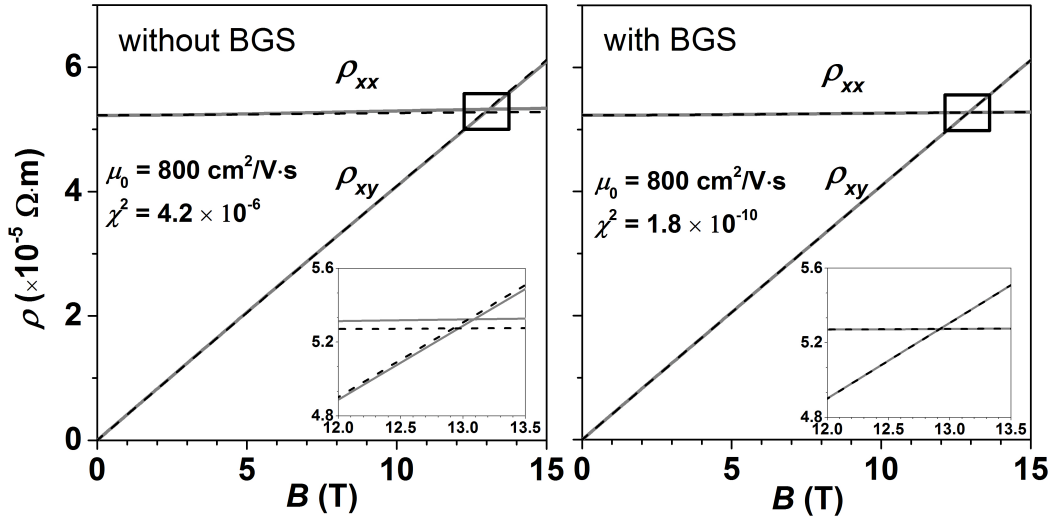


Figure 5.12. The fit of resistivity ρ_{xx} and ρ_{xy} shows a larger deviation for FMSA without BGS (left) than that with BGS (right), even though the two fit spectra look equally accurate in the conductivity spectrum plot. The inset figures are the zoomed-in version of the data around the intersection $\rho_{xx} = \rho_{xy}$. The fit is plotted in solid lines is clearly closer to the synthetic data in dashed lines in the right inset with BGS.

FMSA begins to show some widening in the lineshape fit, while BGS is able to perfectly restore the peak. At $\mu_0 = 200 \text{ cm}^2/(\text{V}\cdot\text{s})$, regular FMSA lost the shape of the fitting spectrum entirely, while BGS correctly identifies the line-shape.

The remarkable increase in accuracy for the BGS method is easiest to see not in the conductivity plots of Figure 5.11 top, but rather in resistivity plots at high magnetic field since low-mobility components play a more significant role at high fields. Figure 5.12 plots resistivity as a function of magnetic field. Without BGS (Figure 5.12 left) the fit in solid lines shows observable deviation from the synthetic data in dashed lines, while no error whatsoever can be seen when BGS is used (Figure 5.12).

For $\mu_0 < \mu_{th}/5$, however, the BGS method starts to fail. Figure 5.10 shows a false trend of even lower χ^2 if both electrons and holes are allowed to fit the data. However,

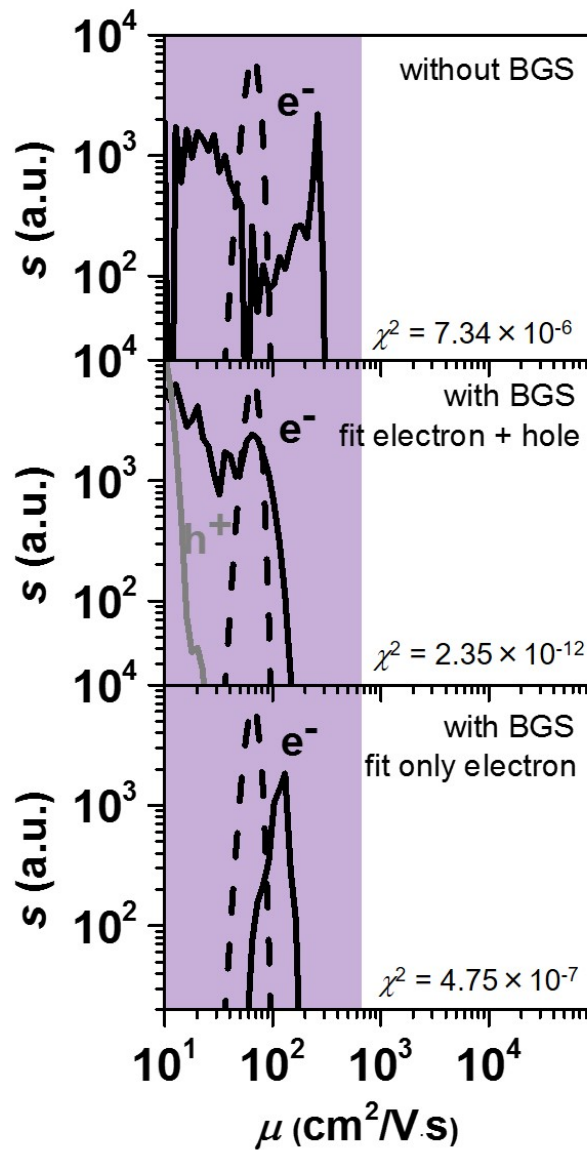


Figure 5.13. Comparison of FMSA fitting spectra for an extremely low central carrier mobility of $\mu_0 = \mu_{th}/10 = 66 \text{ cm}^2/(\text{V}\cdot\text{s})$. It is clear that the assumption of only one carrier type yields the best recovery of the lineshape.

in this case, the lower error results from the appearance of unphysical species of holes (grey). Figure 5.13 gives an example in this regime. Pure FMSA (top) only yields an inaccurately wide and noisy mobility range centered near the Gaussian peak. With

BGS (middle), FMSA provides a fit with a much smaller total error, but also brings an unphysical hole species at the low mobility limit. By intentionally suppressing holes and only fitting electrons (bottom), the total error increases significantly (Figure 5.10), but the BGS yields the proper lineshape with only about a factor of 2 error in μ_0 , which is remarkably good for such a low mobility. Thus, if the low-mobility carrier type is unipolar (n - or p -) and known in advance, the BGS method may help determine spectra down to even lower mobility values. At even lower mobilities $\mu_0 < \mu_{th}/10$, the peak amplitude starts to be significantly off. This sets the lower cutoff for reliability of the BGS method.

After the initial test on a single electron synthetic dataset, the code is tested on a multi-carrier system where one high-mobility electron species (black) coexists with one low-mobility hole species (grey) as shown in Figure 5.14. The electron has a fixed higher mobility at $\mu_0 = 80,000 \text{ cm}^2/(\text{V}\cdot\text{s})$, while the hole peak is centered at $\mu_0 = 200$ and $100 \text{ cm}^2/(\text{V}\cdot\text{s})$ far below the threshold mobility. In Figure 5.14 top row, pure FMSA is only able to resolve the high-mobility electron peak (top left). The low-mobility hole peak loses the line shape in the fit of pure FMSA, but was perfectly recovered with the help of BGS prior to FMSA which also lowers the fitting error by over 4 orders of magnitude (top right). When the hole peaks shifts further to $\mu_0 = 100 \text{ cm}^2/(\text{V}\cdot\text{s})$ in the bottom row, some nonphysical spectral feature of electron begins to appear at the low mobility limit if the fit is conducted by pure FMSA (bottom left). Again in this case BGS helps put less fitting power on the offset conductivity contributed from low mobility species, and successfully recovers both peaks accurately (bottom right) with a much lower χ^2 .

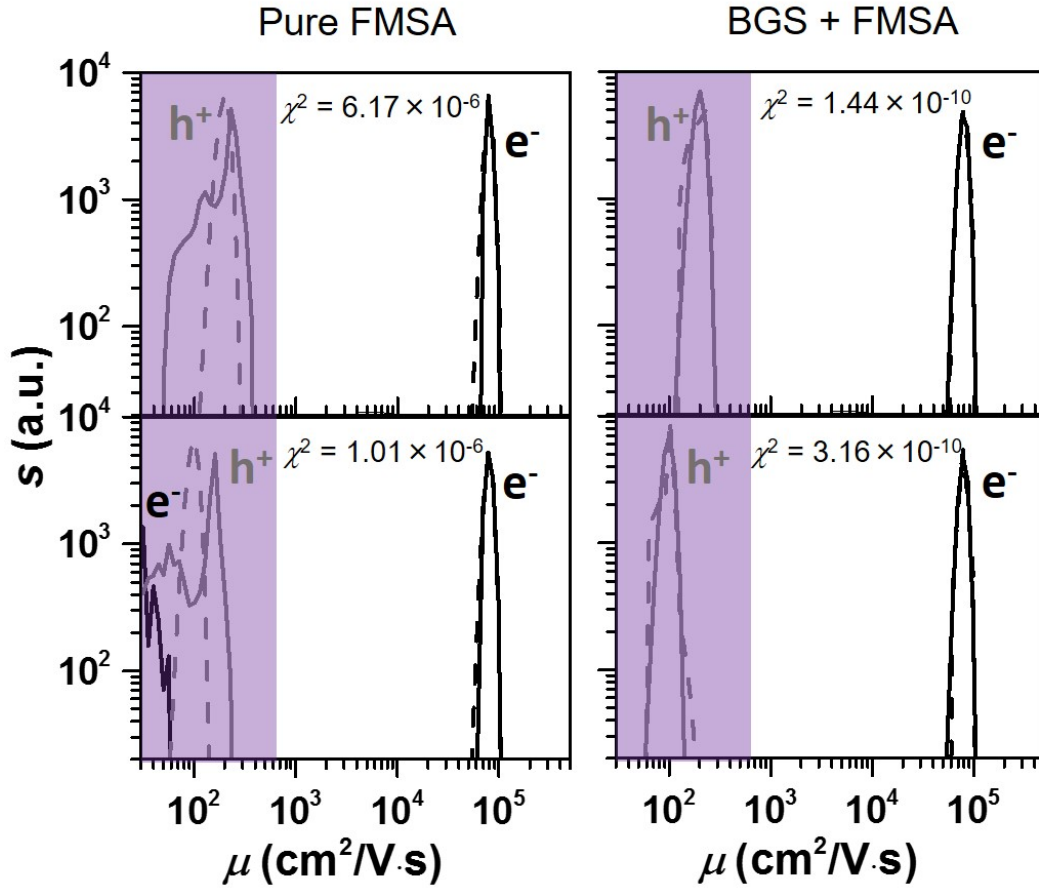


Figure 5.14. Comparison of FMSA fitting spectra without BGS (left) and with BGS (right) for a system where one electron species coexists with one hole species. The electron peak is fixed at a higher mobility $\mu_0 = 80,000 \text{ cm}^2/(\text{V}\cdot\text{s})$ while the hole peak is centered at $\mu_0 = 200$ and $100 \text{ cm}^2/(\text{V}\cdot\text{s})$ for top and bottom row respectively. The dashed line is the assumed synthetic data, and the solid line shows the fit.

5.2.5. Temperature-dependent Results on T2SL

Given the satisfying results on synthetic datasets above, the FMSA codes were tested by real experimental data on InAs/GaSb T2SL, which was measured in our cryogenic system with a 15 T magnet in the temperature range of $T = 10$ to 303 K. The sample

structure illustrated in Figure 5.15(a) was designed originally for optical applications such as infrared detectors, but has a similar layer structure to eventual T2SL TTE's. It is worth testing to verify the robustness of FMSA with experimental noise. The alternating single-crystal layers were observed in the transmission electron microscope (TEM) image in Figure 5.15(b). The magnetotransport result showed the signature of mixed conduction, for example at $T = 303$ K in Figure 5.15(c), with a pronounced curvature in both the longitudinal and transverse resistances R_{xx} and R_{xy} .

To analyze the data with FMSA, the results were converted from resistance to conductivity [Figure 5.15(d)] using the relation

$$(5.8) \quad \begin{aligned} \sigma_{xx} &= \frac{R_{xx}}{t(R_{xx}^2 + R_{xy}^2)}, \\ \sigma_{xy} &= \frac{-R_{xy}}{t(R_{xx}^2 + R_{xy}^2)} \end{aligned}$$

where t is the thickness of the sample. The pure FMSA code was implemented to fit the conductivities σ_{xx} and σ_{xy} for the temperatures where no resistance oscillation occurs as one would expect in classical regime.

The FMSA results are shown in Figure 5.16 at $T = 303$ K, 201 K, and 105 K. The spectral results are not as clean as those from synthetic datasets, which is expected given the experimental noise involved in data-taking process. The spectral transition from the top to the bottom manifests a slight mobility shift of electrons to lower mobilities with decreasing temperature. The electron density, which can be obtained by dividing the area under the corresponding peak by the central mobility value, also decreases by a factor of 2-3 every time from $T = 303$ K to 201 K, and finally to 105 K. The trends in both mobility and density indicate that thermal activation may be the main cause of electron

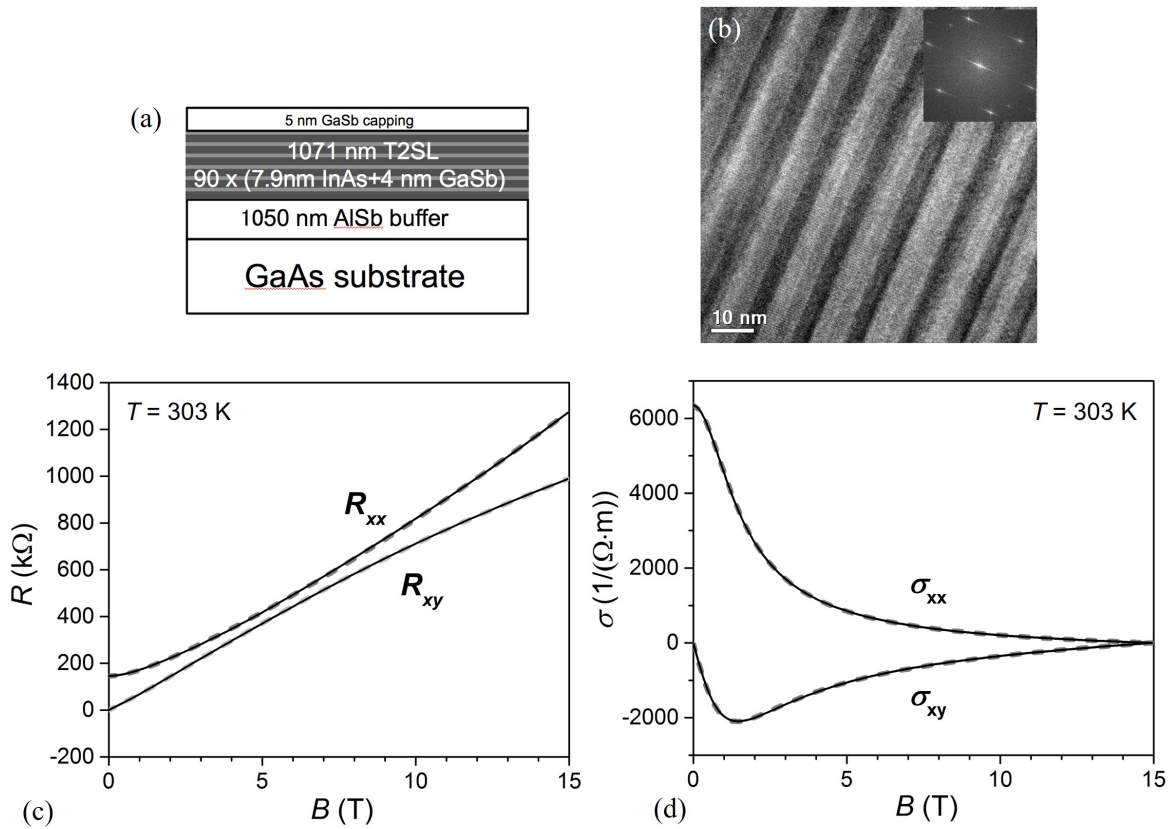


Figure 5.15. InAs/GaSb T2SL structure in (a) and TEM image in (b). The magnetotransport transport data at $T = 300$ K is shown in solid black lines in resistance (c) and conductivity (d), where the dashed grey lines are the FMSA fits.

conduction. At lower temperatures, electrons have lower thermal energy and tend to travel more slowly or fall back to the quantum well, leading to lower mobility and density.

What is concerning for these temperature-dependent results is that at every temperature there is always a hole species right next to the electron peak at $\mu_e \sim 8,000 \text{ cm}^2/(\text{V}\cdot\text{s})$. Some unphysical correlation between electrons and holes seems to be present, which is highly possible in this complicated system. If, for example, the scattering process in the T2SL is not fully explained by the classic Drude model, there would be artifacts in the

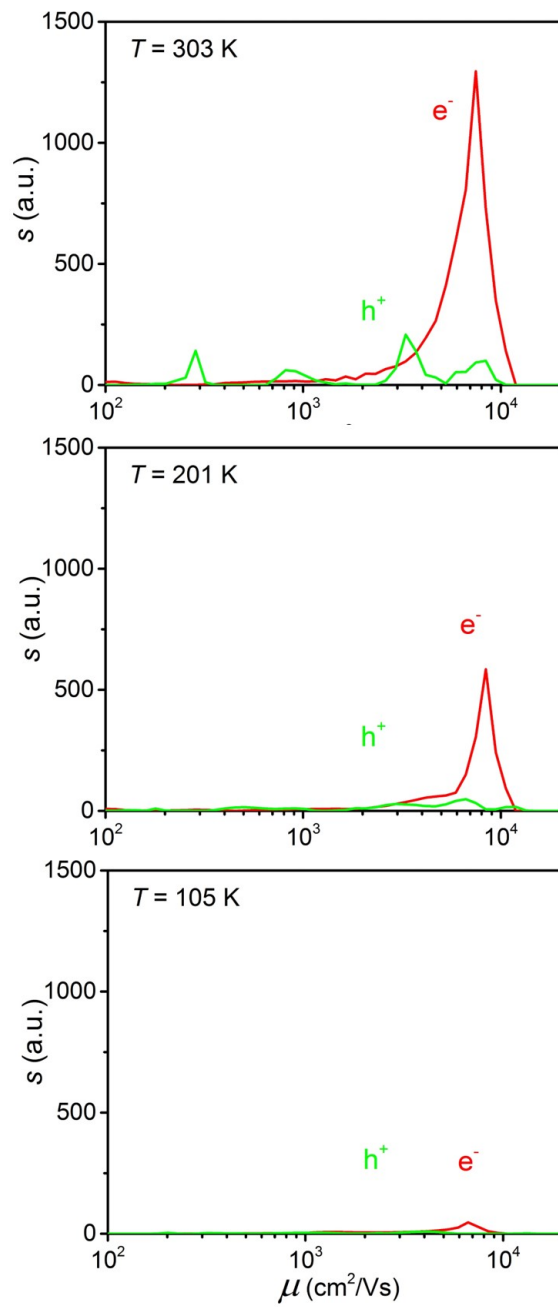


Figure 5.16. Mobility spectral results at $T = 303 \text{ K}$, 201 K , and 105 K , where the red curve corresponds to electrons and green curve corresponds to holes.

data that try to force the wrong lineshape fit to the data. Nonetheless, the FMSA technique is able to deconvolve the data with mixed conduction. It is expected to be employed in the future on other systems where the classic Drude model is valid, and can be modified to employ a non-Drude spectral lineshape to fit non-Drude systems, if needed.

5.3. Future Work

The temperature dependence of InAs/GaSb T2SL thermal conductivity can be examined in the future using the 2-wire 3ω method discussed in Section 5.1 for determining its $z_{\perp}T$, in addition to its room temperature study previously[138]. The optimization in FMSA may be achieved by using the built-in toolbox in Matlab, which would be much faster. Although the mobility-domain optimization has been successfully implemented with the toolbox, more future efforts are needed to integrate Matlab features to develop Fourier-domain optimization as well. The two characterization techniques will help evaluate the figure of merit of transverse thermoelectrics other than T2SL, and shed light on device design for effective thermal management, bringing new understanding to heat and charge transport in novel materials.

References

- [1] U EIA. International Energy Outlook 2016. *US Energy Information Administration (EIA)*, 2016.
- [2] Dolf Gielen, Francisco Boshell, and Deger Saygin. Climate and Energy Challenges for Materials Science. *Nat. Mater.*, 15(2):117–120, 2016.
- [3] Kyo Sung Park, Zheng Ni, Adrien P Côté, Jae Yong Choi, Rudan Huang, Fernando J Uribe-Romo, Hee K Chae, Michael O’Keeffe, and Omar M Yaghi. Exceptional Chemical and Thermal Stability of Zeolitic Imidazolate Frameworks. *Proc. Natl. Acad. Sci.*, 103(27):10186–10191, 2006.
- [4] Cory M Simon, Jihan Kim, Diego A Gomez-Gualdron, Jeffrey S Camp, Yongchul G Chung, Richard L Martin, Rocio Mercado, Michael W Deem, Dan Gunter, Maciej Haranczyk, et al. The Materials Genome in Action: Identifying the Performance Limits for Methane Storage. *Energy Environ. Sci.*, 8(4):1190–1199, 2015.
- [5] Alejandro Sáez and Mario Toledo. Thermal Effect of the Adsorption Heat on an Adsorbed Natural Gas Storage and Transportation Systems. *Appl. Therm. Eng.*, 29(13):2617–2623, 2009.

- [6] Barbara Schmitz, Ulrich Müller, Natalia Trukhan, Markus Schubert, Gérard Férey, and Michael Hirscher. Heat of Adsorption for Hydrogen in Microporous High-Surface-Area Materials. *ChemPhysChem*, 9(15):2181–2184, 2008.
- [7] Jinsong Zhang, Timothy S Fisher, P Veeraraghavan Ramachandran, Jay P Gore, and Issam Mudawar. A Review of Heat Transfer Sssues in Hydrogen Storage Technologies. *J. Heat Transfer*, 127(12):1391–1399, 2005.
- [8] Hailian Li, Mohamed Eddaoudi, Michael O’Keeffe, and Omar M Yaghi. Design and Synthesis of an Exceptionally Stable and Highly Porous Metal-Organic Framework. *Nature*, 402(6759):276–279, 1999.
- [9] Myunghyun Paik Suh, Hye Jeong Park, Thazhe Kootteri Prasad, and Dae-Woon Lim. Hydrogen Storage in Metal-Organic Frameworks. *Chem. Rev.*, 112(2):782–835, 2011.
- [10] Frameworks for Commercial Success. *Nat Chem*, 8(11):987–987, Nov 2016. Editorial.
- [11] Hui Wu, Wei Zhou, and Taner Yildirim. Hydrogen Storage in a Prototypical Zeolitic Imidazolate Framework-8. *J. Am. Chem. Soc.*, 129(17):5314–5315, 2007.
- [12] David Fairen-Jimenez, Raimondas Galvelis, Antonio Torrisi, Alistair D Gellan, Michael T Wharmby, Paul A Wright, Caroline Mellot-Draznieks, and Tina Dueren. Flexibility and Swing Effect on the Adsorption of Energy-Related Gases on ZIF-8: Combined Experimental and Simulation Study. *Dalton Trans.*, 41(35):10752–10762, 2012.

- [13] Kenji Nomura, Hiromichi Ohta, Kazushige Ueda, Toshio Kamiya, Masahiro Hirano, and Hideo Hosono. Thin-Film Transistor Fabricated in Single-Crystalline Transparent Oxide Semiconductor. *Science*, 300(5623):1269–1272, 2003.
- [14] Kenji Nomura, Hiromichi Ohta, Akihiro Takagi, Toshio Kamiya, Masahiro Hirano, and Hideo Hosono. Room-Temperature Fabrication of Transparent Flexible Thin-Film Transistors Using Amorphous Oxide Semiconductors. *Nature*, 432(7016):488–492, 2004.
- [15] Kenji Nomura, Akihiro Takagi, Toshio Kamiya, Hiromichi Ohta, Masahiro Hirano, and Hideo Hosono. Amorphous Oxide Semiconductors for High-Performance Flexible Thin-film Transistors. *Jpn. J. Appl. Phys.*, 45(5S):4303, 2006.
- [16] Hisato Yabuta, Masafumi Sano, Katsumi Abe, Toshiaki Aiba, Tohru Den, Hideya Kumomi, Kenji Nomura, Toshio Kamiya, and Hideo Hosono. High-Mobility Thin-Film Transistor with Amorphous InGaZnO_4 Channel Fabricated by Room Temperature RF-Magnetron Sputtering. *Appl. Phys. Lett.*, 89(11):2123, 2006.
- [17] Minkyu Kim, Jong Han Jeong, Hun Jung Lee, Tae Kyung Ahn, Hyun Soo Shin, Jin-Seong Park, Jae Kyeong Jeong, Yeon-Gon Mo, and Hye Dong Kim. High Mobility Bottom Gate InGaZnO Thin Film Transistors with SiO_x Etch Stopper. *Appl. Phys. Lett.*, 90(21), 2007.
- [18] Myung-Gil Kim, Mercuri G Kanatzidis, Antonio Facchetti, and Tobin J Marks. Low-Temperature Fabrication of High-Performance Metal Oxide Thin-Film Electronics via Combustion Processing. *Nat. Mater.*, 10(5):382–388, 2011.

- [19] Hideo Hosono. Ionic Amorphous Oxide Semiconductors: Material Design, Carrier Transport, and Device Application. *J. Non-Cryst. Solids*, 352(9):851–858, 2006.
- [20] Toshio Kamiya, Kenji Nomura, and Hideo Hosono. Present Status of Amorphous In-Ga-Zn-O Thin-Film Transistors. *Sci. Technol. Adv. Mater.*, 11(4):044305, 2010.
- [21] Tatsuji Nishijima, Seiichi Yoneda, Takuro Ohmaru, Masami Endo, Hiroki Denbo, Masashi Fujita, Hidetomo Kobayashi, Kazuaki Ohshima, Yutaka Shionoiri, Kiyoshi Kato, et al. 43.1: Low-Power Display System Driven by Utilizing Technique Using Crystalline IGZO Transistor. In *SID Symposium Digest of Technical Papers*, volume 43, pages 583–586. Wiley Online Library, 2012.
- [22] Hideaki Shishido, Kouhei Toyotaka, Masashi Tsubuku, Kousei Noda, Hiroki Ohara, Takeshi Nishi, Koji Moriya, Hiromichi Godo, Jun Koyama, Shunpei Yamazaki, et al. 76.1: High Aperture Ratio LCD Display Using In-Ga-Zn-Oxide TFTs without Storage Capacitor. In *SID Symposium Digest of Technical Papers*, volume 41, pages 1128–1131. Wiley Online Library, 2010.
- [23] Takuya Matsuo, Yosuke Kanzaki, Hiroshi Matsukizono, Akihiro Oda, Seiji Kaneko, Naoki Ueda, Yoshiharu Kataoka, Hedeaki Shishido, Kei Takahashi, Shunpei Yamazaki, et al. 76-1: Invited Paper: CAAC-IGZO Technology. In *SID Symposium Digest of Technical Papers*, volume 47, pages 1029–1032. Wiley Online Library, 2016.
- [24] Tien-Yu Hsieh, Ting-Chang Chang, Te-Chih Chen, Ming-Yen Tsai, Yu-Te Chen, Yi-Chen Chung, Hung-Che Ting, and Chia-Yu Chen. Origin of Self-Heating Effect Induced Asymmetrical Degradation Behavior in InGaZnO Thin-Film Transistors.

- Appl. Phys. Lett.*, 100(23):232101, 2012.
- [25] Hiromichi Ohta, Won-Seon Seo, and Kunihito Koumoto. Thermoelectric Properties of Homologous Compounds in ZnO-In₂O₃ System. *J. Am. Ceram. Soc.*, 79(8):2193–2196, 1996.
- [26] Deborah Susan Williams. *Thermoelectric Properties of a-IGZO*. PhD thesis, State University of New York at Binghamton, 2013.
- [27] Dong Kyu Seo, Sangwoo Shin, Hyung Hee Cho, Bo Hyun Kong, Dong Mok Whang, and Hyung Koun Cho. Drastic Improvement of Oxide Thermoelectric Performance Using Thermal and Plasma Treatments of the InGaZnO Thin Films Grown by Sputtering. *Acta Mater.*, 59(17):6743–6750, 2011.
- [28] Jun Hyeon Kim, Dong Kyu Seo, Cheol Hyoum Ahn, Sang Woo Shin, Hyung Hee Cho, and Hyung Koun Cho. Hybrid Solution Processed InGaO₃(ZnO)_m Thin Films with Periodic Layered Structures and Thermoelectric Properties. *J. Mater. Chem.*, 22(32):16312–16317, 2012.
- [29] EA Chávez-Urbiola, Yu V Vorobiev, and LP Bulat. Solar Hybrid Systems with Thermoelectric Generators. *Sol. Energy*, 86(1):369–378, 2012.
- [30] Chuanle Zhou, S Birner, Yang Tang, K Heinselman, and M Grayson. Driving Perpendicular Heat Flow:($p \times n$)-Type Transverse Thermoelectrics for Microscale and Cryogenic Peltier Cooling. *Phys. Rev. Lett.*, 110(22):227701, 2013.

- [31] Chuanle Zhou, Y Tang, and M Grayson. $p \times n$ -Type Transverse Thermoelectrics: An Alternative Peltier Refrigerator with Cryogenic Promise. In *SPIE OPTO*, pages 900006–900006. International Society for Optics and Photonics, 2014.
- [32] Yang Tang, Boya Cui, Chuanle Zhou, and Matthew Grayson. $p \times n$ -Type Transverse Thermoelectrics: A Novel Type of Thermal Management Material. *J. Electron. Mater.*, 44(6):2095–2104, 2015.
- [33] Yang Tang, Ming Ma, and M Grayson. Cooling Power of Transverse Thermoelectrics for Cryogenic Cooling. In *SPIE Defense+ Security*, pages 98210J–98210J. International Society for Optics and Photonics, 2016.
- [34] Don Monroe. Focus: A New Direction for Thermoelectric Cooling. *Physics*, 6:63, 2013.
- [35] Yang Tang, G Koblmüller, H Riedl, and M Grayson. Towards $p \times n$ Transverse Thermoelectrics: Extreme Anisotropic Conduction in Bulk Doped Semiconductor Thin Films via Proton Implantation. In *SPIE OPTO*, pages 976508–976508. International Society for Optics and Photonics, 2016.
- [36] Matthew Grayson and Chaunle Zhou. Anisotropic Ambipolar Transverse Thermoelectrics and Methods for Manufacturing the Same, September 9 2014. US Patent 8,829,324.
- [37] W Nernst et al. Ueber das Auftreten electromotorischer Kräfte in Metallplatten, welche von einem Wärmestrome durchflossen werden und sich im magnetischen

- Felde befinden. *Annalen der Physik*, 265(10):343–347, 1886.
- [38] BL Huang, AJH McGaughey, and M Kaviany. Thermal Conductivity of Metal-Organic Framework 5 (MOF-5): Part I. Molecular dynamics Simulations. *Int. J. Heat Mass Transfer*, 50(3):393–404, 2007.
- [39] BL Huang, Z Ni, A Millward, AJH McGaughey, C Uher, M Kaviany, and O Yaghi. Thermal Conductivity of a Metal-Organic Framework (MOF-5): Part II. Measurement. *Int. J. Heat Mass Transfer*, 50(3):405–411, 2007.
- [40] Justin Purewal, Dongan Liu, Andrea Sudik, Mike Veenstra, Jun Yang, Stefan Maurer, Ulrich Muller, and Donald J Siegel. Improved Hydrogen Storage and Thermal Conductivity in High-Density MOF-5 Composites. *J. Phys. Chem. C*, 116(38):20199–20212, 2012.
- [41] Xiaoliang Zhang and Jianwen Jiang. Thermal Conductivity of Zeolitic Imidazolate Framework-8: A Molecular Simulation Study. *J. Phys. Chem. C*, 117(36):18441–18447, 2013.
- [42] Hasan Babaei and Christopher E Wilmer. Mechanisms of Heat Transfer in Porous Crystals Containing Adsorbed Gases: Applications to Metal-Organic Frameworks. *Phys. Rev. Lett.*, 116(2):025902, 2016.
- [43] Luping Han, Makenzie Budge, and P Alex Greaney. Relationship between Thermal Conductivity and Framework Architecture in MOF-5. *Comput. Mater. Sci.*, 94:292–297, 2014.

- [44] Guang Lu and Joseph T Hupp. Metal-Organic Frameworks as Sensors: A ZIF-8 Based Fabry-Pérot Device as a Selective Sensor for Chemical Vapors and Gases. *J. Am. Chem. Soc.*, 132(23):7832–7833, 2010.
- [45] Huifeng Zhang, Defei Liu, Ying Yao, Baoquan Zhang, and YS Lin. Stability of ZIF-8 Membranes and Crystalline Powders in Water at Room Temperature. *J. Membr. Sci.*, 485:103–111, 2015.
- [46] Xinlei Liu, Yanshuo Li, Yujie Ban, Yuan Peng, Hua Jin, Helge Bux, Longya Xu, Jürgen Caro, and Weishen Yang. Improvement of Hydrothermal Stability of Zeolitic Imidazolate Frameworks. *Chem. Commun.*, 49(80):9140–9142, 2013.
- [47] David G. Cahill. Thermal Conductivity Measurement from 30 to 750 K: 3ω method. *Rev. Sci. Instrum.*, 61(2):802–808, 1990.
- [48] WS Capinski, HJ Maris, T Ruf, M Cardona, K Ploog, and DS Katzer. Thermal-Conductivity Measurements of GaAs/AlAs Superlattices Using a Picosecond Optical Pump-and-Probe Technique. *Phys. Rev. B*, 59(12):8105, 1999.
- [49] T Borca-Tasciuc and GANG Chen. Experimental Techniques for Thin-Film Thermal Conductivity Characterization. In *Thermal Conductivity*, pages 205–237. Springer, 2004.
- [50] Dongliang Zhao, Xin Qian, Xiaokun Gu, Saad Ayub Jajja, and Ronggui Yang. Measurement Techniques for Thermal Conductivity and Interfacial Thermal Conductance of Bulk and Thin Film Materials. *J. Electron. Packag.*, 138(4):040802,

2016.

- [51] David G. Cahill, M. Katiyar, and J. R. Abelson. Thermal Conductivity of a-Si:H Thin Films. *Phys. Rev. B*, 50(9):6077–6082, 1994.
- [52] Bao Yang and ZH Han. Thermal Conductivity Enhancement in Water-in-FC72 Nanoemulsion Fluids. *Appl. Phys. Lett.*, 88(26):261914, 2006.
- [53] SC Saxena and VK Saxena. Thermal Conductivity Data for Hydrogen and Deuterium in the Range 100-1100 Degrees C. *J. Phys. A: Gen. Phys.*, 3(3):309, 1970.
- [54] Laurent Bastin, Patrick S Barcia, Eric J Hurtado, Jose AC Silva, Alrio E Rodrigues, and Banglin Chen. A Microporous Metal-Organic Framework for Separation of CO₂/N₂ and CO₂/CH₄ by Fixed-Bed Adsorption. *J. Phys. Chem. C*, 112(5):1575–1581, 2008.
- [55] Jarad A Mason, Kenji Sumida, Zoey R Herm, Rajamani Krishna, and Jeffrey R Long. Evaluating Metal-Organic Frameworks for Post-Combustion Carbon Dioxide Capture via Temperature Swing Adsorption. *Energy Environ. Sci.*, 4(8):3030–3040, 2011.
- [56] Michael T Barako, Aditya Sood, Chi Zhang, Junjie Wang, Takashi Kodama, Mehdi Asheghi, Xiaolin Zheng, Paul V Braun, and Kenneth E Goodson. Quasi-Ballistic Electronic Thermal Conduction in Metal Inverse Opals. *Nano Lett.*, 16(4):2754–2761, 2016.

- [57] Michael T Barako, Shilpi Roy-Panzer, Timothy S English, Takashi Kodama, Mehdi Asheghi, Thomas W Kenny, and Kenneth E Goodson. Thermal Conduction in Vertically Aligned Copper Nanowire Arrays and Composites. *ACS Appl. Mater. Interfaces*, 7(34):19251–19259, 2015.
- [58] Toru Yoshikawa, Takashi Yagi, Nobuto Oka, Junjun Jia, Yuichiro Yamashita, Koichiro Hattori, Yutaka Seino, Naoyuki Taketoshi, Tetsuya Baba, and Yuzo Shigesato. Thermal Conductivity of Amorphous Indium Gallium Zinc Oxide Thin Films. *Appl. Phys. Express*, 6(2):021101, 2013.
- [59] Xinge Yu, Jeremy Smith, Nanjia Zhou, Li Zeng, Peijun Guo, Yu Xia, Ana Alvarez, Stefano Aghion, Hui Lin, Junsheng Yu, et al. Spray-Combustion Synthesis: Efficient Solution Route to High-Performance Oxide Transistors. *Proc. Natl. Acad. Sci.*, 112(11):3217–3222, 2015.
- [60] Jaroslav Fabian and Philip B Allen. Anharmonic Decay of Vibrational States in Amorphous Silicon. *Phys. Rev. Lett.*, 77(18):3839, 1996.
- [61] D Bruce Buchholz, Qing Ma, Diego Alducin, Arturo Ponce, Miguel Jose-Yacamán, Rabi Khanal, Julia E Medvedeva, and Robert PH Chang. The Structure and Properties of Amorphous Indium Oxide. *Chem. Mater.*, 26(18):5401–5411, 2014.
- [62] Georg Kresse and Jürgen Hafner. Ab Initio Molecular Dynamics for Liquid Metals. *Phys. Rev. B*, 47(1):558, 1993.

- [63] G Kresse and J Hafner. Ab Initio Molecular-Dynamics Simulation of the Liquid-metal-amorphous-semiconductor Transition in Germanium. *Phys. Rev. B*, 49(20):14251, 1994.
- [64] Georg Kresse and Jürgen Furthmüller. Efficient Iterative Schemes for Ab Initio Total-Energy Calculations Using a Plane-Wave Basis Set. *Phys. Rev. B*, 54(16):11169, 1996.
- [65] Georg Kresse and Jürgen Furthmüller. Efficiency of Ab-Initio Total Energy Calculations for Metals and Semiconductors Using a Plane-wave Basis Set. *Comput. Mater. Sci*, 6(1):15–50, 1996.
- [66] John P Perdew, Kieron Burke, and Matthias Ernzerhof. Generalized Gradient Approximation Made Simple. *Phys. Rev. Lett.*, 77(18):3865, 1996.
- [67] Koichi Momma and Fujio Izumi. VESTA 3 for Three-Dimensional Visualization of Crystal, Volumetric and Morphology Data. *J. Appl. Crystallogr.*, 44(6):1272–1276, 2011.
- [68] Altynbek Murat, Alexander U Adler, Thomas O Mason, and Julia E Medvedeva. Carrier Generation in Multicomponent Wide-Bandgap Oxides: InGaZnO₄. *J. Am. Chem. Soc.*, 135(15):5685–5692, 2013.
- [69] D G Cahill and R O Pohl. Lattice Vibrations and Heat Transport in Crystals and Glasses. *Annu. Rev. Phys. Chem.*, 39(1):93–121, 1988.

- [70] David G Cahill and R O Pohl. Heat Flow and Lattice Vibrations in Glasses. *Solid State Commun.*, 70(10):927–930, 1989.
- [71] L. E. Kinsler, A. R. Frey, A. B. Coppens, and J. V. Sanders. *Fundamentals of Acoustics, 4th Edition*. 1999.
- [72] Ivan Stephen Sokolnikoff and Robert Dickerson Specht. *Mathematical Theory of Elasticity*, volume 83. 1956.
- [73] Paul Scherrer. Bestimmung der grösse und der inneren struktur von kolloidteilchen mittels röntgenstrahlen. *Nachr. Ges. Wiss. Göttingen, Math.-Phys. Kl.*, 1918:98–100, 1918.
- [74] Alexander U. Adler. *Defect Analysis of the In-Ga-Zn-O system for Transparent Oxide Semiconductor applications*. PhD thesis, Northwestern University, 2013.
- [75] David G. Cahill and Thomas H. Allen. Thermal Conductivity of Sputtered and Evaporated SiO₂ and TiO₂ Optical Coatings. *Appl. Phys. Lett.*, 65(1994):309–311, 1994.
- [76] Jin Fang, Christian Reitz, Torsten Brezesinski, E. Joseph Nemanick, Chris B. Kang, Sarah H. Tolbert, and Laurent Pilon. Thermal Conductivity of Highly-Ordered Mesoporous Titania Thin Films from 30 to 320 K. *J. Phys. Chem. C*, 115(30):14606–14614, 2011.
- [77] G Gesele, J Linsmeier, V Drach, J Fricke, and R Arens-Fischer. Temperature-Dependent Thermal Conductivity of Porous Silicon. *J. Phys. D: Appl. Phys.*,

- 30(21):2911, 1997.
- [78] Scott Kirkpatrick. Percolation and Conduction. *Rev. Mod. Phys.*, 45(4):574, 1973.
- [79] Ruxandra M Costescu, Andrew J Bullen, George Matamis, Keith E OHara, and David G Cahill. Thermal Conductivity and Sound Velocities of Hydrogen-Silsesquioxane Low- k Dielectrics. *Phys. Rev. B*, 65(9):094205, 2002.
- [80] Charles Kittel. Interpretation of the Thermal Conductivity of Glasses. *Phys. Rev.*, 75(6):972–974, 1949.
- [81] Chunfei Li, Yoshio Bando, Masaki Nakamura, Mitsuko Onoda, and Noboru Kimizuka. Modulated Structures of Homologous Compounds $\text{InMO}_3(\text{ZnO})_m$ ($M = \text{In, Ga}$; $m = \text{Integer}$) Described by Four-Dimensional Superspace Group. *J. Solid State Chem.*, 355(139):347–355, 1998.
- [82] Gang Chen. Thermal Conductivity and Ballistic-Phonon Transport in the Cross-Plane Direction of Superlattices. *Phys. Rev. B*, 57(23):14958, 1998.
- [83] Rama Venkatasubramanian. Lattice Thermal Conductivity Reduction and Phonon Localizationlike Behavior in Superlattice Structures. *Phys. Rev. B*, 61(4):3091, 2000.
- [84] Charles M Brooks, Richard B Wilson, Anna Schäfer, Julia A Mundy, Megan E Holtz, David A Muller, Jürgen Schubert, David G Cahill, and Darrell G Schlom. Tuning Thermal Conductivity in Homoepitaxial SrTiO_3 Films via Defects. *Appl. Phys. Lett.*, 107(5):051902, 2015.

- [85] B Yang, WL Liu, JL Liu, KL Wang, and G Chen. Measurements of Anisotropic Thermoelectric Properties in Superlattices. *Appl. Phys. Lett.*, 81(19):3588–3590, 2002.
- [86] Chuanle Zhou, Boya Cui, I Vurgaftman, CL Canedy, CS Kim, M Kim, WW Bewley, CD Merritt, J Abell, JR Meyer, et al. Thermal Conductivity Tensors of the Cladding and Active Layers of Interband Cascade Lasers. *Appl. Phys. Lett.*, 105(26):261905, 2014.
- [87] FX Alvarez, D Jou, and A Sellitto. Pore-Size Dependence of the Thermal Conductivity of Porous Silicon: A Phonon Hydrodynamic Approach. *Appl. Phys. Lett.*, 97(3):033103, 2010.
- [88] Dietrich Stauffer and Amnon Aharony. *Introduction to Percolation Theory*. CRC press, 1994.
- [89] Von DAG Bruggeman. Berechnung verschiedener physikalischer Konstanten von heterogenen Substanzen. I. Dielektrizitätskonstanten und Leitfähigkeiten der Mischkörper aus isotropen Substanzen. *Ann. Phys.*, 416(7):636–664, 1935.
- [90] JE de Oliveira, JN Page, and HM Rosenberg. Heat Transport by Fracton Hopping in Amorphous Materials. *Phys. Rev. Lett.*, 62(7):780, 1989.
- [91] CL Choy, KW Tong, HK Wong, and WP Leung. Thermal Conductivity of Amorphous Alloys above Room Temperature. *J. Appl. Phys.*, 70(9):4919–4925, 1991.

- [92] VG Karpov and DA Parshin. On the Thermal Conductivity of Glasses at Temperatures below the Debye Temperature. *Zh. Eksp. Teor. Fiz.*, 88(6):2212–2227, 1985.
- [93] S Alexander, Ora Entin-Wohlman, and R Orbach. Phonon-Fractal Anharmonic Interactions: The Thermal Conductivity of Amorphous Materials. *Phys. Rev. B*, 34(4):2726, 1986.
- [94] David G Cahill and Robert O Pohl. Thermal Conductivity of Amorphous Solids above the Plateau. *Phys. Rev. B*, 35(8):4067, 1987.
- [95] BL Zink, R Pietri, and F Hellman. Thermal Conductivity and Specific Heat of Thin-Film Amorphous Silicon. *Phys. Rev. Lett.*, 96(5):055902, 2006.
- [96] A Jagannathan, R Orbach, and O Entin-Wohlman. Thermal Conductivity of Amorphous Materials above the Plateau. *Phys. Rev. B*, 39(18):13465, 1989.
- [97] Joseph L Feldman, Mark D Kluge, Philip B Allen, and Frederick Wooten. Thermal Conductivity and Localization in Glasses: Numerical Study of a Model of Amorphous Silicon. *Phys. Rev. B*, 48(17):12589, 1993.
- [98] Philip B Allen, Joseph L Feldman, Fabian Jaroslav, and Wootend Frederick. Anharmonic Decay of Vibrational States in Amorphous Silicon. *Philos. Mag. B*, 79:1715, 1999.
- [99] Wei Lv and Asegun Henry. Direct Calculation of Modal Contributions to Thermal Conductivity via Green-Kubo Modal Analysis. *New J. Phys.*, 18(1):013028, 2016.

- [100] X Jiang, K Reichelt, and B Stritzker. The Hardness and Young's Modulus of Amorphous Hydrogenated Carbon and Silicon Films Measured with an Ultralow Load Indenter. *J. Appl. Phys.*, 66(12):5805–5808, 1989.
- [101] J Ashley Taylor. The Mechanical Properties and Microstructure of Plasma Enhanced Chemical Vapor Deposited Silicon Nitride Thin Films. *J. Vac. Sci. Technol., A*, 9(4):2464–2468, 1991.
- [102] Charles T. Lynch. *Practical Handbook of Materials Science*. CRC press, 1989.
- [103] DG Neerincx and TJ Vink. Depth Profiling of Thin ITO Films by Grazing Incidence X-ray Diffraction. *Thin Solid Films*, 278(1):12–17, 1996.
- [104] R Martins, P Barquinha, I Ferreira, L Pereira, G Goncalves, and E Fortunato. Role of Order and Disorder on the Electronic Performances of Oxide Semiconductor Thin Film Transistors. *J. Appl. Phys.*, 101(4):044505, 2007.
- [105] Hao Yang and Donald T Morelli. Improved Thermoelectric Properties in Ga_2Te_3 -GaSb Vacancy Compounds. *J. Electron. Mater.*, 41(6):1720–1724, 2012.
- [106] Xingli Zhang and Zhaowei Sun. Influences of Vacancy Defects on Thermal Conductivities of Ge Thin Films. *Rare Metals*, 30(4):317–321, 2011.
- [107] H Tsuchihira, T Oda, and S Tanaka. Modeling of Influence of Lithium Vacancy on Thermal Conductivity in Lithium Aluminate. *Fusion Eng. Des.*, 85(10):1814–1818, 2010.

- [108] NA Katcho, J Carrete, Wu Li, and N Mingo. Effect of Nitrogen and Vacancy Defects on the Thermal Conductivity of Diamond: An Ab Initio Green's Function Approach. *Phys. Rev. B*, 90(9):094117, 2014.
- [109] Jianwei Che, Tahir Cagin, and William A Goddard III. Thermal Conductivity of Carbon Nanotubes. *Nanotechnology*, 11(2):65, 2000.
- [110] Md Delwar Hossain Chowdhury, Mallory Mativenga, Jae Gwang Um, Ravi K Mruthyunjaya, Gregory N Heiler, Timothy John Tredwell, and Jin Jang. Effect of SiO₂ and SiO₂/SiN_x Passivation on the Stability of Amorphous Indium-Gallium Zinc-Oxide Thin-Film Transistors under High Humidity. *IEEE Trans. Electron Devices*, 62(3):869–874, 2015.
- [111] D Bruce Buchholz. unpublished data.
- [112] Sung Woon Cho, Seung Ki Baek, Da Eun Kim, Yunseok Kim, and Hyung Koun Cho. Microstructure-Dependent Thermoelectric Properties of Polycrystalline InGaO₃(ZnO)₂ Superlattice Films. *J. Vac. Sci. Technol., A*, 35(1):01B126, 2017.
- [113] SS Kistler and AG Caldwell. Thermal Conductivity of Silica Aerogel. *Ind. Eng. Chem.*, 26(6):658–662, 1934.
- [114] Prakash C Thapliyal and Kirti Singh. Aerogels as Promising Thermal Insulating Materials: An Overview. *J. Mater.*, 2014, 2014.
- [115] Lawrence W Hrubesh. Aerogel Applications. *J. Non-Cryst. Solids*, 225:335–342, 1998.

- [116] Anubhav Jain, Shyue Ping Ong, Geoffroy Hautier, Wei Chen, William Davidson Richards, Stephen Dacek, Shreyas Cholia, Dan Gunter, David Skinner, Gerbrand Ceder, et al. Commentary: The Materials Project: A Materials Genome Approach to Accelerating Materials Innovation. *APL Mater.*, 1(1):011002, 2013.
- [117] Z Kolter. Linear Algebra Review and Reference., 2008.
- [118] Yang Tang. *Anisotropic Semiconducting Thin Films: Synthesis, In-plane and Cross-plane Characterization, and Thermoelectric Application*. PhD thesis, Northwestern University, 2016.
- [119] Duck-Young Chung, SD Mahanti, Wei Chen, Citrad Uher, and Mercuri G Kanatzidis. Anisotropy in Thermoelectric Properties of CsBi_4Te_6 . In *MRS Proceedings*, volume 793, pages S6–1. Cambridge Univ Press, 2003.
- [120] J-J Gu, M-W Oh, H Inui, and D Zhang. Anisotropy of Mobility Ratio between Electron and Hole along Different Orientations in $\text{Re Ge}_x\text{Si}_{1.75-x}$ Thermoelectric Single Crystals. *Phys. Rev. B*, 71(11):113201, 2005.
- [121] Min-Wook Oh, Jia-Jun Gu, Haruyuki Inui, Myung-Hoon Oh, and Dang-Moon Wee. Evaluation of Anisotropic Thermoelectric Power of $\text{ReSi}_{1.75}$. *Phys. B*, 389(2):367–371, 2007.
- [122] Youhei Sakamaki, Kosuke Kuwabara, Gu Jiajun, Haruyuki Inui, Masaharu Yamaguchi, Atsushi Yamamoto, and Haruhiko Obara. Crystal Structure and Thermoelectric Properties of $\text{ReSi}_{1.75}$ Based Silicides. In *Materials Science Forum*, volume

- 426, pages 1777–1782. Trans Tech Publ, 2003.
- [123] JJ Gu, K Kuwabara, K Tanaka, H Inui, M Yamaguchi, A Yamamoto, T Ohta, and H Obara. Crystal Structure and Thermoelectric Properties of $\text{ReSi}_{1.75}$ Silicide. In *MRS Proceedings*, volume 753, pages BB6–10. Cambridge Univ Press, 2002.
- [124] Khuong P Ong, David J Singh, and Ping Wu. Unusual Transport and Strongly Anisotropic Thermopower in PtCoO_2 and PdCoO_2 . *Phys. Rev. Lett.*, 104(17):176601, 2010.
- [125] H Takatsu, H Yoshizawa, and Y Maeno. Comparative Study of Conductive Delafossites with and without Frustrated Spins on a Triangular Lattice, PdMO_2 (M=Cr; Co). In *Journal of Physics: Conference Series*, volume 145, page 012046. IOP Publishing, 2009.
- [126] Ramzy Daou, Raymond Frésard, Sylvie Hébert, and Antoine Maignan. Large Anisotropic Thermal Conductivity of the Intrinsically Two-Dimensional Metallic Oxide PdCoO_2 . *Phys. Rev. B*, 91(4):041113, 2015.
- [127] N Hamada, T Imai, and H Funashima. Thermoelectric Power Calculation by the Boltzmann Equation: Na_xCoO_2 . *J. Phys.: Condens. Matter*, 19(36):365221, 2007.
- [128] Ichiro Terasaki, Yoshitaka Sasago, and Kunimitsu Uchinokura. Large Thermoelectric Power in NaCo_2O_4 Single Crystals. *Phys. Rev. B*, 56(20):R12685, 1997.
- [129] DO Demchenko and David B Ameen. Lattice Thermal Conductivity in Bulk and Nanosheet Na_xCoO_2 . *Comput. Mater. Sci.*, 82:219–225, 2014.

- [130] JL Cohn, BD White, CAM Dos Santos, and JJ Neumeier. Giant Nernst Effect and Bipolarity in the Quasi-One-Dimensional Metal $\text{Li}_{0.9}\text{Mo}_6\text{O}_{17}$. *Phys. Rev. Lett.*, 108(5):056604, 2012.
- [131] Nicholas Wakeham, Alimamy F Bangura, Xiaofeng Xu, Jean-Francois Mercure, Martha Greenblatt, and Nigel E Hussey. Gross Violation of the Wiedemann-Franz Law in a Quasi-One-Dimensional Conductor. *Nat. Commun.*, 2:396, 2011.
- [132] An Ning Qiu, Lan Ting Zhang, and Jian Sheng Wu. Structure Stability and Electronic Structure of Semiconducting Rhenium Silicide with Doping. In *Adv. Mater. Res.*, volume 26, pages 1029–1032. Trans Tech Publ, 2007.
- [133] Peter E Blöchl. Projector Augmented-Wave Method. *Phys. Rev. B*, 50(24):17953, 1994.
- [134] Jianwei Sun, Richard C Remsing, Yubo Zhang, Zhaoru Sun, Adrienn Ruzsinszky, Haowei Peng, Zenghui Yang, Arpita Paul, Umesh Waghmare, Xifan Wu, et al. Accurate First-Principles Structures and Energies of Diversely Bonded Systems from an Efficient Density Functional. *Nat. Chem.*, 2016.
- [135] Georg KH Madsen and David J Singh. BoltzTraP. A Code for Calculating Band-Structure Dependent Quantities. *Comput. Phys. Commun.*, 175(1):67–71, 2006.
- [136] Jiong Yang, Huanming Li, Ting Wu, Wenqing Zhang, Lidong Chen, and Jihui Yang. Evaluation of Half-Heusler Compounds as Thermoelectric Materials Based on the Calculated Electrical Transport Properties. *Adv. Funct. Mater.*, 18(19):2880–2888, 2008.

2008.

- [137] Anton Kokalj. XCrySDenA New Program for Displaying Crystalline Structures and Electron Densities. *J. Mol. Graphics Modell.*, 17(3):176–179, 1999.
- [138] Chuanle Zhou, G Koblmuller, M Bichler, G Abstreiter, and M Grayson. Thermal Conductivity Tensor of Semiconductor Layers Using Two-Wire 3ω Method. In *Proc. of SPIE*, volume 8631, page 863129, 2013.
- [139] Chuanle Zhou. *Transverse $p \times n$ -type Type Thermoelectrics: Type II Superlattices and their Thermal Conductivity Characterization*. PhD thesis, Northwestern University, 2013.
- [140] T Borca-Tasciuc, AR Kumar, and G Chen. Data Reduction in 3ω Method for Thin-Film Thermal Conductivity Determination. *Rev. Sci. Instrum.*, 72(4):2139–2147, 2001.
- [141] MC Gold and DA Nelson. Variable Magnetic Field Hall Effect Measurements and Analyses of High Purity, Hg Vacancy (p -type) HgCdTe. *J. Vac. Sci. Technol., A*, 4(4):2040–2046, 1986.
- [142] WA Beck and JR Anderson. Determination of Electrical Transport Properties Using a Novel Magnetic Field-Dependent Hall Technique. *J. Appl. Phys.*, 62(2):541–554, 1987.

- [143] JR Meyer, CA Hoffman, FJ Bartoli, DA Arnold, S Sivananthan, and JP Fauri. Methods for Magnetotransport Characterization of IR Detector Materials. *Semicond. Sci. Technol.*, 8(6S):805, 1993.
- [144] J Antoszewski, DJ Seymour, L Faraone, JR Meyer, and CA Hoffman. Magneto-Transport Characterization Using Quantitative Mobility-Spectrum Analysis. *J. Electron. Mater.*, 24(9):1255–1262, 1995.
- [145] JR Meyer, CA Hoffman, FJ Bartoli, J Antoszewski, L Faraone, SP Tobin, PW Norton, CK Ard, DJ Reese, L Colombo, et al. Advanced Magneto-Transport Characterization of LPE-Grown $\text{Hg}_{1-x}\text{Cd}_x\text{Te}$ by Quantitative Mobility Spectrum Analysis. *J. Electron. Mater.*, 25(8):1157–1164, 1996.
- [146] I Vurgaftman, JR Meyer, CA Hoffman, D Redfern, J Antoszewski, L Faraone, and JR Lindemuth. Improved Quantitative Mobility Spectrum Analysis for Hall Characterization. *J. Appl. Phys.*, 84(9):4966–4973, 1998.
- [147] S Kiatgamolchai, M Myronov, OA Mironov, VG Kantser, EHC Parker, and TE Whall. Mobility Spectrum Computational Analysis Using a Maximum Entropy Approach. *Phys. Rev. E*, 66(3):036705, 2002.
- [148] J Antoszewski, GA Umana-Membreno, and L Faraone. High-Resolution Mobility Spectrum Analysis of Multicarrier Transport in Advanced Infrared Materials. *J. Electron. Mater.*, 41(10):2816–2823, 2012.

- [149] Jeffrey Lindemuth, Brad Dodrill, Jerry Meyer, and Igor Vurgaftman. Extraction of Low Mobility, Low Conductivity Carriers from Field Dependent Hall Data. 2002.
- [150] Norman O Birge, Paul K Dixon, and Narayanan Menon. Specific Heat Spectroscopy: Origins, Status and Applications of the 3ω Method. *Thermochim. Acta*, 304:51–66, 1997.
- [151] David Andrew de Koninck. Thermal Conductivity Measurement Using the 3-omega Technique: Applications to Power Harvesting Microsystems. 2008.

APPENDIX

1. Wheatstone Configuration for 3ω Measurement

The circuit connection of a conventional 4-point measurement and a 2-point Wheatstone bridge measurement[150, 151] are illustrated in Figure .1. In a 4-point measurement (Figure .1 left), one lock-in amplifier measures the 3ω voltage across the sample filament, while the other measures the 3ω voltage across a reference resistor R_{ref} (usually a potentiometer) in equal resistance. The 3ω voltage across R_{ref} indicates the background 3ω components from the lock-in power source V_{source} and input channels, as well as other

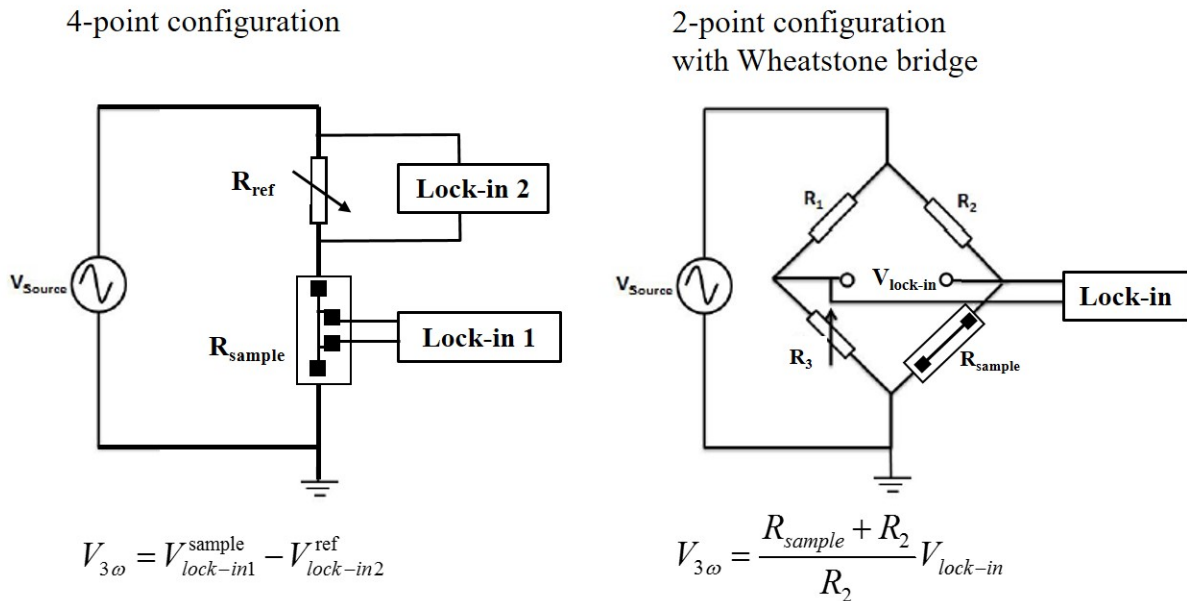


Figure .1. Circuit connection of 4-point (left) and 2-point (left) measurement.

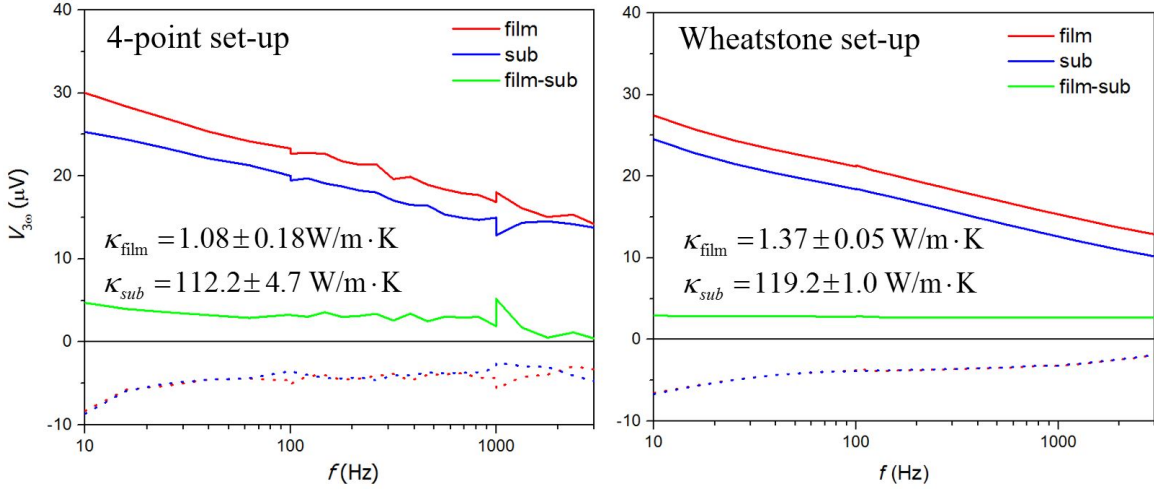


Figure .2. Comparison of 3ω raw datasets from a 150-nm thick SiN_x thin film on a silica substrate.

nonlinear signal in the circuit. So the final $V_{3\omega}$ is the 3ω voltage difference between sample filament and R_{ref} . In a Wheatstone bridge setup (Figure .1 right), only one lock-in is required to measure the 3ω voltage across the bridge when the bridge is balanced. The resistors R_1 and R_2 have fixed resistances, while R_3 is a potentiometer to zero the 1ω voltage across the bridge. These resistors have negligible temperature coefficient compared with the sample filament, which makes sure that no other harmonics are induced away from R_{sample} . The resistance on the left arm of the bridge R_1 and R_3 are chosen to be much larger than those on the right arm (R_2 and R_{sample}) to maximize the power to the sample heater filament.

A calibration measurement was performed on a 150-nm thick SiN_x thin film grown by PECVD on a silica substrate. Both 4-point and 2-point filaments are patterned on the film and the bare substrate to facilitate the two configurations for comparison (Figure .2), where κ_{film} and κ_{sub} are consistent in two cases. Compared with the conventional 4-point result on the left of Figure .2, the Wheatstone configuration on the right obviously

gives much less noise and a cleaner 3ω signal (in the circuit $R_1 = 2 \text{ k}\Omega$, $R_2 = 100 \text{ }\Omega$, $R_{sample} \sim 50 \text{ }\Omega$). Because the 2-point measurement is based on a balanced Wheatstone bridge with $V_{1\omega}$ measured in the lock-in almost zero ($V_{1\omega} < 20 \text{ }\mu\text{V}$), while in the 4-point measurement the lock-in $V_{1\omega}$ channel measures signal 4 orders of magnitude higher ($V_{1\omega} = 400\text{-}900 \text{ mV}$). Error bar of κ_{film} is based on the standard deviation of $V_{3\omega}$ across the whole frequency range, and error bar of κ_{sub} is obtained from slope variations in different sweeps performed. Given the improved noise level in Wheatstone setup, the error bar in both κ_{film} and κ_{sub} are much smaller.